

Faculty of Physics and Astronomy

University of Heidelberg

Diploma Thesis
in Physics

submitted by
Christoph Anders
born in Dresden/Germany

June 2007

Measurement of the Branching Fraction $B^+ \rightarrow \eta \ell^+ \nu$ with the BABAR-Experiment

*This diploma thesis has been performed by Christoph Anders at the
Institute for Physics
under the supervision of
Prof. Dr. Ulrich Uwer*

Kurzfassung

Im *BABAR*-Experiment werden B -Mesonenpaare in e^+e^- -Kollisionen bei einer Schwerpunktsenergie von 10,58 GeV, welche der Masse der $\Upsilon(4S)$ -Resonanz entspricht, produziert. Aufgrund des großen Datensatzes, der einer totalen integrierten Luminosität von 347 fb^{-1} oder 382 Millionen $B\bar{B}$ -Paaren entspricht, ist es möglich, seltene B -Zerfälle mit kleinen Verzweigungsverhältnissen zu untersuchen. Diese Analyse beschreibt die Messung des Verzweigungsverhältnisses des charmfreien semileptonischen B -Zerfalls $B^+ \rightarrow \eta\ell^+\nu_\ell$, wobei das η -Meson im Kanal $\eta \rightarrow \pi^+\pi^-\pi^0$ rekonstruiert wird. Während andere Analysen das zweite B -Meson vollständig rekonstruieren um die Ereigniskinematik zur Untergrundunterdrückung zu nutzen, wird in dieser Analyse nur das semileptonisch zerfallende B -Meson rekonstruiert, was den Vorteil einer höheren Signaleffizienz mit sich bringt. Um das Signal von den Hauptuntergründen zu trennen, werden neuronale Netze benutzt. Das Verzweigungsverhältnis wird mit Hilfe eines Maximum-Likelihood Verfahrens bestimmt. Es wird ein Signal von 285 ± 8 Ereignissen über 4.682 ± 48 Untergrundereignissen bestimmt. Dieses Signal entspricht einem Verzweigungsverhältnis von $\mathcal{B}(B^+ \rightarrow \eta\ell^+\nu_\ell) = (6,47 \pm 1,48_{\text{stat.}} \pm 1,44_{\text{syst.}}) \cdot 10^{-5}$. Die angegebenen Unsicherheiten sind statistischer und systematischer Natur. Die vorgestellte Analyse ist die erste *BABAR*-Messung des Zerfallskanals, die auf die Rekonstruktion des zweiten B -Mesons verzichtet.

Abstract

In the *BABAR*-experiment pairs of B -mesons are produced in e^+e^- -collisions at a center-of-mass energy of 10.58 GeV corresponding to the mass of the $\Upsilon(4S)$ -resonance. The high total integrated luminosity of 347 fb^{-1} acquired, equivalent to about 382 million $B\bar{B}$ -pairs, allows to study rare B -decays with small branching fractions. This analysis presents a branching fraction measurement of the charmless semileptonic B -decay $B^+ \rightarrow \eta\ell^+\nu_\ell$. The η -meson is reconstructed in the channel $\eta \rightarrow \pi^+\pi^-\pi^0$. Earlier analyses have fully reconstructed the second B -meson in the event in order to use the event kinematics for background suppression. This analysis reconstructs only the B -meson decaying semileptonically. This leads to a higher signal efficiency. Neural-networks are used to distinguish the signal from the main backgrounds. The branching fraction is extracted by using a maximum likelihood method. The analysis yields 285 ± 8 signal events over $4,682 \pm 48$ background events. The signal events correspond to a branching fraction of $\mathcal{B}(B^+ \rightarrow \eta\ell^+\nu_\ell) = (6.47 \pm 1.48_{\text{stat.}} \pm 1.44_{\text{syst.}}) \cdot 10^{-5}$. The uncertainties are of statistic and systematic nature. The described analysis is the first *BABAR*-measurement of the decay channel that does not reconstruct the second B -meson in the event.

Contents

1	Introduction	7
2	Theory	9
2.1	Standard Model of Particle Physics	9
2.2	The Cabibbo-Kobayashi-Maskawa Matrix	10
2.3	Charmless Semileptonic B-Decays	10
2.4	Form Factors for $B^+ \rightarrow \eta \ell^+ \nu_\ell$	12
2.4.1	Form Factor Models	12
3	The <i>BABAR</i>-Experiment	13
3.1	The PEP-II e^+e^- -Collider	13
3.2	The <i>BABAR</i> -Detector	14
3.2.1	Silicon Vertex Tracker	14
3.2.2	Drift Chamber	17
3.2.3	Detector of Internally Reflected Čerenkov Light	18
3.2.4	Electromagnetic Calorimeter	19
3.2.5	The Instrumented Flux Return	19
3.2.6	Particle Identification with the <i>BABAR</i> Detector	20
4	Data and Monte-Carlo Samples	23
4.1	Data Samples	23
4.2	Monte-Carlo Samples	23
4.2.1	Classification of Monte-Carlo Events	24
4.3	Data Monte-Carlo Comparison	29
4.3.1	Continuum Monte-Carlo and Off-Resonance Data	31
4.3.2	Monte-Carlo and On-Resonance Data	32
5	Event Selection	35
5.1	Preselection	35
5.1.1	Computational Steps	35
5.1.2	Preselection Criteria	36
5.1.3	Y-System	37
5.1.4	Neutrino Reconstruction	39
5.1.5	Event Shape Variables	43

5.1.6	m_{ES} and ΔE	44
5.2	Analysis Selection	45
5.3	Multivariate Analysis	48
5.3.1	Neural-Networks	48
5.3.2	Neural-Network Configurations	50
5.3.3	Neural-Network Training and Testing	55
5.3.4	Neural-Network Optimization	55
6	Extraction of the Branching Fraction	65
6.1	The Barlow-Beeston Fit Algorithm	65
6.2	Fit Strategy	67
6.3	Fit Validation	70
6.4	Fit Result	70
7	Systematic Uncertainties	75
7.1	Detector Effects	75
7.1.1	Track and Photon Reconstruction	75
7.1.2	K_L^0 Production and Interactions	77
7.1.3	Lepton Identification Efficiency	77
7.1.4	Neutral Pion Efficiency	77
7.2	Physics Modeling	77
7.2.1	$q\bar{q}$ -Continuum Normalization	78
7.2.2	$b \rightarrow c\ell\nu$ Normalization	78
7.2.3	$B \rightarrow u\ell\nu$ Branching Fraction	79
7.2.4	$\eta \rightarrow \pi^+\pi^-\pi^0$ Branching Fraction	79
7.3	Neural-Networks	79
7.3.1	Neural-Network Configuration	79
7.3.2	Neural-Network Training	80
7.4	$B\bar{B}$ Counting	81
7.5	Summary of Systematic Uncertainties	81
8	Conclusion and Outlook	83
	Appendices	88
A	Kaon Veto Study	89
B	Neural-Network Input Distributions	91

Chapter 1

Introduction

The *BABAR*-experiment was designed to study the properties of B -mesons. The initial goal was to discover CP-violation in the B -meson system, which was already achieved in 2001. Due to the very high number of B -meson pairs recorded (about 496 million until June 2007), processes with small cross sections become accessible, allowing tests of the standard model. Of particular interest are precision and over-constraining measurements of the parameters of the Cabibbo-Kobayashi-Maskawa (CKM) quark mixing matrix [1], which is the only source of CP-violation in the standard model.

The branching fractions of semileptonic B -meson decays into light mesons (“charmless semileptonic B -decays”), $B \rightarrow X_u \ell \nu$ where $X_u = \pi^{\pm,0}, \rho^{\pm,0}, \omega, \eta, \eta'$ are directly proportional to the CKM matrix element $|V_{ub}|^2$ because on quark level a “b to u” transition takes place. Different analysis methods can be used to measure these branching fractions. In the “inclusive methods” only the lepton is reconstructed and no difference is made between the light hadrons. Therefore, the total inclusive branching fraction $\mathcal{B}(B \rightarrow X_u \ell \nu)$ is determined. In the “exclusive methods” the light hadron final state is explicitly reconstructed, and the specific branching fraction is measured, e.g. $\mathcal{B}(B \rightarrow \eta \ell \nu)$. As the B -mesons are produced in pairs, both methods can either be applied with the additional reconstruction of the other B -meson (“tagged”) or without reconstructing it (“untagged”). In untagged analyses the signal event yield is larger, and hence the statistic uncertainties are lower, while tagged analyses have cleaner data samples and therefore usually smaller systematic uncertainties. Independent of the method used, the main problem for the analyses of charmless semileptonic B -decays is the huge background of semileptonic B -decays into systems containing charm quarks (“charmed semileptonic B -decays”). The ratio can roughly be estimated by $\Gamma(b \rightarrow u \ell \nu)/\Gamma(b \rightarrow c \ell \nu) \approx 2(|V_{ub}|/|V_{cb}|)^2 \approx 0.02$, where the factor of two arises due to phase-space considerations [2].

The *BABAR*-experiment has already published results on analyses of the decays $B^0 \rightarrow \pi^- \ell^+ \nu_\ell$ ¹ and $B^0 \rightarrow \rho^- \ell^+ \nu_\ell$ [3].

¹Here and in the following the charge conjugated decays are included.

In this thesis an exclusive untagged branching fraction measurement of the charmless B -decay $B^+ \rightarrow \eta \ell^+ \nu_\ell$ is presented². This branching fraction has been measured by the CLEO-collaboration using 9.7 million B -pairs yielding about 15 signal decays [5]. An exclusive tagged analysis conducted by *BABAR* using about 350 million B -pairs yielded 45.9 ± 7.1 signal events³ [6].

The exclusive untagged analysis presented here uses about 380 million B -pairs. It is expected to achieve a higher signal efficiency and therefore a larger signal yield than the earlier tagged *BABAR*-analysis.

²The η is reconstructed in the $\eta \rightarrow \pi^+ \pi^- \pi^0$ decay channel, that accounts for a branching fraction of $\mathcal{B}(\eta \rightarrow \pi^+ \pi^- \pi^0) = (22.7 \pm 0.4)\%$ [4].

³This analysis reconstructs the η in three channels: $\eta \rightarrow \gamma\gamma$ (39%), $\eta \rightarrow \pi^0 \pi^0 \pi^0$ (33%) and $\eta \rightarrow \pi^+ \pi^- \pi^0$ (23%) [4].

Chapter 2

Theory

2.1 Standard Model of Particle Physics

The standard model of particle physics is a theory that very successfully describes three of the four known fundamental interactions between elementary particles, namely the electromagnetic, the weak and the strong interaction, while the fourth - gravity - is not included. It is a relativistic quantum field theory, consistent with both quantum mechanics and special relativity, that describes two types of elementary particles the spin- $\frac{1}{2}$ fermions and the spin-1 bosons that mediate the interactions. To each fermion exists a corresponding anti-fermion that - in case the fermion is charged - is of opposite charge. The fermions are divided into quarks and leptons that both can be grouped in three doublets¹ and that are usually sorted into three so-called generations (Tab. 2.1). A quark doublet consist of one quark with a charge of $q = 2/3 \cdot e$ and another one with a charge of $q = -1/3 \cdot e$ (or $q = -2/3 \cdot e$ and $q = -1/3 \cdot e$ for anti-quarks respectively). The lepton doublet consist of a charged lepton (negative for leptons and positive for anti-leptons) and a neutral lepton called neutrino.

The bosons are the photon, two oppositely charged W-bosons, the Z-boson and the gluon. The massless photon mediates the electromagnetic interaction thus coupling to all charged particles, while the gluon - massless as well - couples

¹Actually 2×3 if one counts the antifermions, too.

	Electric Charge	1 st Generation		2 nd Generation		3 rd Generation	
		Name	Symbol	Name	Symbol	Name	Symbol
Quarks	2/3e	up	u	charm	c	top	t
	-1/3e	down	d	strange	s	bottom	b
Leptons	0	Neutrino	ν_e	Neutrino	ν_μ	Neutrino	ν_τ
	-1e	Electron	e	Muon	μ	Tau	τ

Table 2.1: *The fermions of the standard model*

to the so-called three color charges that only quarks, anti-quarks and the gluons themselves carry and is the mediator of the strong force. The massive W- and Z-bosons mediate the weak force.

Up to now all these particles have been observed, the latest being the top-quark discovered in 1995, and the standard model predictions agree with all experimental tests conducted so far. However, there is one more predicted particle, the spinless Higgs boson, that has not been discovered yet. The Higgs boson plays a key role in understanding the origin of the particle masses.

2.2 The Cabibbo-Kobayashi-Maskawa Matrix

In the standard model the mass-eigenstates of the quarks are not equivalent to their eigenstates with respect to the weak interaction. The weak eigenstates can be described as a linear combination of the mass eigenstates. The transformation is described by the so-called Cabibbo-Kobayashi-Maskawa (CKM) matrix [1]:

$$\underbrace{\begin{pmatrix} d' \\ s' \\ b' \end{pmatrix}}_{\text{WeakEigenstates}} = \underbrace{\begin{pmatrix} V_{ud} & V_{us} & V_{ub} \\ V_{cd} & V_{cs} & V_{cb} \\ V_{td} & V_{ts} & V_{tb} \end{pmatrix}}_{\text{CKM-Matrix } V_{\text{CKM}}} \cdot \underbrace{\begin{pmatrix} d \\ s \\ b \end{pmatrix}}_{\text{MassEigenstates}}$$

The complex matrix is unitary by definition, i.e.

$$\begin{aligned} VV^\dagger &= V^\dagger V = 1 \\ \Rightarrow \sum_{i=1}^3 V_{ij}V_{ik}^* &= \delta_{jk} \quad \forall j, k \end{aligned}$$

Where the relation $V_{ud}V_{ub}^* + V_{cd}V_{cb}^* + V_{td}V_{tb}^* = 0$ is used to define the so-called unitarity triangle in the complex plane. It is shown in Fig. 2.1.

2.3 Charmless Semileptonic B-Decays

The signal decay in this analysis is $B^+ \rightarrow \eta \ell^+ \nu_\ell$. The B^+ -Meson consists of a u and a \bar{b} quark. It has a mass of $m_{B^+} = (5279.0 \pm 0.5) \text{ MeV}/c^2$ and a mean life time of $\tau_{B^+} = (1.638 \pm 0.011) \cdot 10^{-12} \text{ s}$. The quark model prediction for its isospin I , angular momentum J and parity P is $I(J^P) = 1/2(0^-)$ [4].

The η -meson is a $u\bar{u} + d\bar{d}$ combination with a mass of $m_\eta = (547.51 \pm 0.18) \text{ MeV}/c^2$ and a full decay width of $\Gamma = (1.30 \pm 0.07) \text{ keV}$. It is a pseudo-scalar meson, i.e. $I(J^P) = 0(0^-)$ [4].

In this analysis the reconstructed lepton ℓ is either an electron or a muon. Their masses are measured with very high precision:

$$\begin{aligned} m_e &= (0.51099892 \pm 0.00000004) \text{ MeV}/c^2 \\ m_\mu &= (105.658369 \pm 0.000009) \text{ MeV}/c^2 \end{aligned}$$

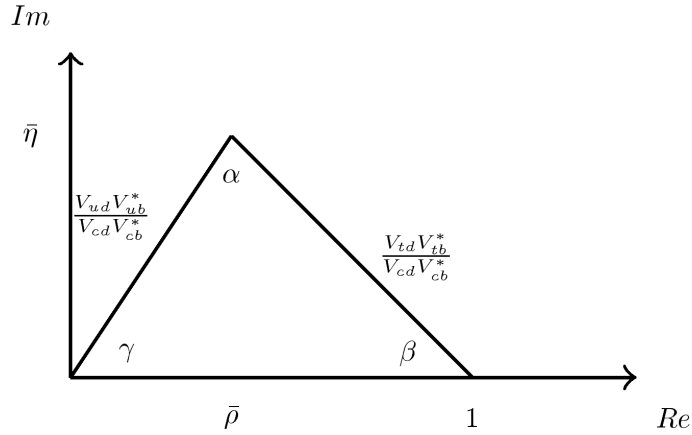


Figure 2.1: The unitarity triangle in the complex plane, with the bottom side scaled to one.

While the electron is a stable particle the muon decays to almost 100% through the channel $\mu^- \rightarrow e^- \bar{\nu}_e \nu_\mu$ and has a lifetime of $\tau_\mu = (2.19703 \pm 0.00004) \cdot 10^{-6}$ s [4].

The Feynman graph for the signal decay $B^+ \rightarrow \eta \ell^+ \nu_\ell$ studied in this thesis is shown in Fig. 2.2. It illustrates the transition of the B -meson's b quark into a u quark with the simultaneous emission of a W -boson. On quark level the probability of this $b \rightarrow u$ transition is $\propto |V_{ub}|^2$.

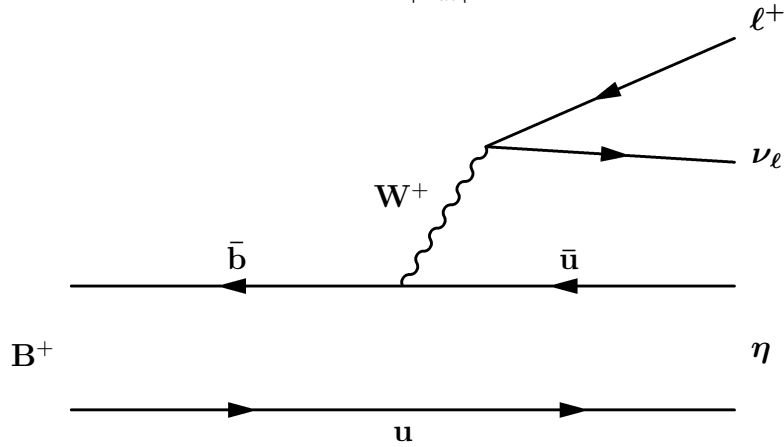


Figure 2.2: Feynman diagram for the signal decay $B^+ \rightarrow \eta \ell \nu$

However, as the quarks are bound into mesons the process is actually more complicated. The transition matrix element for the $B_{bu}^+ \rightarrow \eta_{\bar{u}u} \ell^+ \nu_\ell$ decay is:

$$M(B_{bu}^+ \rightarrow \eta_{\bar{u}u} \ell^+ \nu_\ell) \propto V_{ub}^* L^\mu H_\mu [2]$$

Where $L^\mu = \langle \Psi_\ell | \gamma^\mu (1 - \gamma^5) | \Psi_\nu \rangle$ is the leptonic current, with Ψ_ℓ and Ψ_ν being the

Dirac spinors of the electron and neutrino². $H_\mu = \langle \eta_{\bar{u}u} | \bar{u} \gamma^\mu (1 - \gamma_5) b | B_{\bar{b}u} \rangle$ is the hadronic current which is not easily calculable because of the complexity of the low-energy QCD processes inside the mesons. It is customary to introduce form factors to describe the overlap of the initial B -meson with the final state meson (in this case the η). The form factors are a function of q^2 , the virtual W mass,

$$q^2 = m_W^2 = (p_\ell + p_{\bar{\nu}})^2 = (p_B - p_\eta)^2$$

where p_B and p_η are the four-momentum of the B -meson and the η -meson.

2.4 Form Factors for $B^+ \rightarrow \eta \ell^+ \nu_\ell$

For the signal decay, $B^+ \rightarrow \eta \ell^+ \nu_\ell$ the branching ratio is

$$\mathcal{B}(B^+ \rightarrow \eta \ell^+ \nu_\ell) \propto |V_{ub}|^2 |f^+(q^2)|^2 [2]$$

for electrons and muons³. Evidently for the extraction of $|V_{ub}|$ the theoretical shape of the form factor is needed.

2.4.1 Form Factor Models

Form factors are difficult to calculate, as they cannot be derived from first principles and require theoretical descriptions of “non-perturbative effects”. There are several theoretical groups trying to calculate the form factor shape under different model assumptions:

- **ISGW2** [7]: Older ansatz that is still implemented in many Monte-Carlo generators. It uses a constituent quark model with relativistic corrections. It seems not to be consistent with actual data from the $B^0 \rightarrow \pi^- \ell^+ \nu_\ell$ channel [2].
- **Ball** [8]: Uses QCD sum rules evaluated on the light cone.
- **Lattice QCD** [9, 10]: Uses quenched lattice QCD simulations. Up to now, only calculations for $B^0 \rightarrow \pi^- \ell^+ \nu_\ell$ exist. The calculations are only reliable for large q^2 , i.e. $q^2 < \frac{1}{2} q_{\text{max}}^2$.

As no lattice calculation for $B^+ \rightarrow \eta \ell^+ \nu_\ell$ exists and the ISGW2 model is considered obsolete, the QCD sum rules form factor calculation is used in this analysis.

Ultimately, the problem could be solved by extracting the form factor shape in dependence of q^2 from the data. A theoretical prediction would hence only be needed at a single (well calculable) point in the q^2 spectrum to fix the overall normalization. Thus $|V_{ub}|$ could be extracted with small theoretical uncertainties. However, the signal event yield in this analysis is too small to measure the form factor shape in dependence of q^2 .

²With γ^μ , γ^5 being the Dirac gamma matrices.

³There is a second form factor $f^0(q^2)$, which can be neglected for small lepton masses.

Chapter 3

The *BABAR*-Experiment

The *BABAR*-experiment [11] is performed at the Stanford Linear Accelerator Center (SLAC)¹. It consists of PEP-II², an asymmetric e^+e^- -collider and the *BABAR*-detector.

3.1 The PEP-II e^+e^- -Collider

The PEP-II-collider consists of two storage-rings (Fig. 3.1). The “high energy ring (HER)” accelerates electrons to an energy of 9 GeV. The “low energy ring (LER)” accelerates positrons to an energy of 3.1 GeV. The beam particles collide inside the *BABAR*-detector with a center-of-mass energy of 10.58 GeV, which corresponds to the invariant mass of the $\Upsilon(4S)$ -resonance. The resonance decays dominantly (branching fraction $\approx 96\%$) into a pair of $B\bar{B}$ -mesons. The combined mass of the two B-mesons produced is about 20 MeV below the resonance’s mass and therefore the B-mesons have very small momenta in the resonance’s rest frame. However, as asymmetric beam energies are used, the system is boosted in the laboratory frame by a boost factor of $\beta\gamma = 0.56$. The B -mesons have momenta high enough to perform time resolved studies. Because of the large number of boosted $B\bar{B}$ -pairs *BABAR* and PEP-II are often called *B* Factory.

The design luminosity of the PEP-II collider is $3 \cdot 10^{33} \text{ cm}^{-2}\text{s}^{-1}$. The actual performance turned out to be even higher and the current luminosity record (achieved in August 2006) is $12 \cdot 10^{33} \text{ cm}^{-2}\text{s}^{-1}$. To achieve this luminosity 1722 bunches (design: 1658) are circling in the collider, corresponding to currents of 2900 mA in the LER (design: 2150 mA) and 1875 mA in the HER (750 mA)

To this point (June 2007) PEP-II has delivered an integrated luminosity of about 450 fb^{-1} of which *BABAR* has recorded about 430 fb^{-1} . The integrated luminosity from the start of *BABAR* in 1999 until now is shown in Fig. 3.2. In this thesis data corresponding to an integrated luminosity of 347 fb^{-1} are used.

¹SLAC is located on Stanford University property at Menlo Park, California.

²PEP stands for **P**ositron **E**lectron **P**roject.

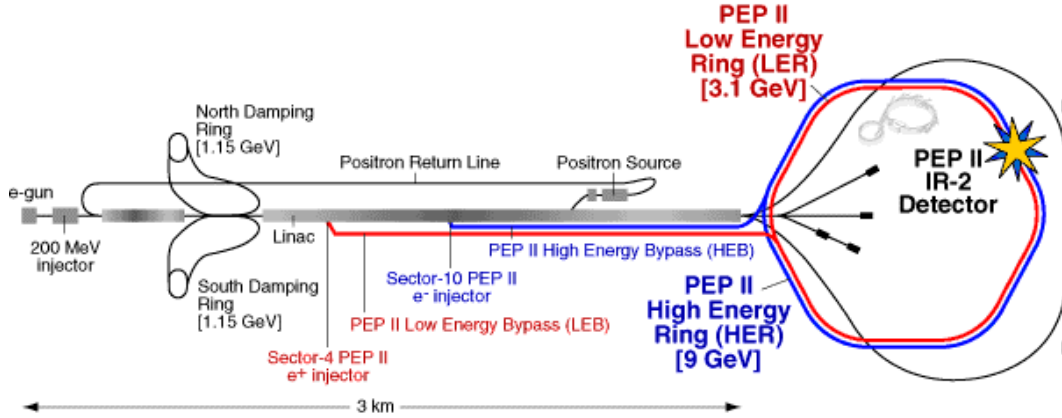


Figure 3.1: Schematics of the linear accelerators used to pre-accelerate the electrons and positrons and the PEP-II collider rings. The BABAR detector is located at the upper right side where the star illustrates a collision.

3.2 The BABAR-Detector

Fig. 3.3 shows a longitudinal section of the BABAR-detector. Its several sub-detectors are symmetrically arranged around the beam pipe, which has a diameter of 2.78 cm. It is asymmetric in beam direction as the boost defines a preferred flight direction for the particles produced. The innermost sub-detector located directly around the interaction point, where the beams are colliding, is a silicon vertex tracker which together with a drift chamber enclosing it performs the track reconstruction and momentum measurement. The drift chamber is surrounded by a Čerenkov detector, called “detector of internally reflected Čerenkov light”. It is mainly used for particle identification. An electromagnetic calorimeter consisting of two parts, the so-called barrel located around the Čerenkov detector and an end-cap in flight direction of the electrons (i.e. the boost), accounts for the asymmetric collision energy. All sub-detectors are surrounded by a solenoidal super conducting coil providing a magnetic field of 1.5 T parallel to the beam axis. The outermost subsystem is the instrumented flux return which is used to detect muons and neutral hadrons, e.g. K_L^0 .

3.2.1 Silicon Vertex Tracker

The silicon vertex tracker consists of five concentric, cylindrically arranged layers of double sided silicon strip detectors (Fig. 3.4). The innermost layer is located as close as possible to the beam pipe and the silicon vertex tracker covers the polar angle³ region from 20° to 150° . The main purpose of the silicon vertex tracker is

³The Polar angle is the angle to the beam axis, defined to be zero in direction of the electron beam

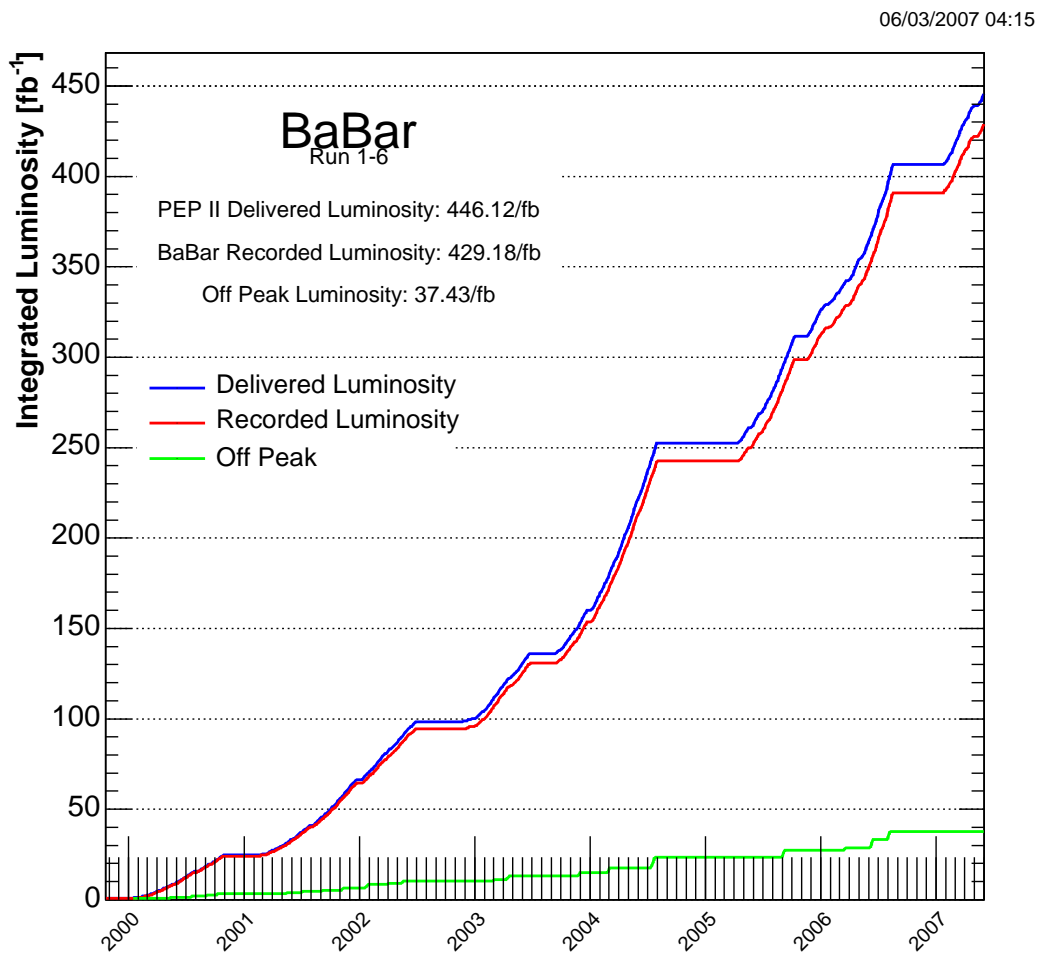


Figure 3.2: *The integrated luminosity delivered by PEP-II (blue line) and recorded by BABAR (red line) in dependence of the operation time. The green line shows the Integrated Luminosity of so-called off-peak or off-resonance data taken at a center-of-mass energy 40 MeV below the $\Upsilon(4S)$ resonance [12].*

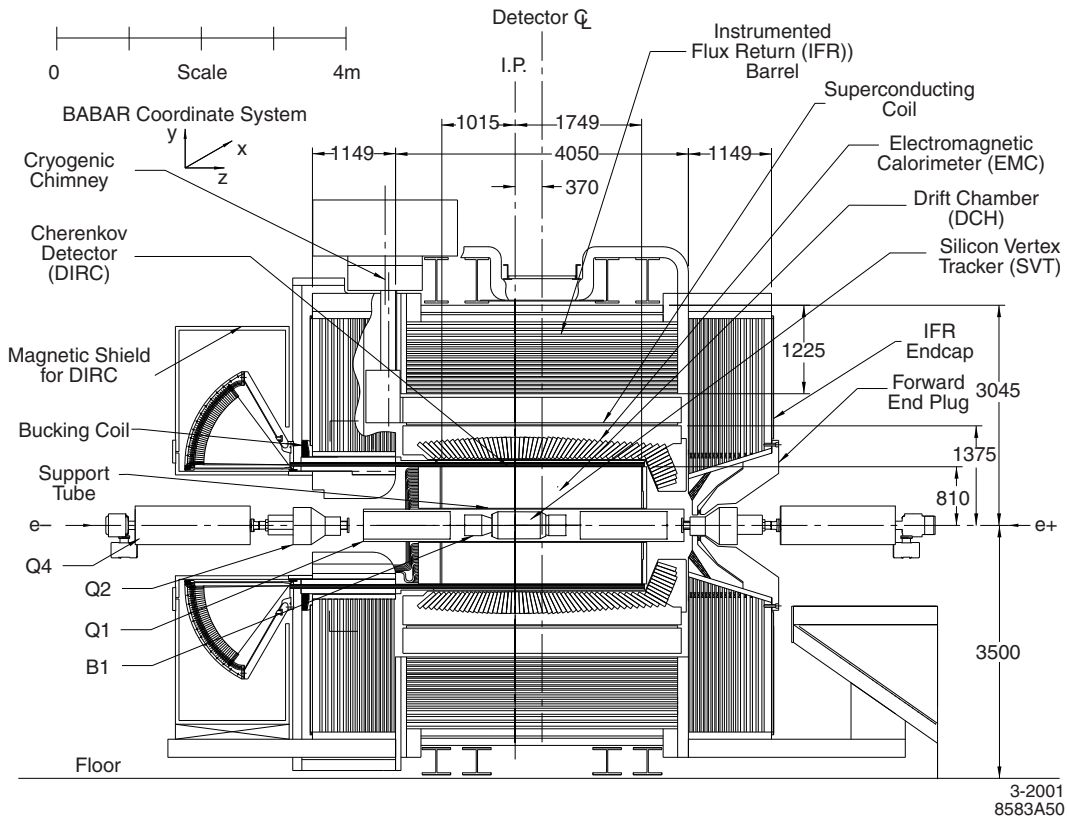


Figure 3.3: Longitudinal section of the BABAR-detector. On the upper left the BABAR coordinate system is shown. The electron beam enters from the left – in z -direction – while the positron beam enters from the right. Sub-detectors from innermost to outermost: silicon vertex tracker, drift chamber, Čerenkov detector, electromagnetic calorimeter all surrounded by the solenoidal super conducting coil and finally the instrumented flux return [11].

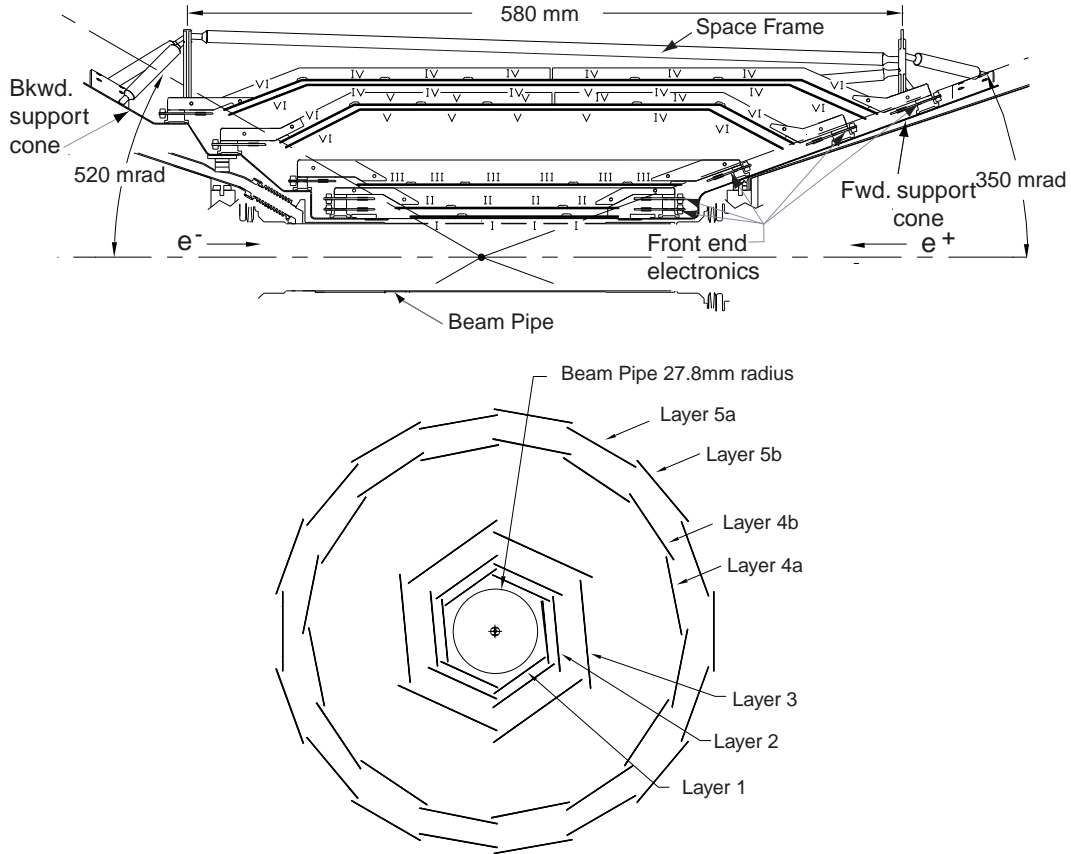


Figure 3.4: Longitudinal (top) and radial (bottom) sections of the silicon vertex tracker [11]

the reconstruction of charged particle tracks and of secondary decay vertices.

3.2.2 Drift Chamber

The drift chamber (Fig. 3.5) measures the tracks and momenta of charged particles. It is also used to identify charged particles using the specific energy loss dE/dx . The drift chamber is a multi-wire chamber with an inner radius of 26.6 cm, an outer radius of 80.9 cm and a length of 280 cm in z -direction. It consists of 40 layers of nearly hexagonal cells. To obtain longitudinal information wires in 24 layers are placed at small angles to the z -axis. Low-mass gold plated tungsten-rhenium wires and a 80:20 mixture of helium and iso-butane drift gas are used to minimize multiple scattering in the drift chamber. The transverse

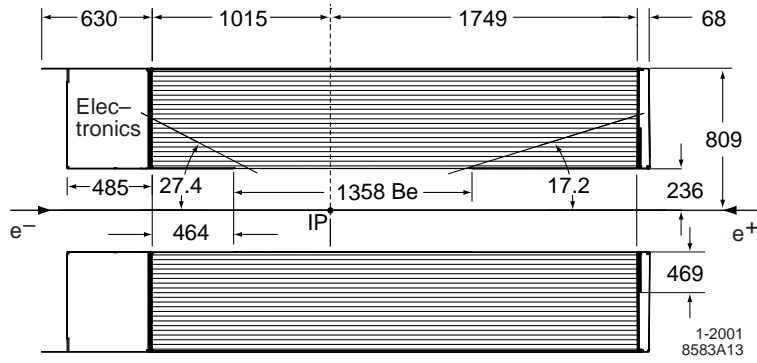


Figure 3.5: Longitudinal section of the drift chamber [11]

momentum p_t resolution of the reconstructed track is:

$$\frac{\sigma(p_t)}{p_t} = (0.13 \pm 0.001) \% \cdot p_t + (\pm 0.03) \%$$

3.2.3 Detector of Internally Reflected Čerenkov Light

The Čerenkov detector is used for particle identification and its main feature is the separation between pions and kaons in the momentum range from about 500 MeV/ c to the kinematic limit of 4.5 GeV/ c . It uses so-called Čerenkov photons that are emitted by charged particles traversing the Čerenkov detector's active material with a velocity higher than the speed of light in this material. The photons are emitted at an angle Θ_C with respect to the direction of the charged particle's track,

$$\cos(\Theta_C) = \frac{1}{\beta n} = \frac{\sqrt{1 + m/p}}{n},$$

with p and m being the momentum and mass of the charged particle and the refractive index n of the medium traversed.

The Čerenkov detector (Fig. 3.6) consists of 144 4.9 m long quartz bars with a rectangular cross section (1.7 cm \times 3.5 cm) and a refractive index $n = 1.453$. In the bars the Čerenkov light is produced and also transported by total internal reflection, preserving the angle of emission. Mirrors are placed at the forward end of the bars mirrors to reflect the light to the instrumented back. Photons arriving at the instrumented end emerge into a water filled expansion region and are then detected with an array of about 11,000 photo multipliers placed about 1.2 m from the bars' ends. The expected light pattern is a conical section where the cone opening angle is the Čerenkov angle Θ_C .

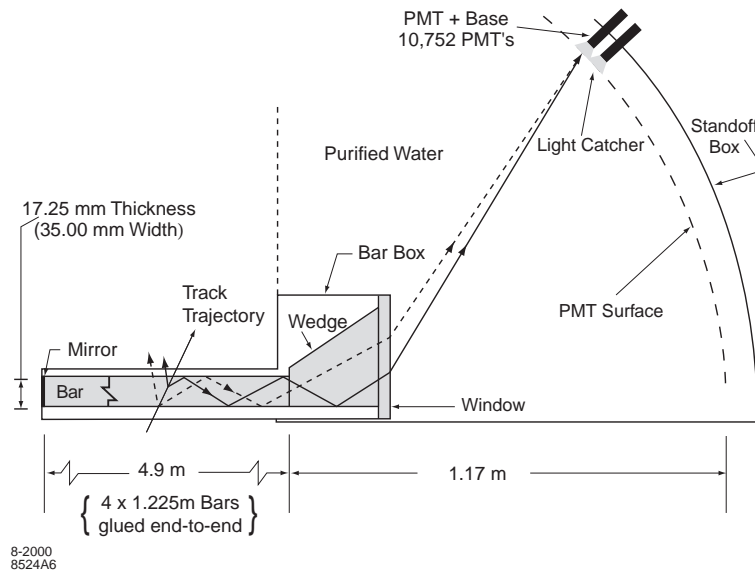


Figure 3.6: Schematic longitudinal section of the Čerenkov detector, illustrating its working principle [11]

3.2.4 Electromagnetic Calorimeter

The electromagnetic calorimeter measures the energy, position and transverse shape of electromagnetic showers. It is designed to detect photons in the energy range of 20 MeV to 9 GeV and can be used to detect particles like neutral pions that mainly decay into photons. It can also contribute to the particle identification by measuring E/p together with the drift chamber.

It consists of 6580 thallium-doped cesium iodide (CsI(Tl)) crystals arranged in 56 rings (Fig. 3.7) in the barrel around the beam axis. Eight rings cover the forward end-cap. The electromagnetic calorimeter covers the angular range from 15.8° to 141° . Electromagnetic showers produce scintillation light in the crystals that is read out with silicon photo diodes. Generally, a particle entering the electromagnetic calorimeter deposits energy in several crystals. The combination of all crystals belonging to a single shower is called cluster in the following.

3.2.5 The Instrumented Flux Return

The iron flux return of the superconducting coil is instrumented with resistive plate chambers and limited streamer tubes. It consists of three parts, the cylindrical barrel surrounding the other subdetectors and a pair of end doors to cover the forward and backward region. It is used to detect muons and neutral hadrons like K_L^0 .

energy deposition in the calorimeter and

- the Čerenkov angle Θ_C measured in the Čerenkov detector

to estimate the likelihood for the particle being an electron. The selector correctly identifies electrons in the laboratory momentum range $1 \text{ GeV}/c < p_{lab}^e < 5 \text{ GeV}/c$ with an efficiency of about 94% and a missidentification probability well below 1%. For smaller momenta the efficiency falls below 75% and the misidentification probability rises slightly.

Muon Identification

In contrast to electrons that deposit all their energy in the electromagnetic calorimeter, muons are minimum ionizing particles. They only lose small amounts of their energy while traversing all the inner detectors and can only be detected in the muon chambers of the instrumented flux return.

The so-called “muon selector” is based on the output of a neural-network⁶ trained to identify muons [14]. It uses the following detector information as input variables:

- the energy E_{cal} deposited in the electromagnetic calorimeter
- the number of layers in the instrumented flux return hit by the track
- flight lengths information to distinguish between muons that traverses the muon chambers and hadrons that are absorbed
- the average multiplicity \bar{m} of hit strips per instrumented flux return layer and its standard deviation $\sigma_{\bar{m}}$
- $\chi^2/d.o.f.$ ⁷ of each the fit of the track measured in the drift chamber and the instrumented flux return

The selector has a muon identification efficiency of about 70% and a muon-as-pion missidentification probability of 2%.

Charged Kaon Identification

A so-called “kaon selector” designed to identify kaons is used to veto kaons [15]. It is based on a likelihood method like the electron selector discussed before and has the same input variables. In addition to that, a kaon is required not to be identified as an muon and for momenta $p < 0.04 \text{ GeV}/c$ not to be identified as an electron.

⁶Neural-networks are described in chapter 5

⁷degrees of freedom

Particle Identification in Monte-Carlo and Data

The performance of the particle identification “selectors” on real data is estimated on control samples, where the identity of the particle can be inferred from kinematics, the event topology, etc. without the use of particle identification criteria, e.g. in case of the electron selector, a sample of almost pure electrons is obtained from radiative Bhabha events [13] and then used to measure the electron selector’s efficiency on data.

The efficiencies on data differ from the ones obtained in the Monte-Carlo (MC) simulation. Therefore in order to compare data to MC it is necessary to weight MC events by a so-called particle identification weight, which is the ratio of the data to the MC efficiencies. The *BABAR* particle identification group [16] provides these weights in dependence of the momentum, the polar and the azimuthal angle, and they are applied here accordingly.

Chapter 4

Data and Monte-Carlo Samples

4.1 Data Samples

This analysis uses data corresponding to a total integrated “on-resonance” luminosity of 347 fb^{-1} , equal to about 382 million $B\bar{B}$ pairs taken at the $\Upsilon(4S)$ resonance, which corresponds to a center of mass energy of $\sqrt{s} = 10.58 \text{ GeV}$. In addition to this, another sample with 35 fb^{-1} total integrated “off-resonance” luminosity recorded 40 MeV below the $\Upsilon(4S)$ resonance is used. The data were recorded with the *BABAR* detector from 1999 to 2006. Table 4.1 shows the amount of data acquired in different run periods.

4.2 Monte-Carlo Samples

Monte-Carlo (MC) simulated data of signal and background modes are used to study properties such as signal and background shapes, selection efficiencies or fit performance. The MC data is produced in three steps:

- Events are generated according to the cross sections, kinematic properties and decay branching fractions of the decays involved.

	$\int L$ On-Res. [fb^{-1}]	$\int L$ Off-Res. [fb^{-1}]	$N_{B\bar{B}}$ [10^6] On-Peak
Run1	20.4	2.6	22.4
Run2	61.1	6.9	67.5
Run3	32.3	2.5	35.6
Run4	100.3	10.1	110.5
Run5	133.0	13.1	146.9
Total	347.2	35.2	382.9

Table 4.1: *Integrated luminosity for on-resonance and off-resonance data and number of $B\bar{B}$ pairs recorded in the different run periods*

MC	Events [10^6]	$\int L$ [fb^{-1}]	σ [nb]	BF [10^{-4}]
$c\bar{c}$	584.58	449.7	1.30	
$u\bar{u}, d\bar{d}, s\bar{s}$	648.12	310.1	2.09	
B^+B^- generic	539.74	1028.1	0.525	
$B^0\bar{B}^0$ generic	541.79	1032.0	0.525	
$B^+ \rightarrow \eta\ell^+\nu$	0.31	7029.5		0.84
$B^+ \rightarrow \omega\ell^+\nu$	1.54	22564.1		1.30
$B^+ \rightarrow \eta'\ell^+\nu$	1.54	34920.6		0.84
$B^+ \rightarrow \rho^0\ell^+\nu$	0.31	5134.6		1.15
$B^+ \rightarrow \pi^0\ell^+\nu$	0.31	8201.1		0.72
$B^0 \rightarrow \rho^-\ell^+\nu$	1.54	13707.2		2.14
$B^0 \rightarrow \pi^-\ell^+\nu$	0.31	4406.5		1.34
$B^+ \rightarrow u\ell\nu$	8.07	8242.1		18.65
$B^0 \rightarrow u\ell\nu$	8.17	8541.1		18.22

Table 4.2: Overview of the signal and the different background MC samples. For all samples the number of generated events and the corresponding integrated luminosities are given. In case of the $q\bar{q}$ -continuum and the generic B samples the event number is just the product $N = \int L \cdot \sigma$. In the exclusive B samples the other B -meson decays generically. Here the event numbers are calculated with the specific branching fractions.

- The interaction of the resulting particles with the detector is simulated with the GEANT package [17].
- The tracks and clusters from the detector simulation are reconstructed in the same way real data are.

An overview of the different MC samples used is given in Tab. 4.2.

4.2.1 Classification of Monte-Carlo Events

The signal mode in this analysis is $B^+ \rightarrow \eta\ell^+\nu_\ell$, with the lepton ℓ either being an electron or a muon and with the η decaying into three pions ($\eta \rightarrow \pi^+\pi^-\pi^0$). A number of other physics processes may mimic these signal decays through errors in reconstruction. The simulated MC backgrounds are divided into different sources, depending on the origin of the candidate lepton. The different sources are defined in the following and a graphical overview is given in Fig. 4.1.

Signal Monte-Carlo Sample

The signal MC sample for $B^+ \rightarrow \eta\ell^+\nu_\ell$ was generated with a flat four-momentum transfer q^2 -distribution and a branching fraction $\mathcal{B}(B^+ \rightarrow \eta\ell^+\nu_\ell)_{\text{MC}} = 8.4 \cdot 10^{-5}$

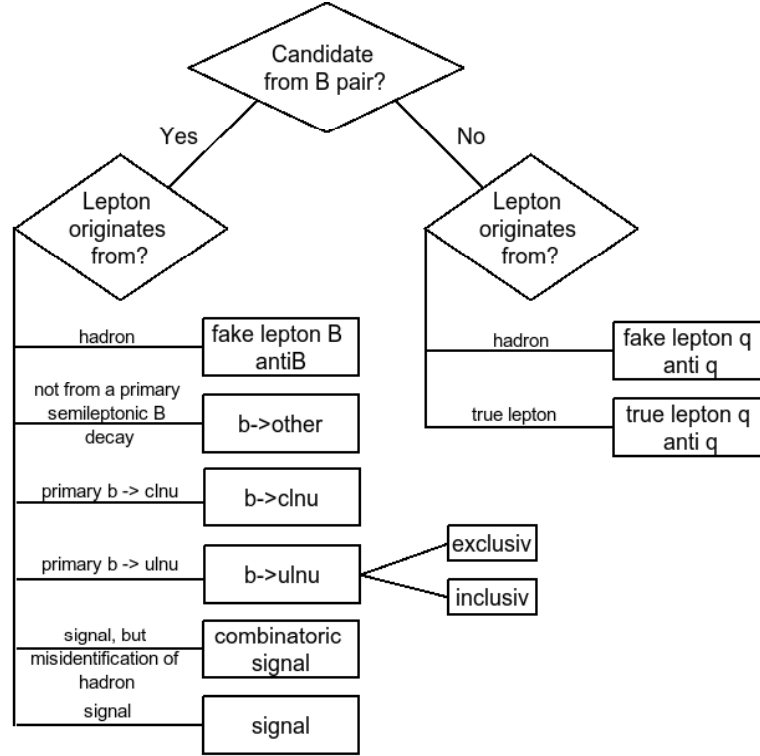


Figure 4.1: *Classification of MC sources*

is used in the MC simulation.

The decision to generate a flat q^2 -spectrum was made to allow for easy changes of the form-factor model. To use one of the specific models discussed in chapter 2, the generated events must be reweighted in q^2 according to the model chosen. For this analysis the light-cone sum rule form-factor model by Ball and Zwicky [8] (Ball04) is used. A generator level comparison of the generated flat q^2 -spectrum, the one reweighted to the model used (Ball04) and the one reweighted to the ISGW2 [7] model, is shown in Fig. 4.2.

Combinatoric Signal

For some MC studies it is interesting to distinguish true signal, where the lepton, the η and its three pion daughters were reconstructed correctly, from so-called combinatoric signal, where either the η is not coming from the signal B or where the η is not reconstructed from the correct daughter particles. The difference is clearly visible in the three pions invariant mass distributions shown in Fig. 4.3. Here only the signal MC sample is used.

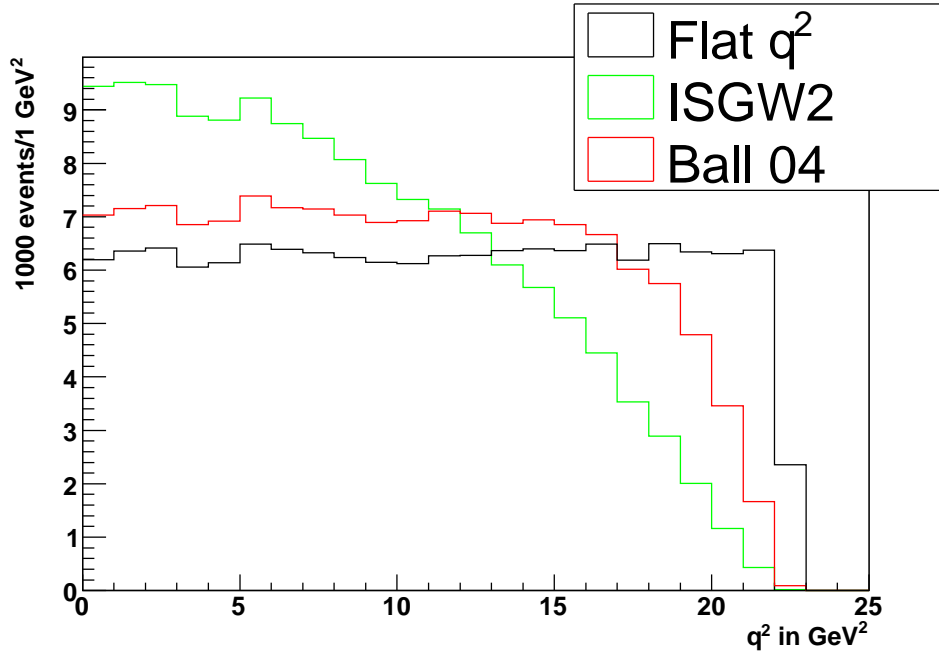


Figure 4.2: Generated flat q^2 distribution for $B^+ \rightarrow \eta \ell^+ \nu_\ell$ and the reweighted distributions for the Ball04 and the ISGW2 form-factor models

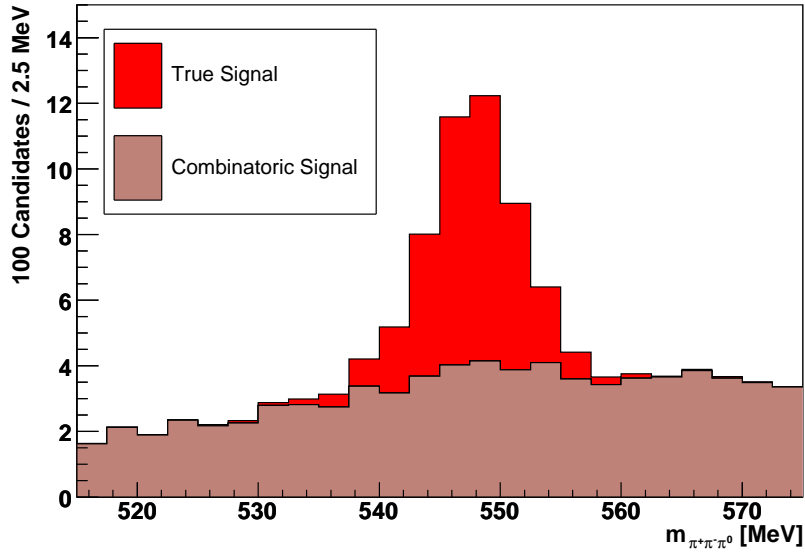


Figure 4.3: Invariant mass of the $\eta \rightarrow \pi^+ \pi^- \pi^0$ candidates for true and combinatoric signal in the signal MC sample without any cuts applied

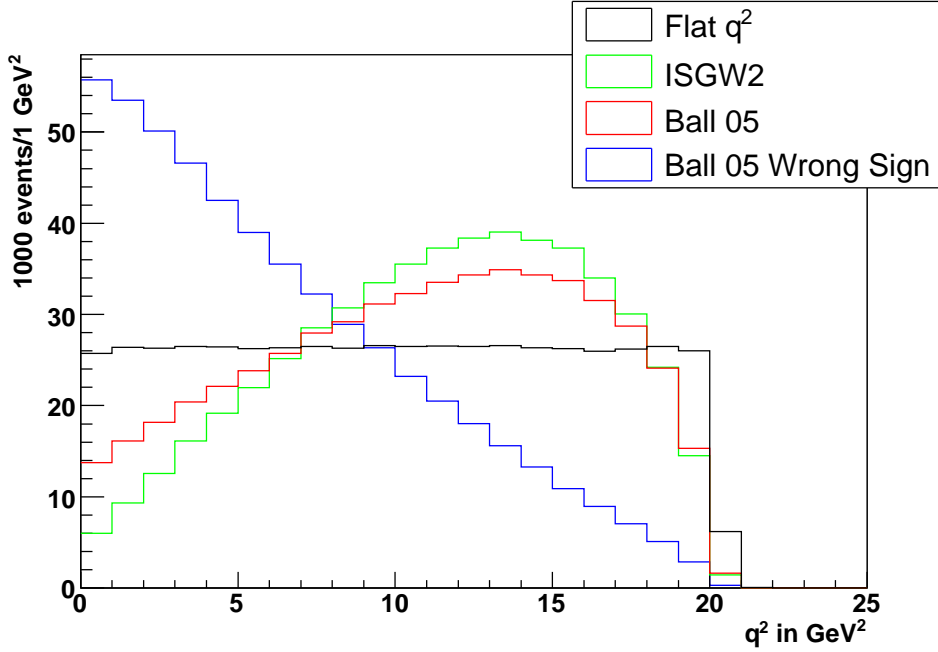


Figure 4.4: Generated flat q^2 distribution for $B^+ \rightarrow \omega \ell^+ \nu_\ell$ and the reweighted distributions for the Ball05 (with and without wrong sign) and the ISGW2 form-factor models

Charmless Semileptonic B-Decays

Exclusive samples of $B^0 \rightarrow \pi^- \ell^+ \nu_\ell$, $B^+ \rightarrow \pi^0 \ell^+ \nu_\ell$, $B^0 \rightarrow \rho^- \ell^+ \nu_\ell$, $B^+ \rightarrow \rho^0 \ell^+ \nu_\ell$, $B^+ \rightarrow \omega \ell^+ \nu_\ell$ and $B^+ \rightarrow \eta' \ell^+ \nu_\ell$ also produced with a flat q^2 -distribution are used. They are reweighted in q^2 accordingly, either using the Ball04 form-factor model for light pseudoscalar mesons [8] or the Ball05 [18] form-factor model for light vector mesons, both calculated from light-cone sum rules. In case of $B^+ \rightarrow \omega \ell^+ \nu_\ell$ due to a typing error in the theory publication [18] a wrong sign occurred in the form-factor calculation [19]. This significantly reduced the amount of $B^+ \rightarrow \omega \ell^+ \nu_\ell$ background events passing this analysis's selection criteria. The q^2 -distribution for this channel before and after the sign correction is shown in Fig. 4.4.

In addition, an inclusive $B \rightarrow u \ell \nu$ sample of non-resonant charmless semileptonic B -decays generated with a smooth hadronic mass spectrum is used. Correctly combining this inclusive sample with the exclusive ones is not a simple task, as the total hadronic mass M_X spectrum of $B \rightarrow u \ell \nu$ cannot be calculated. Currently the best solution to this problem is the so-called “hybrid model” [20]. To give the correct $B \rightarrow u \ell \nu$ branching fraction the overall normalization of the inclusive sample is adjusted when it is combined with the resonant samples. Furthermore the sample is reweighted in bins of q^2 , the lepton energy E_ℓ^* in the $\Upsilon(4S)$

frame and the hadron mass M_X . This is done in such a way that the sum of the weighted resonant and non-resonant samples in each bin approximates the fraction of the unweighted non-resonant sample alone. Fig. 4.5 shows the obtained mass M_X spectrum of the hadronic $u\bar{u}$ -system.

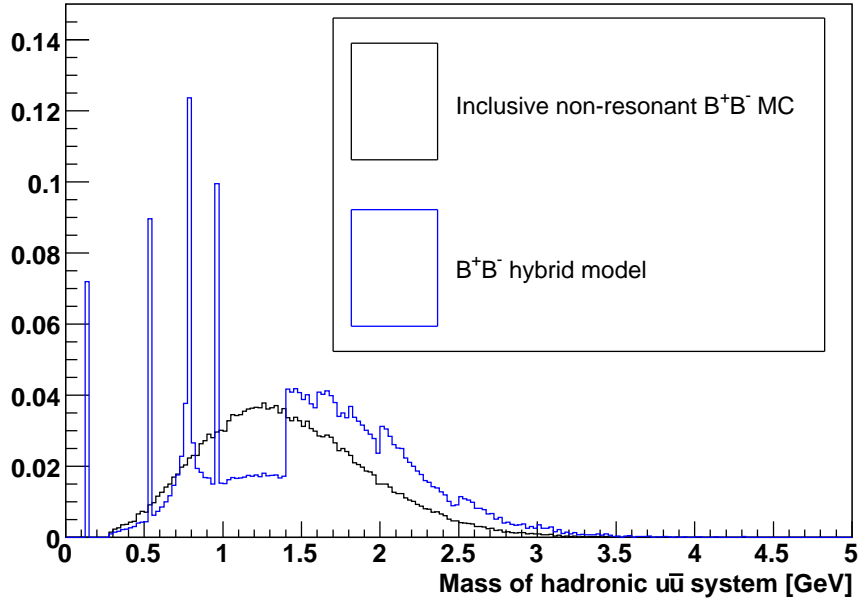


Figure 4.5: Mass of the hadronic $u\bar{u}$ -system in charmless semileptonic B-Meson decays, for the unweighted inclusive non-resonant sample and for the hybrid model

$B\bar{B}$ Background

The remaining sources of background from B decays contain events where the reconstructed lepton is a true lepton coming from

- a semileptonic decay of the form $B \rightarrow X_c \ell \nu^1$, called $b \rightarrow c \ell \nu$ in the following
- one of the B-meson daughters instead of coming directly from the B-meson itself, such as $B \rightarrow J/\Psi X \rightarrow \ell^+ \ell^- X^2$, called $b \rightarrow other$ in the following.

Events where the reconstructed lepton is actually a misidentified hadron from a B decay are called $B\bar{B}$ fake in the following.

¹ X_c stands for a hadron containing a charm quark.

² X stands for additional particles.

Continuum Background

Simulated $e^+e^- \rightarrow q\bar{q}$ events with $q = u, d, s, c$ are divided into two sources: $q\bar{q}$ *true* where the lepton has been reconstructed correctly and the $q\bar{q}$ *fake* where the reconstructed lepton is a missidentified hadron.

Pure QED backgrounds like Bhabha scattering or $e^+e^- \rightarrow \tau^+\tau^-$ were studied and found to be negligible in the $B^0 \rightarrow \pi^-\ell^+\nu_\ell$ analysis [2] and are therefore not considered in this analysis.

4.3 Data Monte-Carlo Comparison

As the statistics of the MC samples are different (in fact much higher) from the statistics of the data sample, the MC samples need to be normalized to compare them with data. For all MC samples where $B\bar{B}$ -meson pairs were generated this is done by normalizing the MC samples according to their branching fractions to the total number of $B\bar{B}$ -pairs produced in data. This method is more precise than a simple cross section normalization. The actual center-of-mass energy is only known to a finite experimental precision, but as the data are taken on the $\Upsilon(4S)$ resonance, a slight change in the energy also significantly changes the crosssection. Therefore, the number of $B\bar{B}$ -pairs $N^{B\bar{B}}$ is estimated using standard BABAR B -counting tools [21]. The scale factor $f_{\text{scale}}^{B \rightarrow X}$ of a MC sample $B \rightarrow X$ with branching ratio $\mathcal{B}(B \rightarrow X)$ is:

$$f_{\text{scale}}^{B \rightarrow X} = \frac{N_{\text{data}}^{B\bar{B}}}{N_{(B \rightarrow X)\text{-MC}}^{B\bar{B}}} \cdot \mathcal{B}(B \rightarrow X)$$

The continuum samples are normalized to the integrated data luminosity $\int L_{\text{data}}$ according to their cross section σ , i.e.:

$$f_{\text{scale}}^{\text{non-}B\bar{B}} = \frac{\int L_{\text{data}}}{N_{\text{generated}}^{\text{non-}B\bar{B}}} \cdot \sigma_{\text{non-}B\bar{B}}$$

The branching ratios and cross sections used are listed in Tab. 4.2. The data luminosity is shown in Tab. 4.1.

As described in chapter 3.2.6, the particle identification criteria used in this analysis have different identification efficiencies in real data and in the MC simulation. This effect is corrected for by applying the ratios of the identification efficiencies on data and the MC simulation, as weights to the MC events.

Fig. 4.6 illustrates a typical plot of the different MC sources and the data as it is used in this analysis. The sample is divided into $B^+ \rightarrow \eta e^+\nu_{e^+}$ and $B^+ \rightarrow \eta\mu^+\nu_{\mu^+}$ samples, where the reconstructed lepton is an electron or muon respectively. The data points are shown with their statistical errors. The different MC samples are color-coded. The signal sample is normalized to the fraction

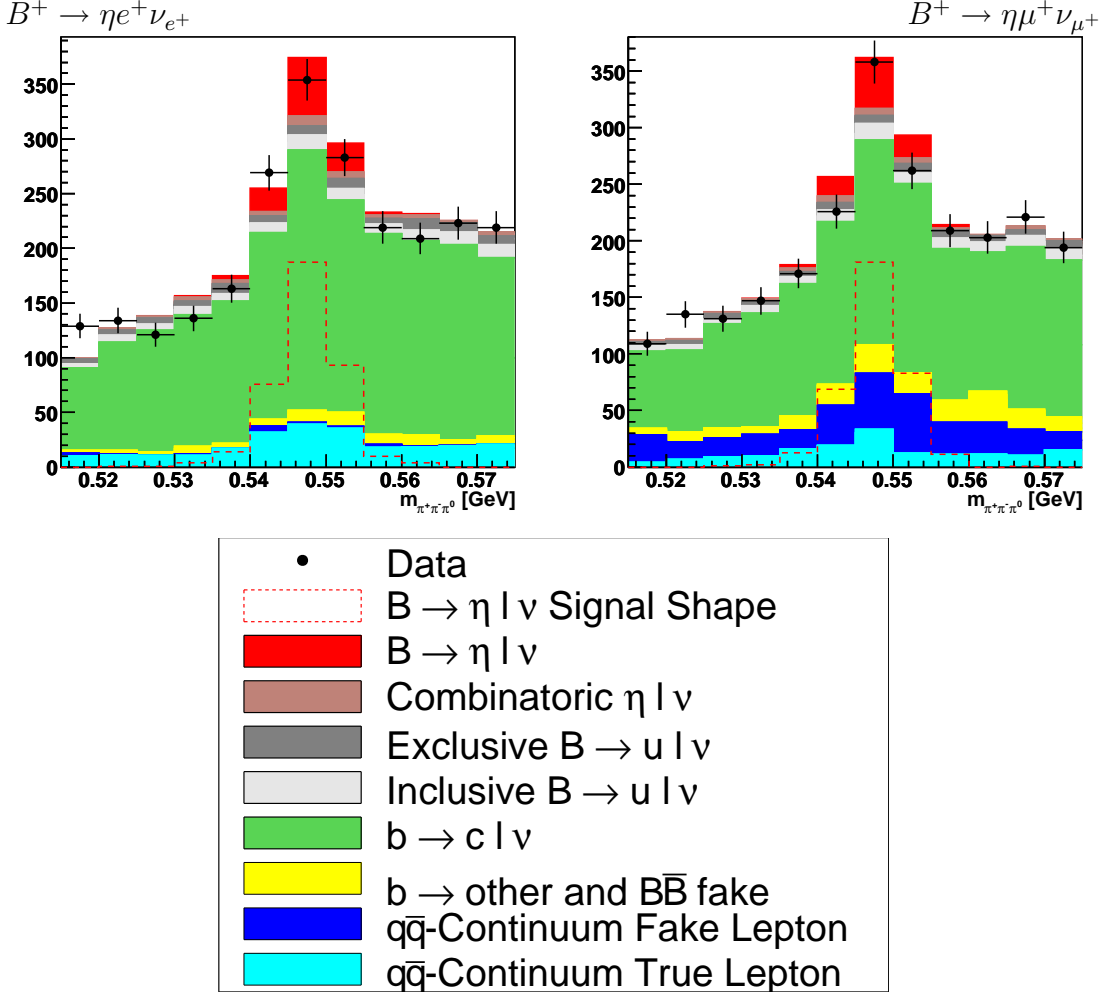


Figure 4.6: A typical data and MC background distribution (The reconstructed η mass $m_{\pi^+\pi^-\pi^0}$ with the final selection applied). The data points are shown with their statistical errors. The MC background samples are color-coded. The signal sample is normalized to the fraction measured in this analysis. The red dashed line is the $B^+ \rightarrow \eta l^+ \nu_l$ signal with an arbitrary normalization, used to illustrate the signal shape. The sample is divided into a $B^+ \rightarrow \eta e^+ \nu_{e^+}$ subsample, where an electron is reconstructed (left) and a $B^+ \rightarrow \eta \mu^+ \nu_{\mu^+}$, where a muon is reconstructed (right).

measured in this analysis (chapter 6). The red dashed line is the signal with an arbitrary normalization, used to illustrate the signal shape, as without applying any selection the signal is hardly visible.

4.3.1 Continuum Monte-Carlo and Off-Resonance Data

The statistics of the continuum background MC samples used in the analysis are relatively small. To check their normalization, they can be compared to the off-resonance data sample, which is recorded with a center-of-mass energy 40 MeV below the $\Upsilon(4S)$ resonance. Hence the center-of-mass energy is below the $B\bar{B}$ -pair production threshold and therefore the sample only contains $q\bar{q}$ -continuum events. Fig. 4.7 shows the reconstructed invariant mass of $\eta \rightarrow \pi^+\pi^-\pi^0$ candidates³ in the $B \rightarrow \eta\nu_e$ and the $B \rightarrow \eta\mu\nu_\mu$ final state. In case of the $B \rightarrow \eta\nu_e$ -sample the

$B^+ \rightarrow \eta e^+\nu_{e^+}$

$B^+ \rightarrow \eta\mu^+\nu_{\mu^+}$

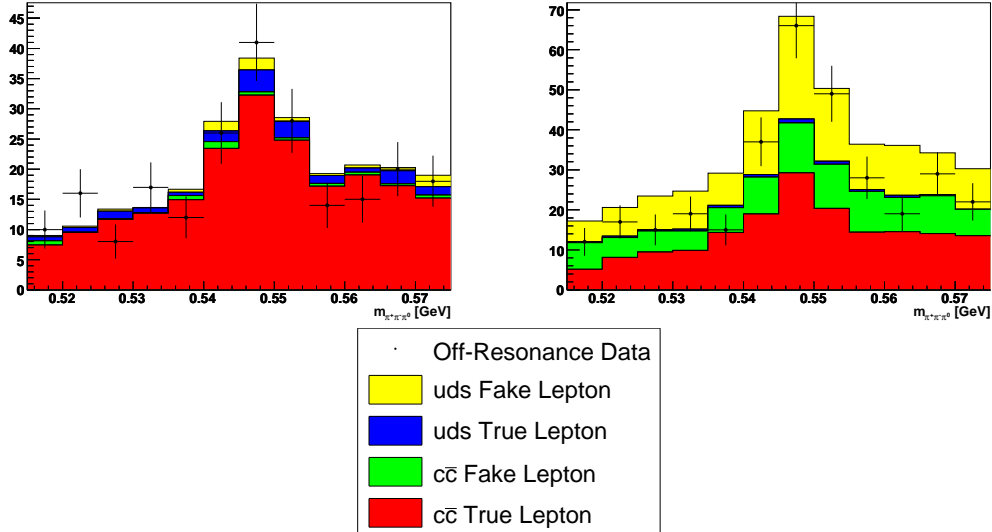


Figure 4.7: Comparison of off-resonance data and continuum MC samples divided into $B^+ \rightarrow \eta e^+\nu_{e^+}$ and $B^+ \rightarrow \eta\mu^+\nu_{\mu^+}$. The distribution shown is the reconstructed η mass $m_{\pi^+\pi^-\pi^0}$.

MC simulation seems to describe the data properly, but in the $B \rightarrow \eta\mu\nu_\mu$ -sample the MC simulation systematically over-estimates the event yield in real data. A fit of the MC histograms to the data histogram⁴ yields normalization factors of $f_{q\bar{q}}^e = (94.8 \pm 6.3)\%$ for the $B \rightarrow \eta\nu_e$ and $f_{q\bar{q}}^\mu = (78.9 \pm 4.4)\%$ for the $B \rightarrow \eta\mu\nu_\mu$ sample.

³The selection criteria applied are described later in chapter 5.2.

⁴The fit is not performed for the invariant mass distribution – used for illustration here – but for the same distribution later (chapter 6) used to extract the $B^+ \rightarrow \eta\ell^+\nu_\ell$ branching fraction. This distribution is of technical nature and therefore not shown here.

In the $B \rightarrow \eta e \nu_e$ -sample the scaling factor is compatible with one. The $B \rightarrow \eta \mu \nu_\mu$ -sample contains about 60% of fake muons (hadrons identified as muons), while there are only about 5% fake electrons in the other sample. The discrepancy in the muon-sample is probably due to the bad description of the fake rate in the simulation.

The continuum MC is rescaled with these factors for all of the following analysis steps.

4.3.2 Monte-Carlo and On-Resonance Data

Comparing the MC expectation with on-resonance data shows that the MC simulation systematically over-estimates the event yield in data, independent of the distribution considered and the selection criteria applied. To illustrate the problem the distribution of the $\eta \rightarrow \pi^+ \pi^- \pi^0$ invariant mass is shown in Fig. 4.8. The discrepancy can be traced back to the $b \rightarrow c \ell \nu$ background, where the MC expectation is about 15% too high. The shapes of the distributions are described reasonably well, however, some distributions show discrepancies in purely background dominated regions. Due to the limited time, it was not possible to understand the difference in the context of this thesis.

To overcome the problem in the MC modeling, selection criteria (see chapter 5.2) are used to reject events from purely background dominated regions that show discrepancies between data and the simulation. These criteria are not affecting the signal acceptance, but improve the agreement of the shapes significantly. To correct the overall normalization, the $b \rightarrow c \ell \nu$ background fraction is not taken from the MC simulation, but determined from the data in a simultaneous fit of signal $B^+ \rightarrow \eta \ell^+ \nu_\ell$ and $b \rightarrow c \ell \nu$ background (chapter 6). The fractions are $f_{\text{signal}} = (0.773 \pm 0.177)$ and $f_{b \rightarrow c \ell \nu} = (0.889 \pm 0.039)$.

In the following, both the signal $B^+ \rightarrow \eta \ell^+ \nu_\ell$ and the $b \rightarrow c \ell \nu$ background are scaled by the fractions determined in the fit, when data and MC are shown.

As the origin of the “scaling factor” could not be determined, the full MC/data discrepancy is treated as an additional systematic uncertainty (chapter 7).

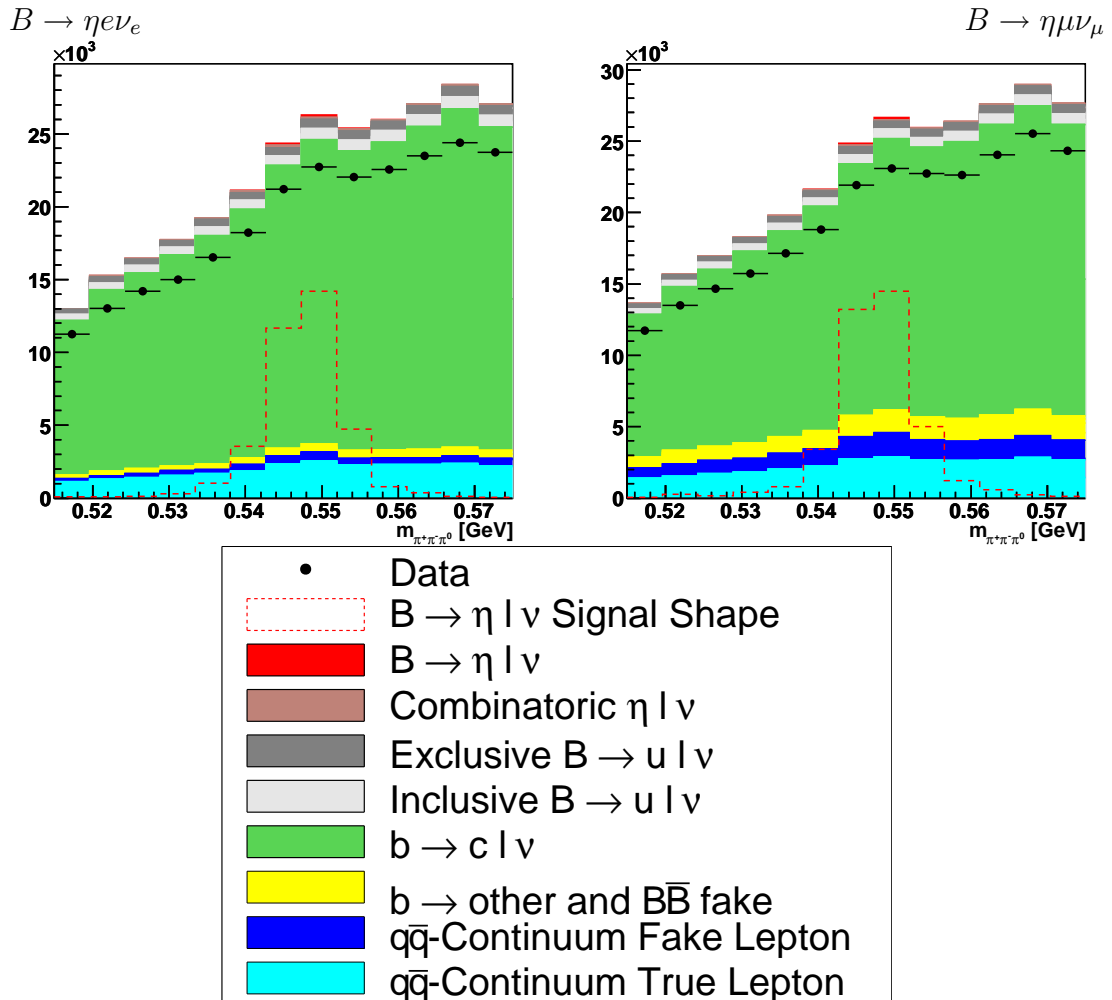


Figure 4.8: Distribution of the invariant $\eta \rightarrow \pi^+\pi^-\pi^0$ mass without scaling of the $b \rightarrow c l \nu$ background. the overestimation of the data event yield by the MC simulation can be seen.

Chapter 5

Event Selection

Events are selected in several steps. The first selection criteria are of technical nature and are performed within the computing framework of the SLAC $B^0 \rightarrow \pi^- \ell^+ \nu_\ell$ analysis [2] to reduce the size of the data sample. These criteria are described in chapter 5.1. In addition to that, there are selection criteria specific to this analysis. They are discussed in chapter 5.2. Then the final selection, described in chapter 5.3, is performed by using a multivariate analysis technique - namely neural-networks.

5.1 Preselection

The preselection is performed during reconstruction at SLAC computing facilities. It is performed in three steps and with each step the amount of disk space and computing time is reduced. As the selection criteria of the last step are more restrictive and cover the less restrictive ones, the criteria of the first two steps are not described in detail. The steps are briefly described in the following section 5.1.1 and the selection criteria are discussed in section 5.1.2.

5.1.1 Computational Steps

First, a so-called skim is used. It is a filter that selects events of a certain topology. The skim used here was created to study exclusive semileptonic B decays [22]. An event is kept if it passes the selection criteria of at least one of the modes included.

Those are: $B^0 \rightarrow \pi^- \ell^+ \nu_\ell$, $B^+ \rightarrow \pi^0 \ell^+ \nu_\ell$, $B^+ \rightarrow \eta \ell^+ \nu_\ell$, $B^+ \rightarrow \eta' \ell^+ \nu_\ell$, $B^0 \rightarrow \rho^- \ell^+ \nu_\ell$, $B^+ \rightarrow \rho^0 \ell^+ \nu_\ell$, $B^+ \rightarrow \omega \ell^+ \nu_\ell$.

Within work for this thesis the efficiencies of the skim were estimated for all different MC samples used by running it over a couple of 100000 events for each sample and counting the event numbers before and after the filter. The results of this study can be found in Table 5.1. For data the efficiency is 1.55% for the on-resonance and 0.57% for the off-resonance sample [22].

Sample	Events before filter	Events after filter	Ratio (After/Before)
$B^0 B^0$ generic	2499998	275736	11.0%
$B^+ B^-$ generic	2499998	298817	12.0%
$c\bar{c}$	1625000	47780	2.9%
$u\bar{u}, d\bar{d}, s\bar{s}$	1750000	28530	1.6%
$B^0 \rightarrow u\ell\nu$	622328	263558	42.4%
$B^+ \rightarrow u\ell\nu$	622381	267008	42.9%
$B^0 \rightarrow \pi^-\ell^+\nu_\ell$	309088	176457	57.1%
$B^+ \rightarrow \pi^0\ell^+\nu_\ell$	309041	167089	54.1%
$B^0 \rightarrow \rho^-\ell^+\nu_\ell$	1218669	629522	51.7%
$B^+ \rightarrow \rho^0\ell^+\nu_\ell$	309091	167142	54.1%
$B^+ \rightarrow \omega\ell^+\nu_\ell$	1449430	740545	51.1%
$B^+ \rightarrow \eta\ell^+\nu_\ell$	309072	150670	48.7%
$B^+ \rightarrow \eta'\ell^+\nu_\ell$	1279235	565725	44.2%

Table 5.1: *Skim efficiencies for the different MC samples.*

In order to prepare data for the exclusive $B \rightarrow X_u \ell \nu$ analyses, the important information of the events selected by the filter is copied to ntuples. Furthermore, information on the neutrino, such as its energy and momentum is calculated. As these ntuples are still too large for common usage, the selection criteria are further tightened and the data is copied to “private ntuples” that only include the information needed for the further analysis, e.g. the properties of the charged lepton. The whole process reduces the amount of diskspace needed to about 25 GB, which can be copied to Heidelberg for further analysis.

Due to the way the analysis is done, it is technically impossible or at least very difficult and time consuming to show the distributions of variables without any selection criteria applied.

5.1.2 Preselection Criteria

The selection of $B^+ \rightarrow \eta \ell^+ \nu_\ell$ candidates is subdivided into the reconstruction of directly and indirectly reconstructable components:

- The so-called Y-system consisting of the charged lepton (e^\pm or μ^\pm) and the η (reconstructed in the $\eta \rightarrow \pi^+ \pi^- \pi^0$ decay mode).
- The neutrino whose four-vector p_ν is approximated by the missing energy and momentum of the whole event .

Criterion	Value
Hits in the DCH	$N_{\text{Hits}} \geq 12$
Polar angle	$0.41 < \Theta_\ell < 2.54$
Momentum	$p < 10 \text{ GeV}/c$
Transverse momentum	$p_T > 0.1 \text{ GeV}/c$
DOCA in the xy-plane	$DOCA_{xy} \leq 1.5 \text{ cm}$
DOCA in z-direction	$DOCA_z \leq 10 \text{ cm}$

Table 5.2: Track requirements, DOCA stands for “Distance of closest approach to the interaction point”.

5.1.3 Y-System

Lepton Reconstruction

First an electron or muon is selected, requiring the following:

- A well reconstructed track, by requiring the criteria listed in Tab. 5.2. These criteria ensure that the track is coming from the initial collision at the interaction point, that there is enough information from the drift chamber to correctly measure its momentum and charge, and that it traverses the sensitive areas of the silicon vertex tracker, the drift chamber, and the well calibrated barrel section of the calorimeter.
- The lepton momentum in the $\Upsilon(4S)$ frame must be $p_\ell^* > 1 \text{ GeV}$, to reduce the amount of fake leptons (which are missidentified hadrons) and to reduce background from true leptons that do not originate from primary B-meson decays.
- The selected track must satisfy the *BABAR* criteria for electron/muon identification, described in chapter 3.2.6.

η -Reconstruction

The η is reconstructed in the $\eta \rightarrow \pi^+\pi^-\pi^0$ channel. The requirements for the charged pions are:

- A well reconstructed track, as in the lepton case, requiring the criteria in Tab. 5.2
- The two charged pions reconstructed must have opposite charge
- The tracks must differ from the track assigned to the lepton.
- The tracks must not pass the kaon selection criteria, described in chapter 3.2.6. A study of this veto is presented in Appendix A.

The neutral pion is reconstructed in the $\pi^0 \rightarrow \gamma\gamma$ channel and the following requirements are made:

- Each photon has a minimum energy of 30 MeV, no track pointing to the photon's cluster and a maximal lateral moment (defined in chapter 3.2.6) of 0.8. The lateral moment describes the shower shape of clusters and is used to identify clusters consistent with an electromagnetic energy deposition
- An invariant mass of $0.10 \text{ GeV}/c^2 < m_{\pi^0} < 0.16 \text{ GeV}/c^2$

The invariant mass $m_{\pi^+\pi^-\pi^0}$ of η -candidates is required to be within $0.515 \text{ GeV}/c^2 < m_{\pi^+\pi^-\pi^0} < 0.575 \text{ GeV}/c^2$.

Y-Candidates

The signal lepton is combined with each $\eta \rightarrow \pi^+\pi^-\pi^0$ combination that passes the selection, so that there can be more than one signal Y-candidate per event. Only a small amount of events with more than one candidate ($\approx 2\%$) are left after the final selection and the effect is well described in the simulation (Fig. 5.1). Only Y candidates satisfying at least one of the requirements $|p_\eta^*| \geq 1.3 \text{ GeV}/c$,

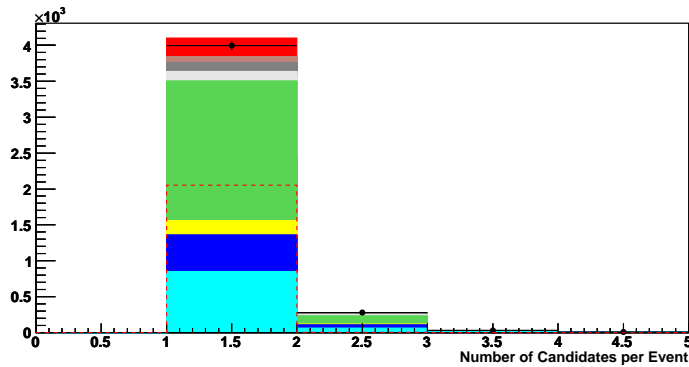


Figure 5.1: *Distribution of the number of candidates per event with the final selection applied. For multiple candidates per event the data is well described by the simulation. For the legend see Fig. 5.2.*

$|p_\ell^*| \geq 2.2 \text{ GeV}/c$ and $|p_\eta^*| + |p_{\text{lepton}}^*| > 2.8 \text{ GeV}/c$ are selected. This 2-dimensional cut rejects about 80% of the $B\bar{B}$ -background and more than 90% of the $q\bar{q}$ -continuum, while about 30% of the signal are kept. It is further described in [22]. All the tracks belonging to one Y-candidate are fit to a common vertex and the $\chi^2/d.o.f.$ ¹ probability of the fit (used later) is computed.

¹degrees of freedom

Kinematic Consistency Requirement

To test whether the four-momentum p_Y of the Y-candidate is consistent with the one expected from a $B^+ \rightarrow \eta \ell^+ \nu_\ell$ decay the neutrino's four-momentum

$$p_\nu^2 = 0 = (p_B - p_Y)^2 = M_B^2 + M_Y^2 - 2(E_B E_Y - |\vec{p}_B| |\vec{p}_Y| \cos(\Theta_{BY})).$$

is used.

The angle Θ_{BY} between the Y-candidate and the B-meson can be determined from the B-momentum \vec{p}_B and the B-energy E_B :

$$\cos(\Theta_{BY}) = \frac{2E_B E_Y - M_B^2 - M_Y^2}{2|\vec{p}_B| |\vec{p}_Y|}$$

Physical solutions should be between -1 and 1. Taking into account the finite resolution of the measured quantities, events are required to have $-1.2 < |\cos \Theta_{BY}| < 1.1$. The resulting distribution is shown in Fig. 5.2. The data are well described by the MC simulation. This is a good example for a distribution where a one-dimensional cut would not increase the signal fraction very effectively. However, in a multivariate analysis multi-dimensional correlations can be exploited and therefore this distribution can be used to help distinguish signal from background.

5.1.4 Neutrino Reconstruction

The neutrino cannot be detected directly. But its energy and momentum can be reconstructed indirectly by subtracting the energies and momenta of all tracks and clusters in the event from the initial beam energy and momentum. As the other B-meson can also decay in leptons or as particles might be lost in the beam pipe etc. the resolution of the neutrino four-momentum is limited.

Tracks Used for Visible Momentum Reconstruction

The tracks used to reconstruct the visible momentum in the event are required to be within the sensitive areas of the silicon vertex tracker, the drift chamber and the calorimeter (polar angle $0.41 < \Theta_\ell < 2.54$) and have a momentum $p < 10$ GeV. To ensure that the corresponding particles come from the initial collision a distance of closest approach to the interaction point of less than 1.5 cm in the xy-plane and of less than 10 cm in z-direction is required.

In addition to that, clean up requirements described in [23] are used to suppress multiple usage of the same track for different particles (so-called ghosts), and of particles that are curling in the drift chamber and therefore produce several track candidates (so-called loopers).

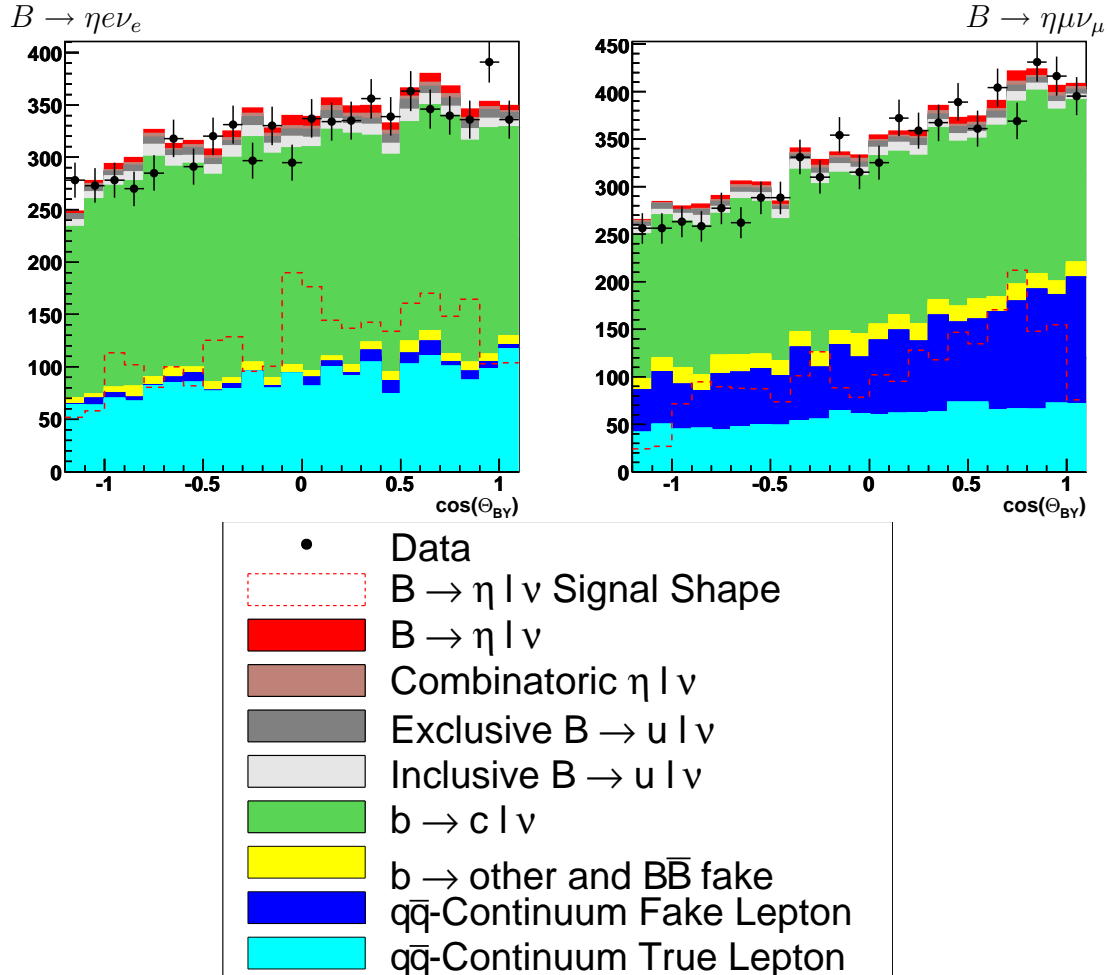


Figure 5.2: *Distribution of the cosine of the angle between the Y -candidate and the B -meson $\cos(\Theta_{BY})$ with the analysis selection (5.2) applied. The data are well described by the MC simulation. This is a good example for a distribution where a one-dimensional cut would not increase the signal fraction very effectively. However, in a multivariate analysis multi-dimensional correlations can be exploited and therefore this distribution can be used to help distinguish signal from background.*

Neutral Clusters Used for Visible Energy Reconstruction

The neutral clusters are required to

- have a minimum energy of 30 MeV
- have a lateral moment l , defined in 3.2.6, smaller than 0.8
- have no track pointing to the cluster

Determination of the Neutrino's Four-Vector

After good clusters and tracks have been selected, the neutrino's four-vector can be calculated

$$p_\nu = (E_{\text{miss}}, \vec{p}_{\text{miss}}) = (E_{\text{beams}}, \vec{p}_{\text{beams}}) - \left(\sum_i E_i, \sum_i \vec{p}_i \right)$$

with the \vec{p}_i and the E_i being the three-momenta and energies of the i^{th} track² or cluster measured in the laboratory frame. E_{beams} and \vec{p}_{beams} are the sum of the energies and three-momenta of the two colliding beams. A missing momentum p_{miss} of at least 0.3 GeV in the laboratory frame is required. The neutrino track is also required to have a polar angle Θ_{miss} within $0.3 < \Theta_{\text{miss}} < 2.2$ in order not to select events where particles lost in the beam pipe are mistaken as neutrinos. To further improve the neutrino quality, $m_{\text{miss}}^2 / (2 \cdot E_{\text{miss}}) < 2.5 \text{ GeV}$ is required. As the neutrino is massless this quantity should have a smaller values for signal events than for background events where heavier particles were lost. Fig. 5.3 shows the resulting distribution of $m_{\text{miss}}^2 / (2 \cdot E_{\text{miss}})$, the so-called ‘‘analysis selection’’ discussed in chapter 5.2 is applied. In the region dominated by the $b \rightarrow c\ell\nu$ background, the data event yield is slightly lower than the one expected from the MC simulation. At this relatively early analysis step, the fraction of the $b \rightarrow c\ell\nu$ background in the sample is high, and therefore the uncertainties due to it can account for the discrepancies. In addition, the scale factor $f_{b \rightarrow c\ell\nu}$ used to scale the $b \rightarrow c\ell\nu$ background is slightly too big at this point as it is estimated after the final selection.

²To calculate the energy of a track, particle identification is used to assign the corresponding mass to the track, e.g. the kaon mass, if the track was identified as a kaon.

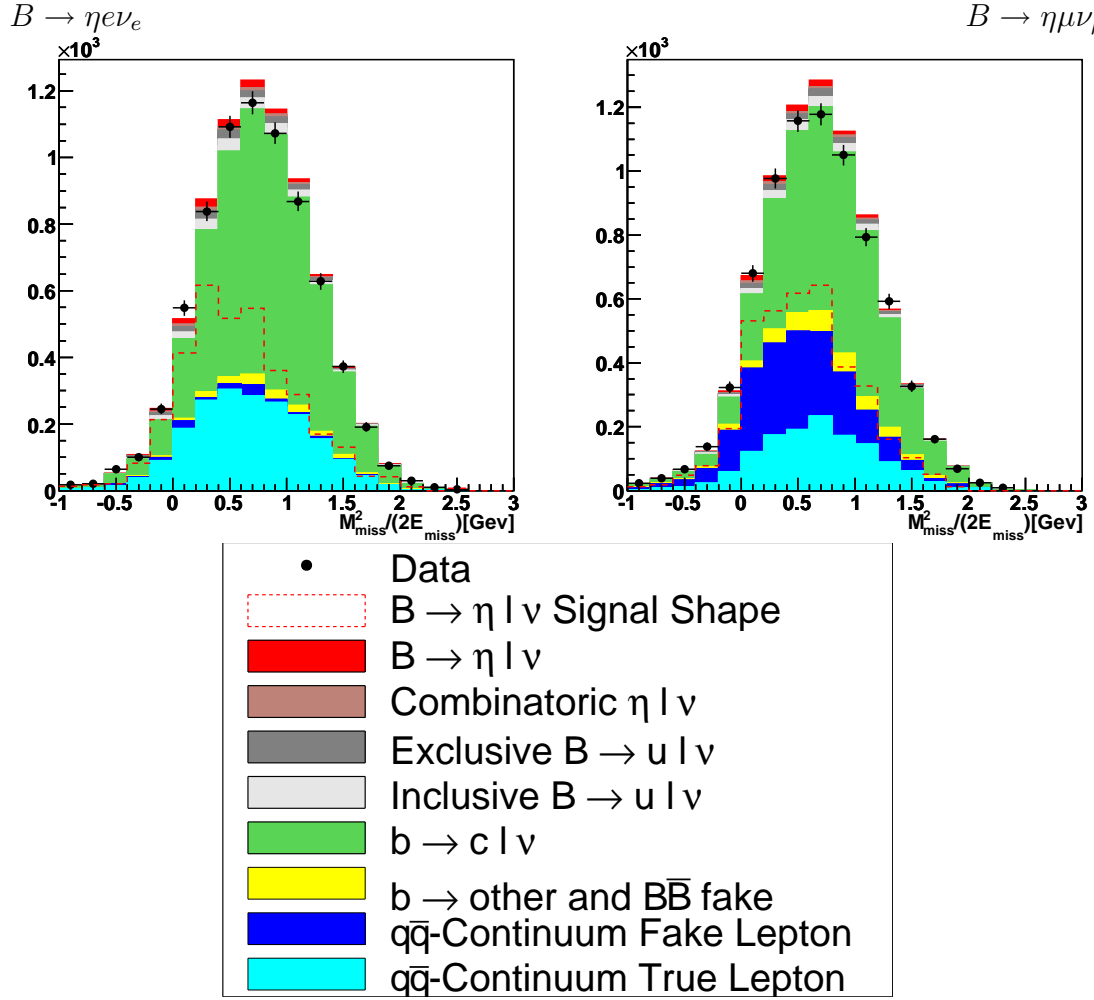


Figure 5.3: Distribution of the energy over the mass $m_{\text{miss}}^2/(2E_{\text{miss}})$ of the neutrino candidate with the analysis selection (5.2) applied. In the region dominated by the $b \rightarrow c l \nu$ background, the data event yield is slightly lower than the one expected from the MC simulation, which can be accounted for by the uncertainties of the $b \rightarrow c l \nu$ background.

5.1.5 Event Shape Variables

Jet-like continuum events can be distinguished from spherical $B\bar{B}$ events using so-called event shape variables:

- $\cos(\Theta_{Thrust})$, where Θ_{Thrust} is the angle between the thrust axes³ of the Y-candidate and of the whole event. It is only used in the final selection and shown in Fig. 5.4. In the distribution the $q\bar{q}$ -continuum events clearly separate from the $B\bar{B}$ events.
- The second normalized Fox-Wolfram moment⁴ R_2 , required to be $R_2 < 0.5$
- The second Legendre moment⁵ L_2 , required to be $L_2 < 2.0$

The criteria chosen for R_2 and L_2 reject events from $q\bar{q}$ -continuum dominated regions and are adopted from the $B^0 \rightarrow \pi^- \ell^+ \nu_\ell$ analysis [2].

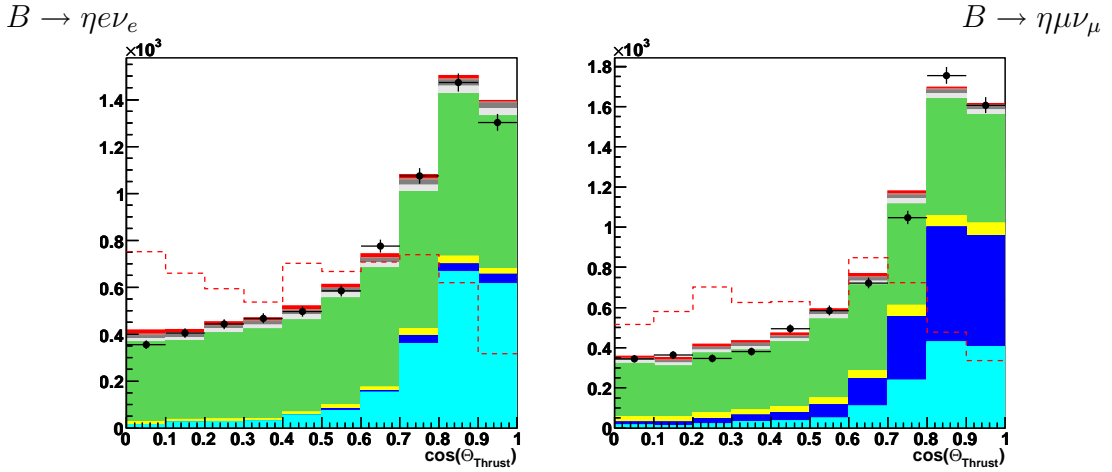


Figure 5.4: Distribution of the cosine of the angle between the thrust axes of the Y-system and of the whole event $\cos(\Theta_{Thrust})$ with the analysis selection (5.2) applied. The $q\bar{q}$ -continuum events clearly separate from the $B\bar{B}$ events. For the legend see Fig. 5.3.

³The thrust axis of N particles is given as the normal vector \vec{n} that maximizes the thrust, given as:

$$thrust = \left| \frac{\sum_i^N \vec{n} \cdot \vec{p}_i}{\sum_i^N |\vec{p}_i|} \right|$$

⁴ $R_2 = \sum_{ij} |p_i| |p_j| P_2(\cos\Theta_{ij})$, where the summation is over all final state particles, p_i and p_j are momenta of the particles i and j , Θ_{ij} is the angle between them and $P_2(x) = (1/2)(3x^2 - 1)$ is the second Legendre polynomial.

⁵ $L_2 = \sum_i |\vec{p}_i^*| \cos^2(\Theta_i^*)$, where the sum is over all the tracks in the event not used to form the Y-candidate. \vec{p}_i^* and Θ_i^* are the tracks momenta and angles with respect to the Y-systems thrust axis.

5.1.6 m_{ES} and ΔE

The kinematic consistency of the candidate with a B -meson decay is further checked by using the energy substituted mass m_{ES} and the difference between the expected and the reconstructed energy of the B -meson, ΔE . Defined in the laboratory frame, ΔE is

$$\Delta E = \frac{P_B \cdot P_{\text{beams}} - s/2}{\sqrt{s}}$$

where s is the center-of-mass energy of the colliding e^\pm beam particles and P_B and P_{beams} ⁶ are the four-momenta of the B -meson and the colliding beam particles. The energy substituted mass m_{ES} is the mass of the B -meson under the assumption that the B -meson's energy is half the beam energy (equivalent to $\Delta E = 0$):

$$m_{\text{ES}} = \sqrt{(s/2 + \vec{p}_B \cdot \vec{p}_{\text{beams}})^2 / E_{\text{beams}}^2 - \vec{p}_B^2}$$

To restrict the selected events to the region expected for B -decays, the following

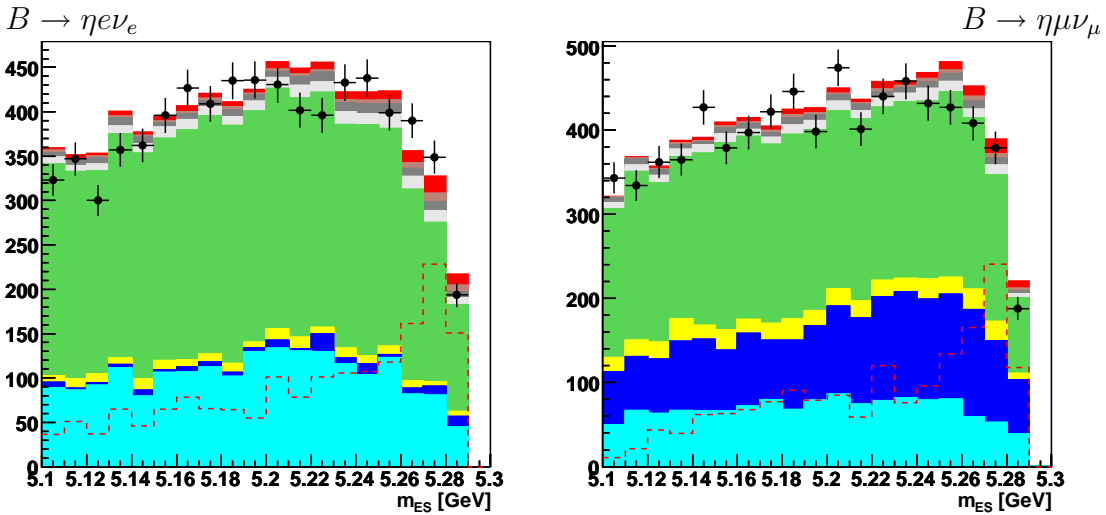


Figure 5.5: Distribution of the energy substituted mass m_{ES} with the analysis selection (5.2) applied. As expected for B -decays, the signal tends to have a value of m_{ES} around the B -meson mass (5279 MeV/ c^2). For the legend see Fig. 5.3.

is required: $5.095 \text{ GeV} < m_{\text{ES}} < 5.295 \text{ GeV}$ and $-0.95 \text{ GeV} < \Delta E < 0.95 \text{ GeV}$. The distribution of m_{ES} is shown in Fig. 5.5. As expected for B -decays, the signal tends to have higher values of m_{ES} than the backgrounds.

In chapter 6, the MC samples are fit to data to extract the signal branching fraction, using a two-dimensional fit of m_{ES} and the $\eta \rightarrow \pi^+ \pi^- \pi^0$ invariant mass.

⁶This quantity is not zero, as the system is boosted in direction of the electron beam.

5.2 Analysis Selection

After the preselection criteria just discussed, additional selection criteria are applied before neural-networks are used. They are described here and called “analysis selection” in the following.

A standard criterion is the selection of Y-candidates with a $\chi^2/d.o.f.$ vertex fit probability (see chapter 5.1.3) bigger than 0.01. This reduces the combinatoric signal background by about 50% and the $b \rightarrow c\ell\nu$ and continuum backgrounds by about 60% each, while more than 80% of the signal is kept.

As already mentioned, some distributions show discrepancies between the event yield in data and the MC simulation solely in purely background dominated regions. Namely the energy difference of the B -meson ΔE and the momenta of the η ’s pion daughters in the laboratory system. Fig. 5.6 shows the energy

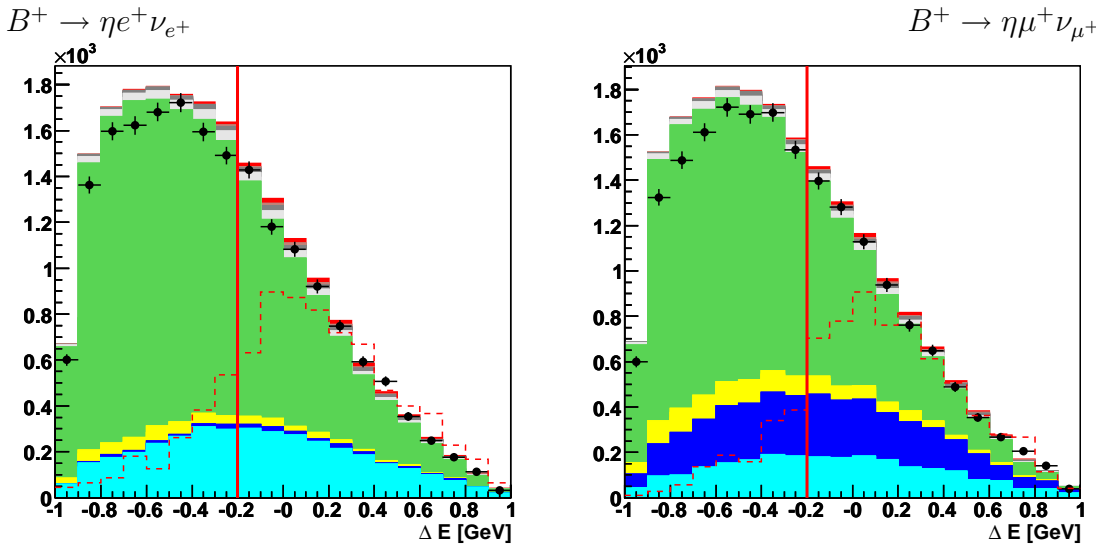


Figure 5.6: *Distribution of the energy difference of the B -meson ΔE with all the analysis selection criteria but the one on ΔE applied. Note that the dashed red line is the signal shape at an arbitrary scale, while the signal events (colored red) are scaled to the measured branching fraction. Only events on the right of the red lines pass the ΔE selection criterion. For the legend see Fig. 5.3.*

difference of the B -meson ΔE with all the other selection criteria discussed in this section applied. For small values the distribution is dominated by the $b \rightarrow c\ell\nu$ background⁷ and the event yield is systematically overestimated by the MC simulation. The effect is not understood, but the events in this purely background dominated region can be rejected, as the signal acceptance is not influenced by that. Therefore only events satisfying $\Delta E > -0.2$ GeV are selected.

⁷Note that the dashed red line is the signal shape at an arbitrary scale!

The same effect is observed in the momentum distributions of the η 's pion daughters (see Fig. 5.7). Charged pions with momenta $p_{\text{lab}}^{\pi^\pm} > 200 \text{ MeV}/c$ and neutral pions with momenta $p_{\text{lab}}^{\pi^0} > 400 \text{ MeV}/c$ are selected⁸. In addition, neutral pions that are made of photons with energies below 100 MeV are rejected, since the reconstruction is unreliable at smaller energies.

Tab. 5.4 and Tab. 5.5 (page 62 et seq.) show the event numbers as well as the relative and cumulative efficiencies of all selection criteria. In total, the selection significantly suppresses the main backgrounds, $b \rightarrow c\ell\nu$ by about 98% and $q\bar{q}$ -continuum by about 83%, while 38% of the signal events are kept.

⁸The specific values are adopted from the $B^0 \rightarrow \rho^- \ell^+ \nu_\ell$ analysis [2].

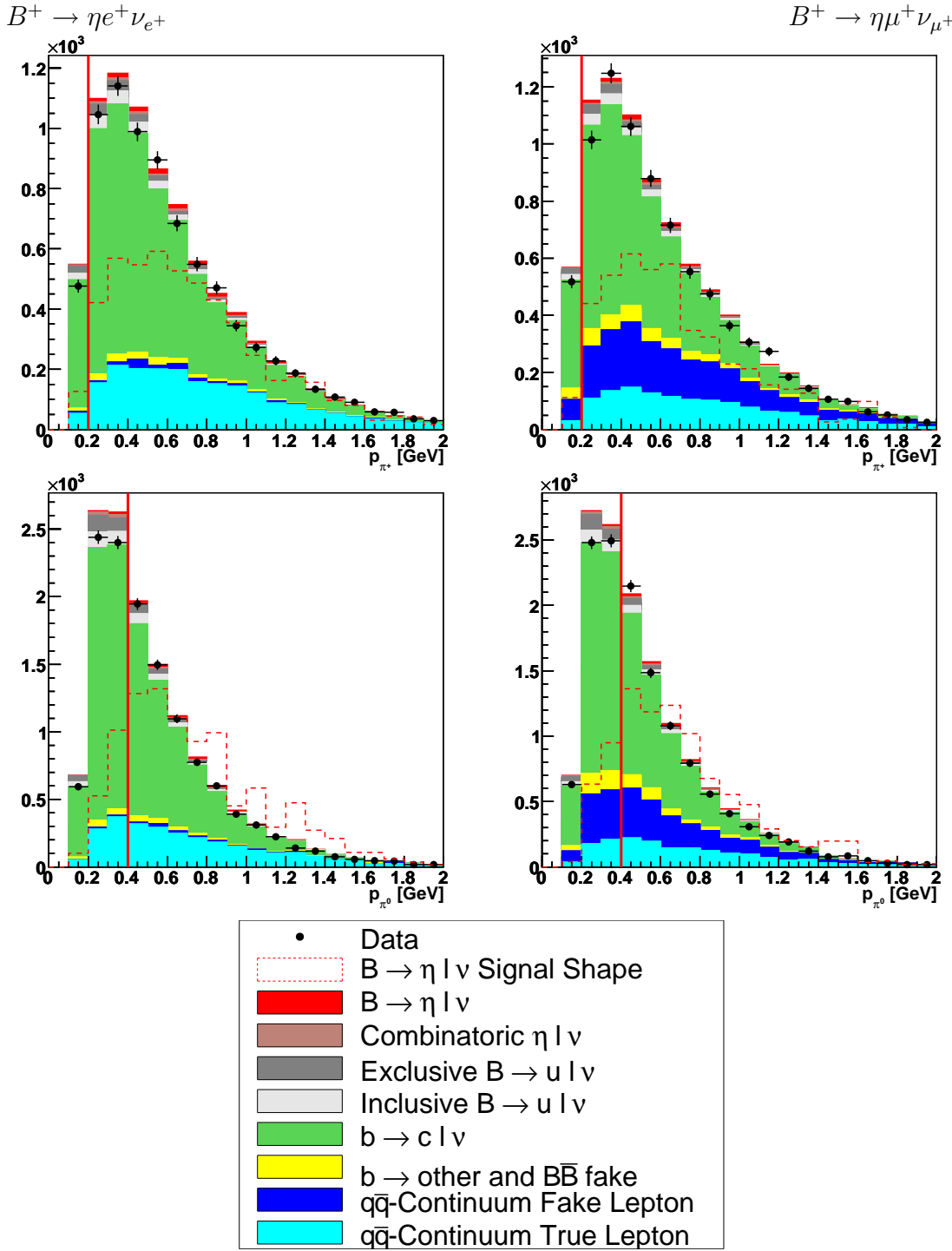


Figure 5.7: Momentum distributions of the η daughters. Namely charged (top) and neutral (bottom) pions, with all the analysis selection criteria but the one in question applied. For small values the distributions are dominated by the $b \rightarrow c l \nu$ background and the event yield is systematically overestimated by the MC simulation. Events in these purely background dominated regions can be rejected, as the signal acceptance is not influenced by that, therefore only events on the right of the red lines pass the corresponding selection criterion.

5.3 Multivariate Analysis

In multivariate analyses (MVA), a multi-dimensional space formed by a number of input variables is mapped onto a one dimensional space of a single output variable, called discriminator. The discriminator variable is then used to distinguish signal from background. The main advantage of a MVA is that, in contrast to an analysis with one-dimensional criteria, multi-dimensional correlations are taken into account.

This analysis uses neural-networks (NN) for the final signal selection. Their principles and how they are used are described in the following.

5.3.1 Neural-Networks

In this analysis the ROOT [24] based toolkit TMVA [25] is used. It conveniently provides a variety of multivariate algorithms and tools to analyse their performance. For the NNs the ROOT implementation⁹ is used.

Figure 5.8 shows the basic structure of a NN used in this analysis¹⁰. All the NNs used consist of n input neurons (one for each input variable), a first “hidden layer” with $n + 1$ neurons, a second hidden layer with n neurons and finally one output neuron. In the following, layers are labeled with l and the neurons in each layer are labeled with j . Each neuron presents an activation-function that, depending on the input value x_j , yields a certain output value $y_j(x_j)$. Different activation-functions can be used, the simplest one being a linear one $y_j(x_j) = x_j$, which in this work is used for the input neurons. The neurons in the hidden layers use a more sophisticated activation-function, the sigmoid function

$$y_j(x_j) = \frac{1}{1 + e^{-x_j}}.$$

This function has an output value between zero and one. Each neuron is connected with all neurons of the previous layer. The connections are called synapses and represent weights $w_{l,j}$. The input of a neuron x_j in the l^{th} layer is the sum of the output $y_1^{(l-1)} \dots y_n^{(l-1)}$ of all the previous layers’ m neurons, each weighted by $w_{1j}^{(l)} \dots w_{mj}^{(l)}$:

$$x_j = \sum_{i=1}^m y_i^{(l-1)} w_{ij}^{(l)}$$

The weighting factors of the synapses are estimated by a training process. The NN is trained with input variables from N signal and background MC events. For each event, the response y_{out} of the output neuron can be calculated and is

⁹Called “TMlpANN”

¹⁰This configuration is the default one applied in the TMVA package. Due to the limited amount of time, no other NN structures have been studied.

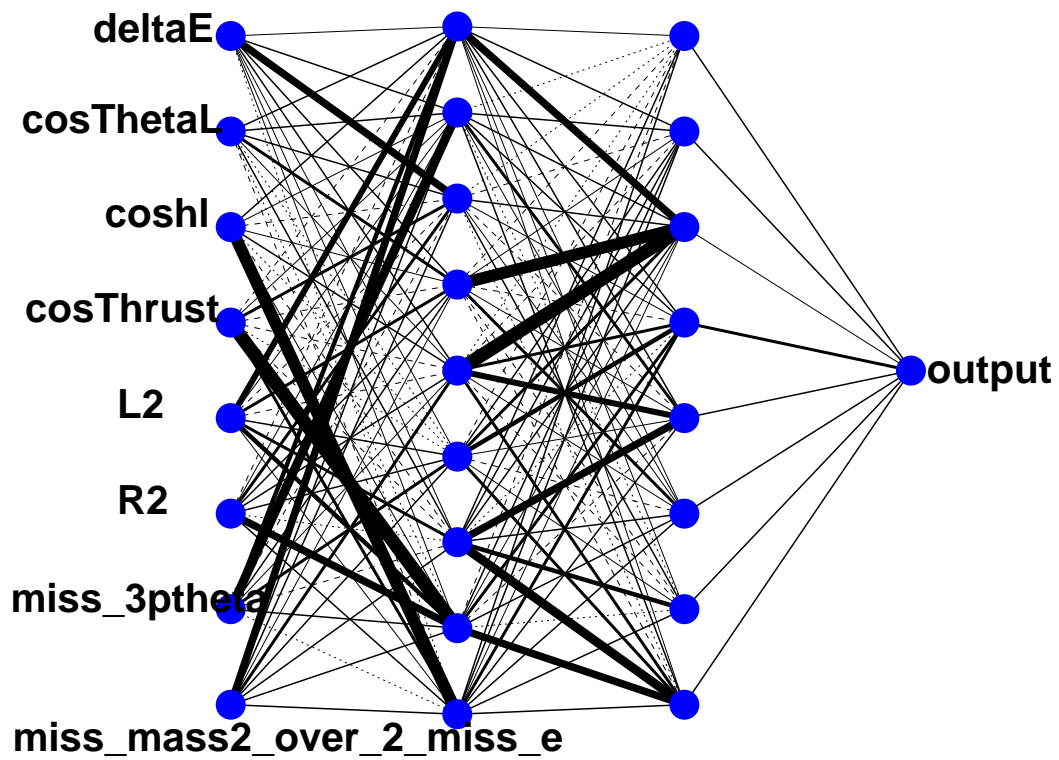


Figure 5.8: *Neural-network structure: Eight input neurons, one hidden layer with nine neurons, one hidden layer with eight neurons and one output neuron. The thickness of the lines (synapses) indicates the relative weight of the neuron.*

compared to the desired one $y_{\text{out}}^{\text{true}}$, which is one for signal and zero for background. To measure the agreement, an error function E is defined:

$$E(x_1, \dots, x_n, \mathbf{w}) = \sum_{a=1}^N \frac{1}{2} (y_{\text{out}} - y_{\text{out},a}^{\text{true}})^2,$$

where \mathbf{w} is the ensemble of adjustable weights and a denotes the a^{th} event of the sample. The set of weights that minimizes the error function is found using the method of steepest descent. Starting from a random set of weights \mathbf{w}^ρ , the weights are updated by moving a small distance in \mathbf{w} -space in the direction of the error functions derivative $-\nabla_{\mathbf{w}}E$, where E decreases most rapidly,

$$\mathbf{w}^{\rho+1} = \mathbf{w}^\rho - \eta \nabla_{\mathbf{w}}E$$

where the positive number η is the learning rate. The process is repeated over several cycles. This training method is called “back propagation of errors” [25].

After the NNs are trained, their performance is validated on a test sample that is different from the training sample.

In the following, the input distributions for the NNs used in this thesis as well as the training and testing processes are described.

5.3.2 Neural-Network Configurations

As the two main backgrounds have very different shapes in many distributions considered for this analysis, two different NN are applied to discriminate the signal against them.

First, a NN against the $q\bar{q}$ -continuum background ($q\bar{q}$ -net) is used. Then another one is applied against the $b \rightarrow c\ell\nu$ background ($c\ell\nu$ -net).

The following input variables are used for both, the $q\bar{q}$ -net and the $c\ell\nu$ -net.

Neural-Network Input Variables

Most variables used as input for the neural-networks were already mentioned in section 5.1.2, but all of them are listed here to give a complete overview. For completeness all the NN input distributions – also the ones not shown here – can be found in appendix B, with each, the analysis selection, the $q\bar{q}$ -net and the $c\ell\nu$ -net applied.

- $m_{\text{miss}}^2/(2E_{\text{miss}})$ using the mass and energy of what would be the neutrino in case of perfect reconstruction, see Fig. 5.3.
- $\Theta_{p_{\text{miss}}}$ the angle between the neutrino momentum and the beam axis, see Fig. 5.9.
- The second Fox-Wolfram moment R_2 , described in section 5.1.5.

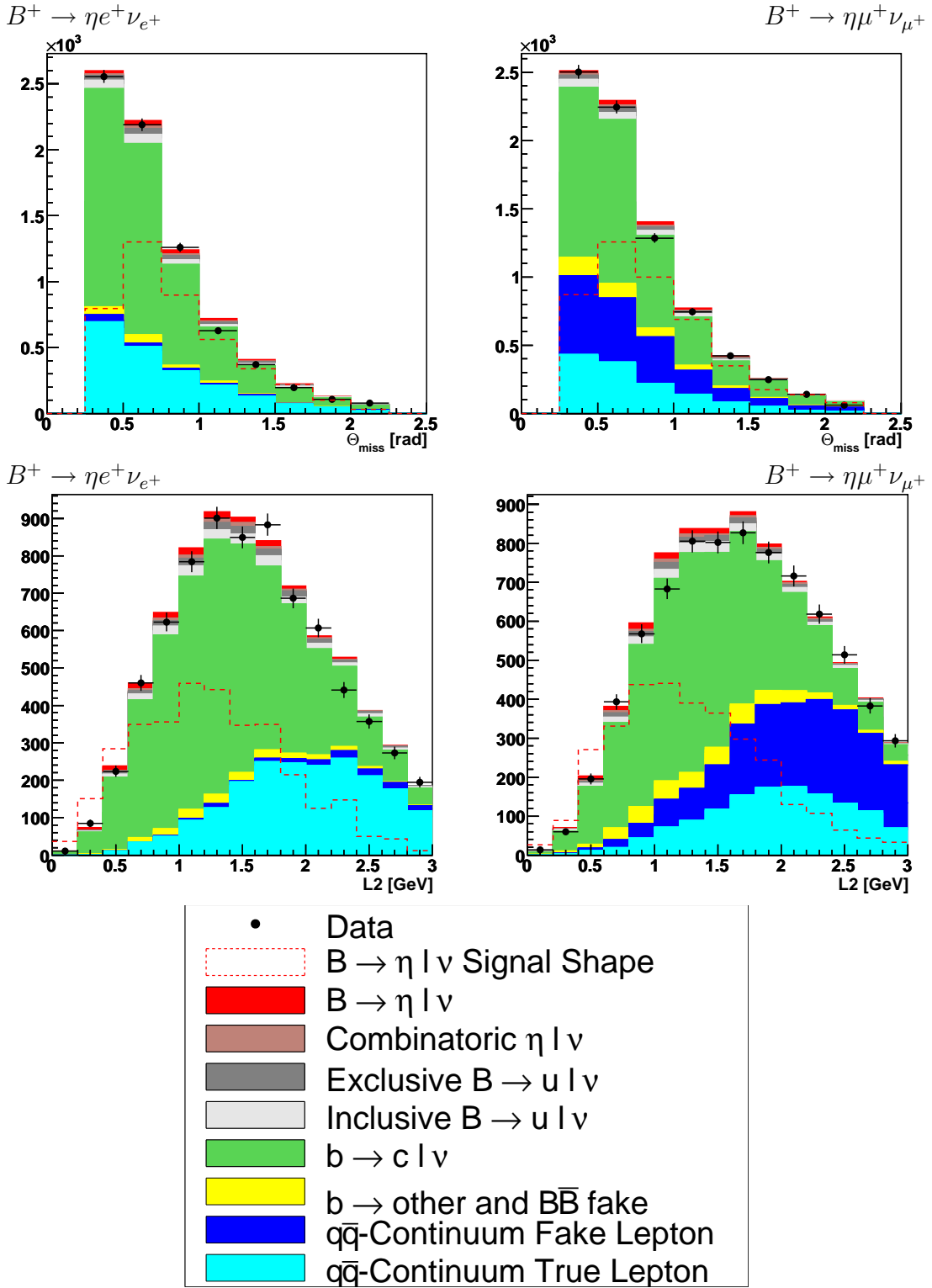


Figure 5.9: Distribution of $\Theta_{p_{\text{miss}}}$, the angle between the neutrino momentum and the beam axis, and L_2 , the second Legendre moment with the analysis selection (5.2) applied. The data is well described by the simulation. While in $\Theta_{p_{\text{miss}}}$ only slight differences between the signal and background shapes are visible, in L_2 the $q\bar{q}$ -continuum events clearly separate from the $B\bar{B}$ events.

- The second Legendre moment L_2 , described in section 5.1.5, see Fig. 5.9.
- $\cos(\Theta_{Thrust})$, the cosine of the angle between the thrust axes of the Y-system and of the whole event, described in 5.1.5, see Fig. 5.4.
- $\cos(\Theta_{BY})$, described in 5.1.3, see Fig. 5.2.
- $\cos(\Theta_{hl})$, the cosine of the angle between the η and the lepton taken in the laboratory system, see Fig. 5.10.
- The lepton momentum p_l^* in the $\Upsilon(4S)$ system, see Fig. 5.10.
- The momentum $p_{\pi^0}^*$ of the π^0 coming from the η decay measured in the $\Upsilon(4S)$ system, see Fig. 5.7.
- $\cos(\Theta_L)$, the cosine of the angle between the lepton and the W-boson in $\Upsilon(4S)$ system, see Fig. 5.11.
- ΔE , described in 5.1.6, see Fig. 5.6.
- The η momentum p_η^* in the $\Upsilon(4S)$ system, see Fig. 5.11.

With only the analysis selection applied some of these distributions still show small discrepancies between the data and the MC simulation in background dominated regions. However, after the final selection with the NNs has been applied the data agree well with the simulation (see appendix B), e.g. the lepton momentum distribution after the analysis selection (Fig. 5.10) shows a discrepancy in the $B^+ \rightarrow \eta\mu^+\nu_{\mu^+}$ event sample where it is dominated by $q\bar{q}$ -continuum events with fake leptons. After those events are suppressed with the $q\bar{q}$ -net it agrees well. Furthermore, the effect is accounted for as a systematic uncertainty by studying the influence of different choices of NN input variables (chapter 7).

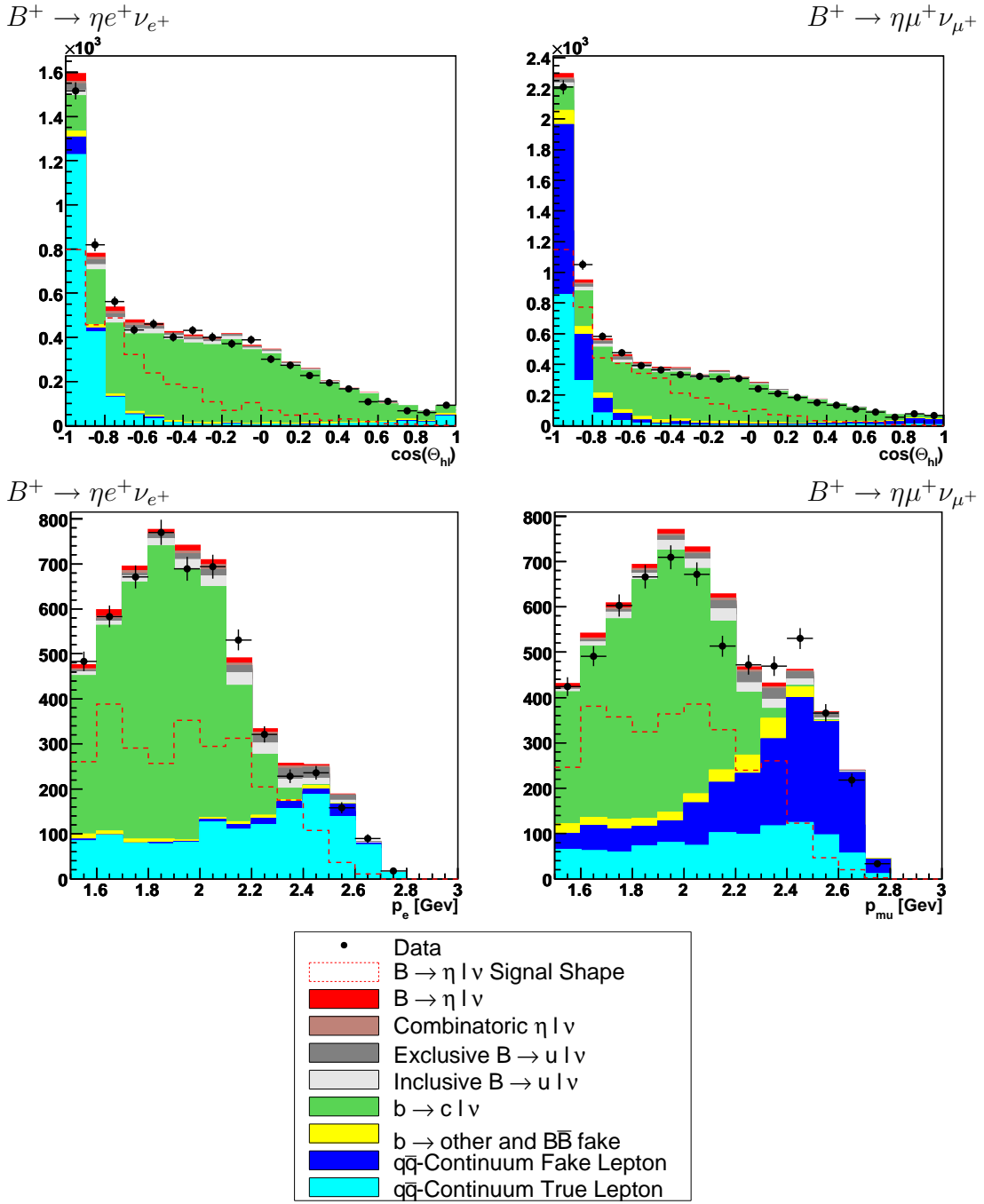


Figure 5.10: Distribution of $\cos(\Theta_{hl})$, the cosine of the angle between the η and the lepton taken in the laboratory system and the lepton momentum p_l^* in the $\Upsilon(4S)$ system with the analysis selection (5.2) applied. The $\cos(\Theta_{hl})$ in data is described well by the simulation and the signal events separate from both, the $q\bar{q}$ -continuum and the $b \rightarrow c l \nu$ -background events. The lepton momentum distribution shows a small discrepancy between the data and the simulation in the $B^+ \rightarrow \eta \mu^+ \nu_{\mu^+}$ event sample where it is dominated by continuum events with fake leptons. However, after those are suppressed with the $q\bar{q}$ -net (see appendix B) it agrees well. It distinguishes the signal from both main backgrounds.

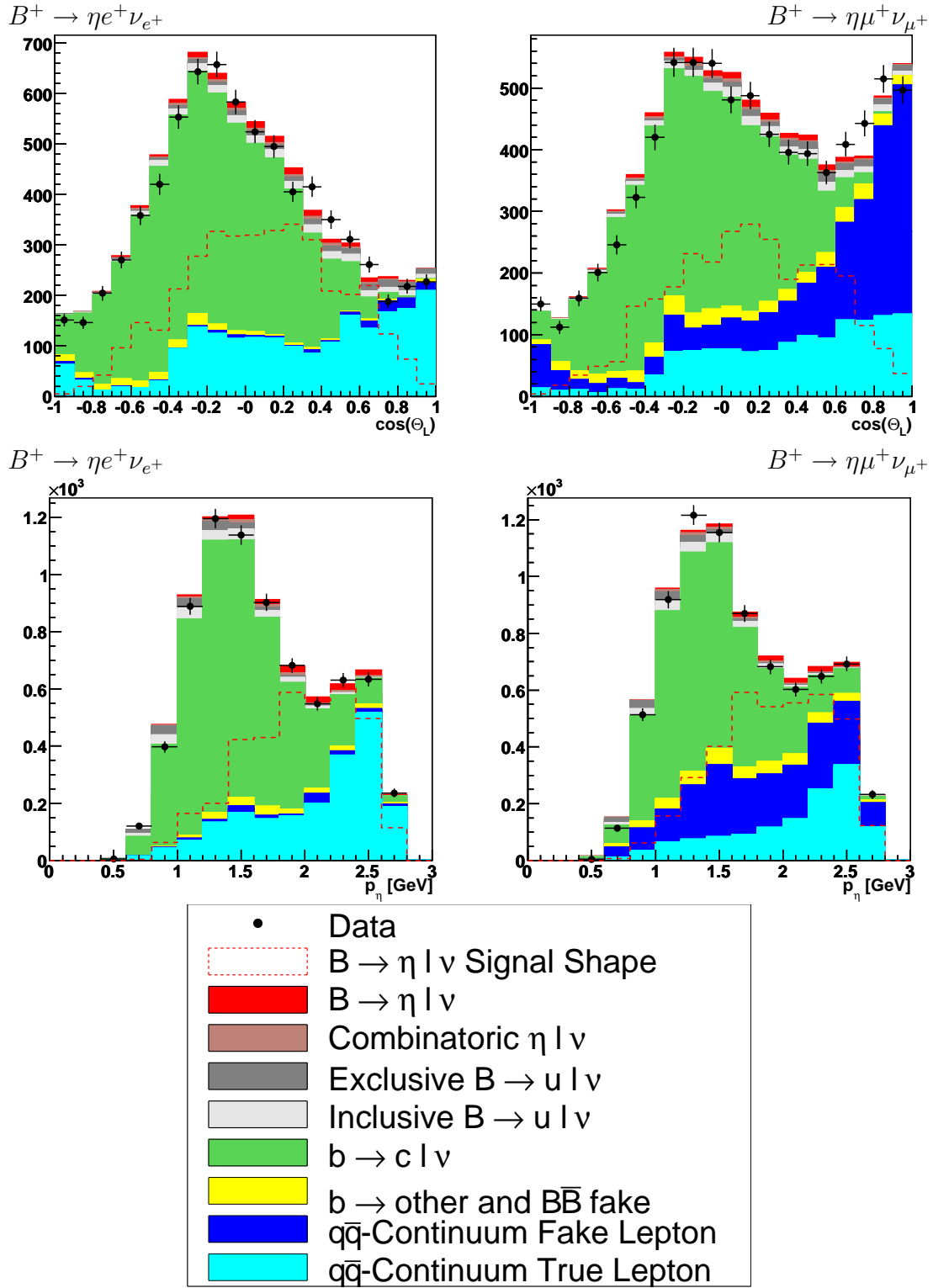


Figure 5.11: Distribution of $\cos(\Theta_L)$, the cosine of the angle between the lepton and the W -boson in $\Upsilon(4S)$ system and the momentum p_η^* of the η in the $\Upsilon(4S)$ system with the analysis selection (5.2) applied. The data is well described by the simulation. While in the $\cos(\Theta_L)$ distribution the signal events mainly separate from the $q\bar{q}$ -continuum events, in the p_η^* distribution they separate from the $b \rightarrow c l \nu$ -background events.

5.3.3 Neural-Network Training and Testing

One half of the signal MC and background MC sample¹¹ are used to train the NNs, while the other one is used to test it. Due to the already limited statistics, for further analyses both the training and test samples are used.

For the training only events in the signal region $m_{ES} > 5.2 \text{ GeV}$ and $533 \text{ MeV}/c^2 < m_{\pi^+\pi^-\pi^0} < 557 \text{ MeV}/c^2$ are used to enhance the discrimination power of the NNs and to keep the computing time within a reasonable range well below one hour.

After the training the test MC sample is used to determine the NN performance. The signal and background efficiencies and the background rejection

$$\begin{aligned}
 E_{\text{signal}}^{\text{MC}} &= \frac{\text{Signal events selected by the NN}}{\text{Total number of signal events}} \\
 E_{\text{bkg}}^{\text{MC}} &= \frac{\text{Background events selected by the NN}}{\text{Total number of background events}} \\
 R_{\text{bkg}}^{\text{MC}} &= 1 - E_{\text{bkg}}^{\text{MC}} = 1 - \frac{\text{Background events selected by the NN}}{\text{Total number of background events}}
 \end{aligned}$$

are determined as a function of the output variables. These distributions vary whenever a the NN is retrained¹², so the discriminator variable itself is not a good variable to use for any selection. However, it is connected to the signal efficiencies, as can be seen in Fig. 5.12. For each value of the discriminator variable the signal efficiency and the background rejection can be calculated from the distribution of the signal shown in the figure. Fig. 5.13 shows the background rejection versus the signal efficiency for the $q\bar{q}$ -net. In chapter 5.3.4 cut-values for the discriminator variables of each NN are estimated, that optimize the signal efficiency and the background rejection.

Each NN is trained 20 times on the same samples. To make sure the NNs are not overtrained - meaning that the goodness of the selection is overrated - the signal efficiencies in the training and test samples are compared at different background efficiencies. The numbers are shown in Tab. 5.3. The signal efficiencies on the test sample compare well with the ones on the training sample. Hence the NNs are not overtrained.

5.3.4 Neural-Network Optimization

After the NNs have been trained on the signal MC sample and the specific MC background samples they are used on the whole sample to estimate their total efficiencies. Fig. 5.15 shows the discriminator output of both the $q\bar{q}$ -net and the $cl\nu$ -net estimated on the whole MC sample and data. The $q\bar{q}$ -net successfully discriminates the signal against the $q\bar{q}$ -continuum background. In case of the

¹¹The $q\bar{q}$ -continuum for the $q\bar{q}$ -net and the $b \rightarrow cl\nu$ background for the $cl\nu$ -net.

¹²When a new NN is trained the initial weights are randomly generated.

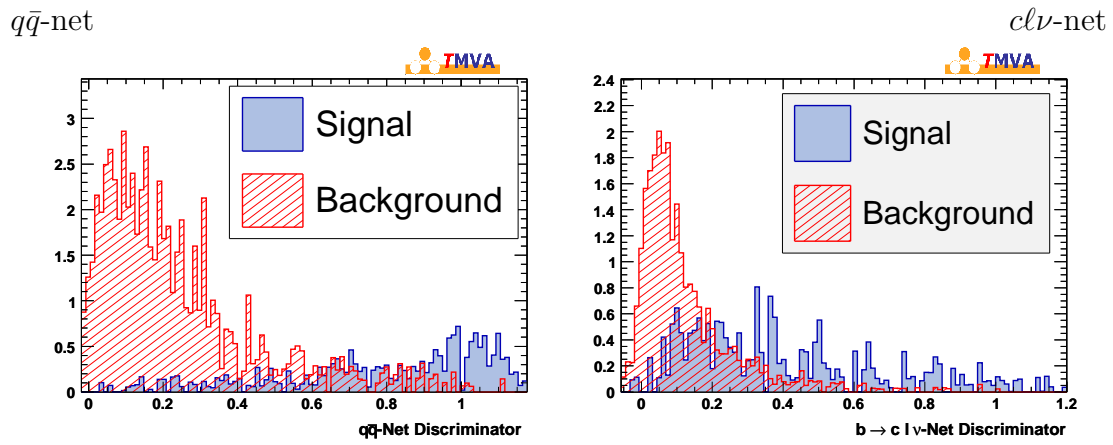


Figure 5.12: Distribution of the discriminator output variables of the $q\bar{q}$ -net (left) and the $cl\nu$ -net (right).

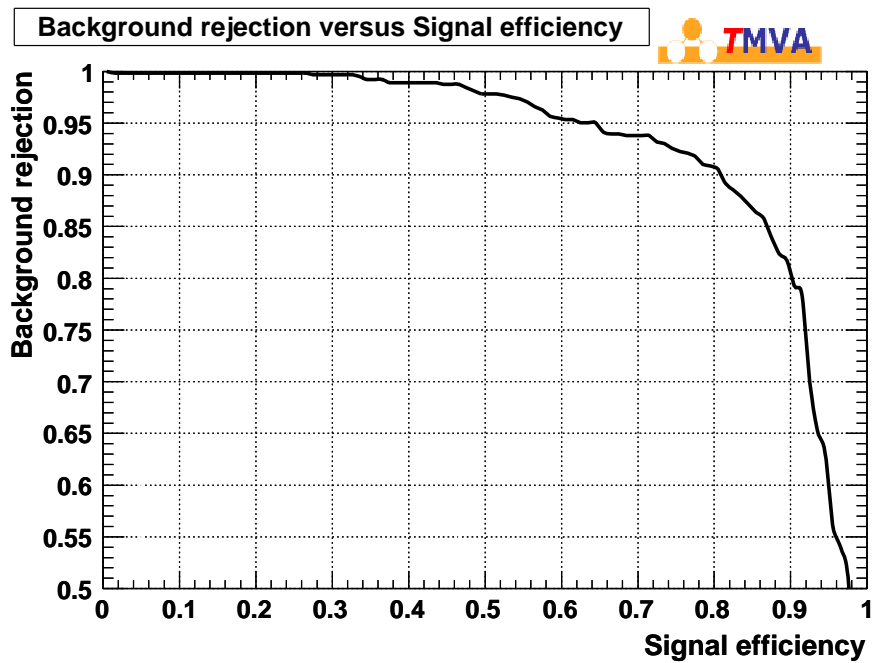


Figure 5.13: Distribution of the background rejection versus the signal efficiency for the $q\bar{q}$ -net.

Net	BE = 10%		BE = 30%	
	SE Test	SE Train	SE Test	SE Train
$q\bar{q}$ -net	78.4%	77.8%	92.6%	91.3%
$cl\nu$ -net	58.6%	56.7%	82.3%	82.9%

Table 5.3: Signal efficiencies (SE) on both the test and the training sample at different background efficiencies (BE) for the $q\bar{q}$ -net and the $cl\nu$ -net.

$cl\nu$ -net the discrimination of the signal against the $b \rightarrow cl\nu$ -background is not as good as in the $q\bar{q}$ -net case, which is probably due to the relatively low statistics.

In order to minimize the statistical error in the later fit, the cuts on the two discriminator variables must be optimized somehow. This is done by optimizing the ratio

$$S/\sqrt{S+B},$$

where S is the number of signal MC events and B the number of MC background events in the signal region ($533 \text{ MeV}/c^2 < m_\eta < 557 \text{ MeV}/c^2$ and $m_{ES} > 5.2 \text{ GeV}$).

Technically, the optimization is done by scanning both the signal efficiency of the $cl\nu$ -net and the $q\bar{q}$ -net from 20% to 100% in steps of 5% and computing the ratio $S/\sqrt{S+B}$ at each step. The result of the scan in the $cl\nu$ -net signal efficiency - $q\bar{q}$ -net efficiency plane is shown in Figure 5.14. The maximum is found

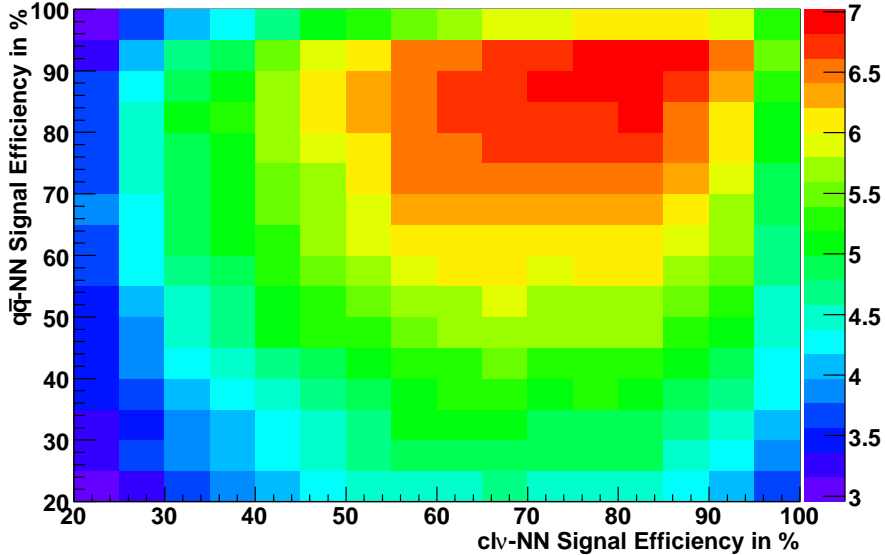


Figure 5.14: $S/\sqrt{S+B}$ in dependence of the signal efficiencies of the $q\bar{q}$ -net and the $cl\nu$ -net used for the optimization of the discriminant thresholds. A signal efficiency of 95% for the $q\bar{q}$ -net and of 85% for the $cl\nu$ -net are later used.

to be $S/\sqrt{S+B} = 7.02$ for signal efficiencies of 95% for the $q\bar{q}$ -net and 85% for the $cl\nu$ -net. This translates into a cut-value of 0.23 for the $q\bar{q}$ -net discriminator variable and of 0.13 for the $cl\nu$ -net discriminator variable.

Fig. 5.16 and Fig. 5.17 (60 et seq.) show the distributions of the variables later used to extract the branching fraction: the energy substituted mass m_{ES} and the reconstructed η mass $m_{\pi^+\pi^-\pi^0}$, before the NNs, after the application of the $q\bar{q}$ -net and after the additional use of the $cl\nu$ -net and illustrate the increase of the signal fraction with each selection step performed.

Tab. 5.4 and Tab. 5.5 (62 et seq.) show the event numbers and relative as well as cumulative efficiencies on the signal MC sample, the $q\bar{q}$ -continuum background MC, the $b \rightarrow cl\nu$ background MC, the total MC sample and on data. Note that the $b \rightarrow cl\nu$ background is not scaled by scale factor $f_{b \rightarrow cl\nu} = 0.889$ discussed in chapter 4.3.2 and estimated in chapter 6.

All selection criteria applied significantly reduce the main backgrounds, namely the $b \rightarrow cl\nu$ background by 99% and the $q\bar{q}$ -continuum background by 98%.

29% of the $B^+ \rightarrow \eta\ell^+\nu_\ell$ signal events are passing the selection, while 96% of the combinatoric $B^+ \rightarrow \eta\ell^+\nu_\ell$ background are rejected. Thus the ratio of the number of signal events to combinatoric signal events increases from $917/2746 = 33\%$ to $264/105 = 251\%$. Note that no difference between true and combinatoric signal is made when the branching fraction is extracted from data in the next chapter, as in data the two samples cannot be distinguished.

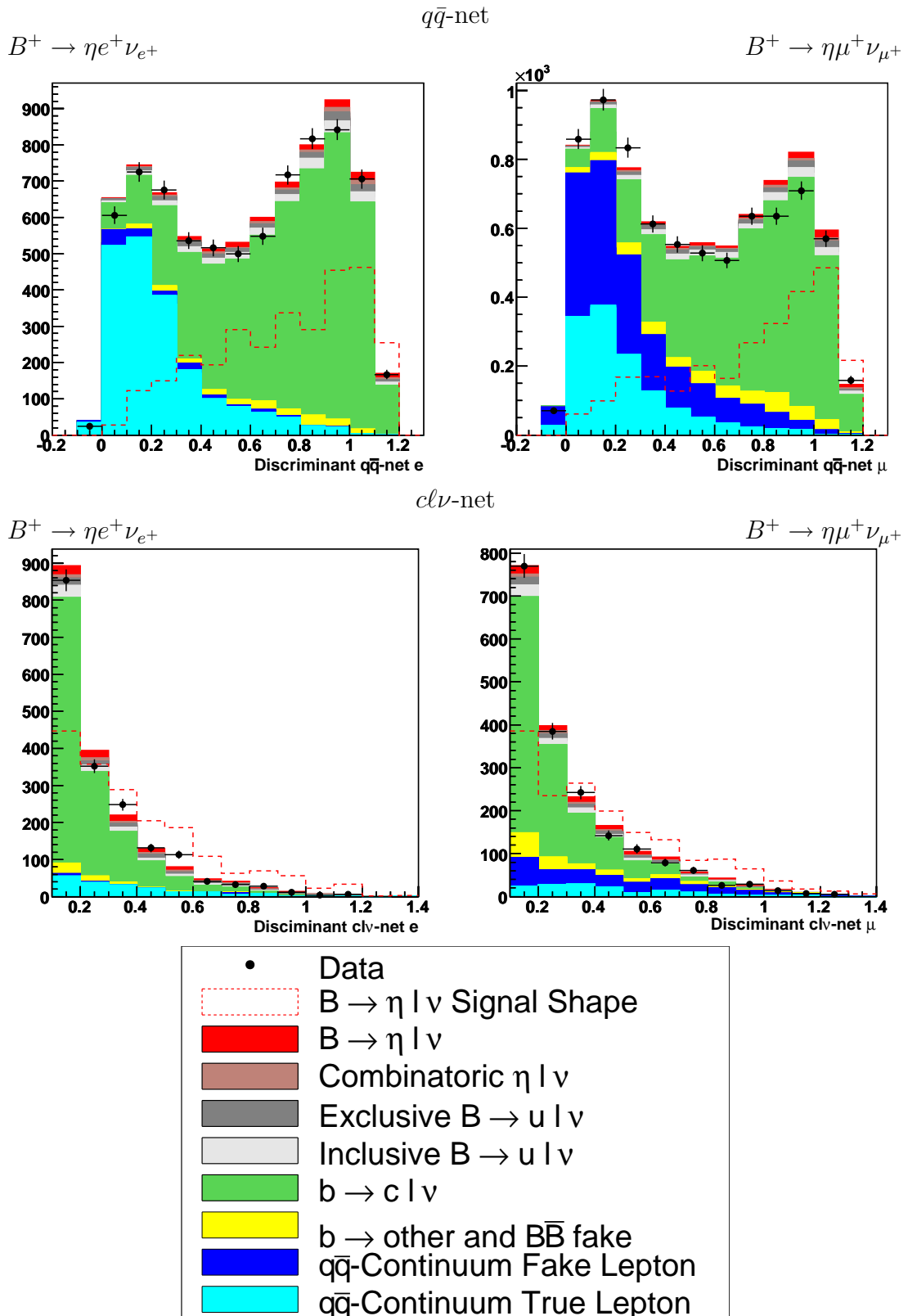


Figure 5.15: Distributions of the discriminator output variables for the $q\bar{q}$ -net and the $cl\nu$ -net. Events with a $q\bar{q}$ -net discriminator smaller than 0.23 and with a $cl\nu$ -net discriminator smaller than 0.13 are rejected.

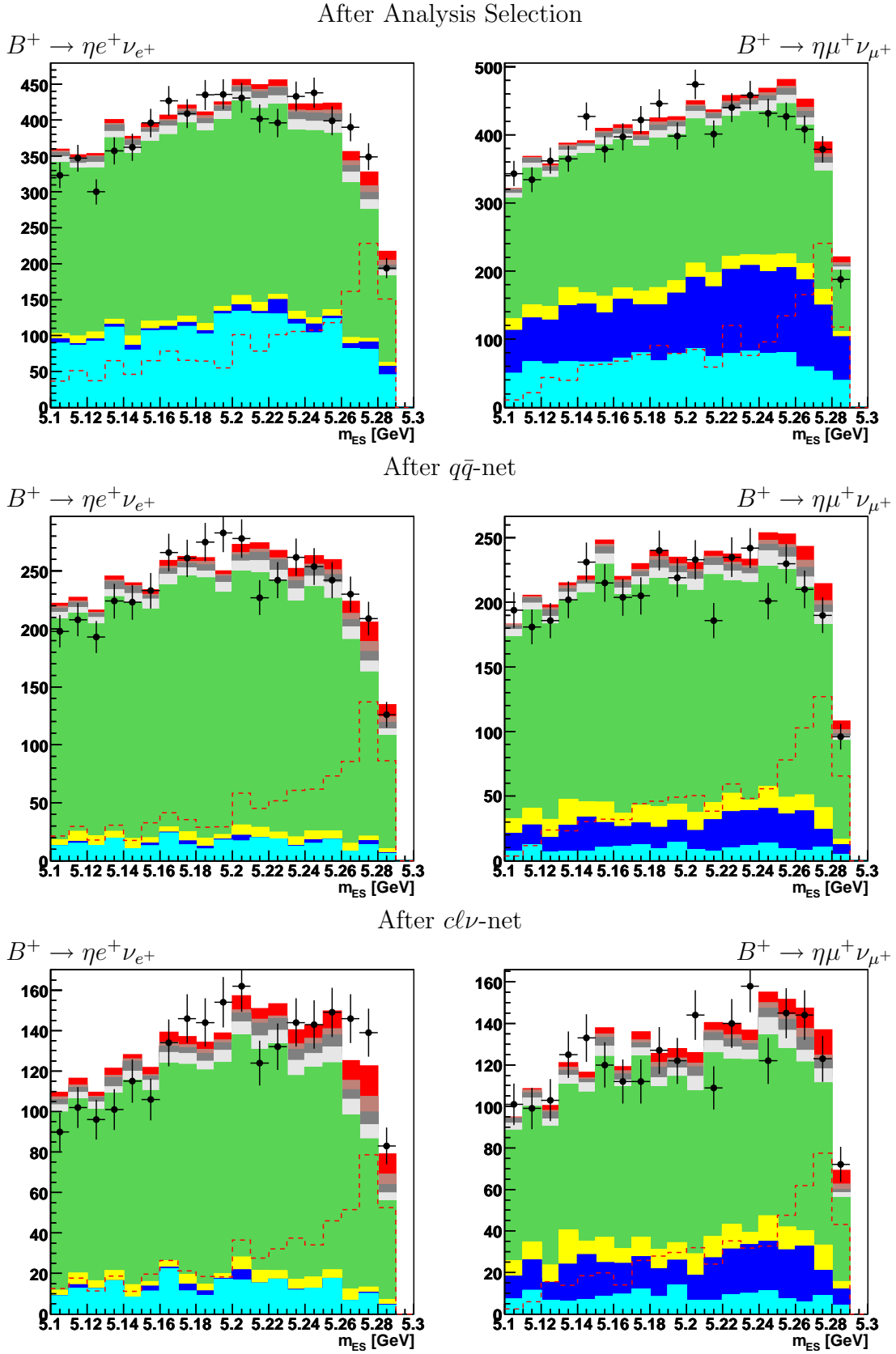


Figure 5.16: Distribution of m_{ES} at different selection steps. The increasing signal fraction and background suppression are visible. See Fig. 5.15 for the legend.

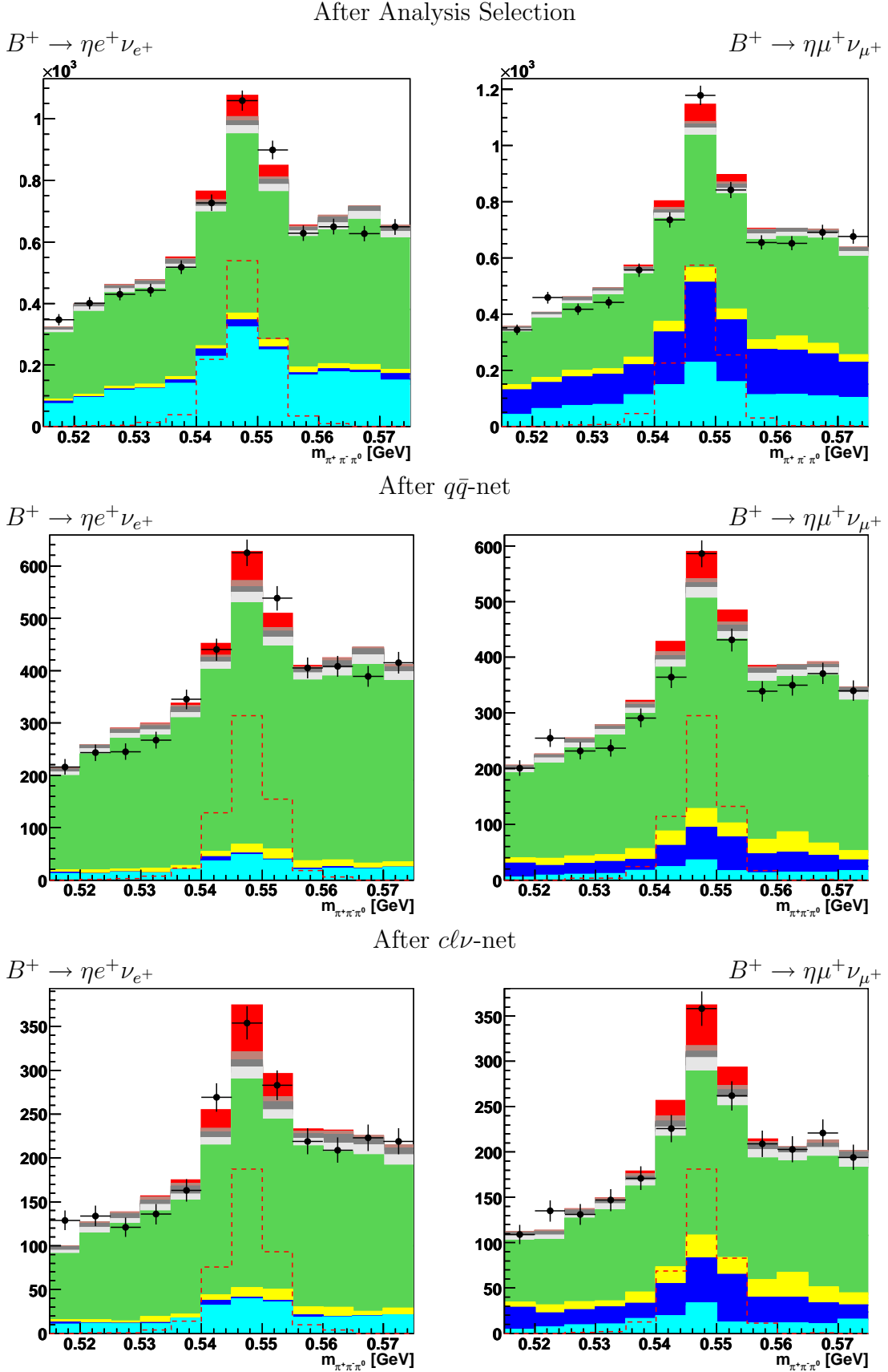


Figure 5.17: Distribution of the reconstructed η mass $m_{\pi^+\pi^-\pi^0}$ at different selection steps. The increasing signal fraction and background suppression are visible. See Fig. 5.15 for the legend.

Selection Flow - $B^+ \rightarrow \eta\ell\nu$				
Requirement	Before	After	Relative Efficiency	Cumulative Efficiency
Vertex	917	751	82%	82%
ΔE	751	610	81%	67%
π^+	610	586	96%	64%
π^-	586	567	97%	62%
π^0	567	422	74%	46%
E_γ	422	352	83%	38%
$q\bar{q}$ -net	352	328	93%	36%
$cl\nu$ -net	328	264	81%	29%
Selection Flow - Combinatoric $B^+ \rightarrow \eta\ell\nu$				
Requirement	Before	After	Relative Efficiency	Cumulative Efficiency
Vertex	2746	1341	49%	49%
ΔE	1341	909	68%	33%
π^+	909	793	87%	29%
π^-	793	717	90%	26%
π^0	717	276	38%	10%
E_γ	276	161	58%	6%
$q\bar{q}$ -net	161	150	93%	5%
$cl\nu$ -net	150	105	70%	4%
Selection Flow - $q\bar{q}$ -Continuum MC Sample				
Requirement	Before	After	Relative Efficiency	Cumulative Efficiency
Vertex	76542	31475	41%	41%
ΔE	31475	15121	48%	20%
π^+	15121	14017	93%	18%
π^-	14017	13193	94%	17%
π^0	13193	7353	56%	10%
E_γ	7353	5251	71%	7%
$q\bar{q}$ -net	5251	2129	41%	3%
$cl\nu$ -net	2129	1619	76%	2%

Table 5.4: *Event numbers and relative as well as cumulative efficiencies for the signal MC sample, the combinatoric signal MC sample and the $q\bar{q}$ -Continuum MC sample. Relative efficiencies are with respect to the number of events after applying the last criterion, cumulative efficiencies are with respect to the initial number of events.*

Selection Flow - $b \rightarrow c\ell\nu$ MC Sample				
Requirement	Before	After	Relative Efficiency	Cumulative Efficiency
Vertex	447539	177026	40%	40%
ΔE	177026	53646	30%	12%
π^+	53646	47325	88%	11%
π^-	47325	42578	90%	10%
π^0	42578	14374	34%	3%
E_γ	14374	9663	67%	2%
$q\bar{q}$ -net	9663	9116	94%	2%
$c\ell\nu$ -net	9116	2486	27%	1%
Selection Flow - Sum of all MC Samples				
Requirement	Before	After	Relative Efficiency	Cumulative Efficiency
Vertex	581447	233704	40%	40%
ΔE	233704	79677	34%	14%
π^+	79677	70380	88%	12%
π^-	70380	63543	90%	11%
π^0	63543	24293	38%	4%
E_γ	24293	16686	69%	3%
$q\bar{q}$ -net	16686	12842	77%	2%
$c\ell\nu$ -net	12842	5041	39%	1%
Selection Flow - Data				
Requirement	Before	After	Relative Efficiency	Cumulative Efficiency
Vertex	504191	193552	38%	38%
ΔE	193552	68874	36%	14%
π^+	68874	61611	89%	12%
π^-	61611	56078	91%	11%
π^0	56078	21978	39%	4%
E_γ	21978	15025	68%	3%
$q\bar{q}$ -net	15025	11303	75%	2%
$c\ell\nu$ -net	11303	4666	41%	1%

Table 5.5: Event numbers and relative as well as cumulative efficiencies for the $b \rightarrow c\ell\nu$ MC sample, the sum of all MC samples and on real data. Relative efficiencies are with respect to the number of events after applying the last criterion, cumulative efficiencies are with respect to the initial number of events. Note that the $b \rightarrow c\ell\nu$ MC sample is not scaled with the scale factor $f_{b \rightarrow c\ell\nu} = 0.889$ discussed in chapter 4.3.2 and therefore the sum of all MC samples yields higher numbers than the data.

Chapter 6

Extraction of the Branching Fraction

To extract the branching fraction the two-dimensional distribution of the energy substituted mass m_{ES} and the reconstructed η mass $m_{\pi^+\pi^-\pi^0}$ is used. In this distribution the signal and background MC samples are fit to the data and the fraction of $B^+ \rightarrow \eta\ell^+\nu_\ell$ is extracted.

In contrast to many other analyses, in this analysis the MC statistics are limited compared to the data statistics. Although in $b \rightarrow c\ell\nu$ 1100 million MC events were used, this is only about three times the data statistics. Therefore the statistical uncertainty in the MC samples cannot be neglected. This is why a special kind of binned maximum likelihood fit, described in the next section, is used.

6.1 The Barlow-Beeston Fit Algorithm

To extract the branching fraction a special kind of binned maximum likelihood fit, that does not only account for the statistical fluctuations of the data sample but also for the fluctuations in the MC samples is used. It is described in more detail in [26].

Assuming that the data are somehow binned in i bins, let d_i stand for the number of data and f_i for the number of predicted MC events in the i^{th} bin. As there are actually m different MC samples contributing, the f_i are actually a sum over all the m MC samples in the i^{th} bin, $f_i = \sum_{j=1}^m p_j a_{ji}$. The factors p_j are the fractions of each source (that need to be estimated) and the a_{ji} are the numbers of generated events from the j^{th} MC sample in the i^{th} bin.

In a normal binned maximum likelihood fit the likelihood function \mathcal{L} is the probability to find the measured number of data d_i for a given parameter f_i . For

Poisson distributed events the likelihood function is

$$\mathcal{L} = \prod_i \frac{f_i^{d_i}}{d_i!} e^{-f_i}.$$

The problem is usually solved by maximizing $\ln(\mathcal{L})$, instead of \mathcal{L} , by taking its derivative and setting it to zero:

$$\begin{aligned} \ln(\mathcal{L}) &= \sum_{i=1}^n d_i \ln(f_i) - f_i + \text{const.} \\ \frac{\partial \ln(\mathcal{L})}{\partial p_j} &= 0 \quad \forall j \end{aligned}$$

But when fitting MC distributions to data, the MC event numbers a_{ji} in each bin are not the expected but the generated ones. The expectation A_{ij} is unknown. From each A_{ij} a corresponding a_{ij} is generated by a Poisson distribution. So the prediction for the number of data events in bin i actually is $f_i = \sum_{j=1}^m p_j A_{ji}$. Therefore, the total likelihood that needs to be maximized is the combined probability of the observed d_i and the observed a_{ij} and hence

$$\begin{aligned} \ln(\mathcal{L}) &= \sum_{i=1}^n d_i \ln(f_i) - f_i \\ &\quad + \sum_{i,j} a_{ji} \ln(A_{ji}) - A_{ji} \\ &\quad + \text{const.} \end{aligned}$$

needs to be maximized. Taking the derivative and setting it to zero yields:

$$\begin{aligned} \frac{\partial \ln(\mathcal{L})}{\partial p_j} = 0 &\Rightarrow \sum_{i=1}^n \frac{d_i A_{ji}}{f_i} - A_{ji} = 0 \quad \forall j \\ \frac{\partial \ln(\mathcal{L})}{\partial A_{ji}} = 0 &\Rightarrow \frac{d_i p_j}{f_i} - p_j + \frac{a_{ji}}{A_{ji}} - 1 = 0 \quad \forall i, j \end{aligned}$$

The second equation can be rewritten to

$$A_{ij} = \frac{a_{ji}}{1 + p_j \left(1 - \frac{d_i}{f_i}\right)}$$

which allows, with a given set of starting values for the fractions p_j , to calculate the expected values A_{ij} . Those are used in the first equation that is then maximized using MINUIT [27]. Note that at least one of the p_j needs to float in the fit. All others might be set to a fixed value if needed.

6.2 Fit Strategy

As the energy substituted mass m_{ES} and the reconstructed invariant η mass $m_{\pi^+\pi^-\pi^0}$ are correlated in the signal and most background sources and therefore the likelihood function cannot be factorized, the data is binned in a two-dimensional histogram of these variables. Both the electron and the muon sample are used together, as the statistics would be too low to perform separate fits. Only events that are in the fit region $5.09 \text{ GeV} < m_{\text{ES}} < 5.29 \text{ GeV}$ and $515 \text{ MeV} < m_{\pi^+\pi^-\pi^0} < 575 \text{ MeV}$ are considered. An irregular binning is used to fully exploit the specific signal and background shapes. In the signal region defined as $5.23 \text{ GeV} < m_{\text{ES}} < 5.29 \text{ GeV}$ and $533 \text{ MeV} < m_{\pi^+\pi^-\pi^0} < 557 \text{ MeV}$ smaller bins are used than in the sidebands. With this binning the histogram consists of 77 bins. The shape of the binning is shown in Fig. 6.1. Fig. 6.2 shows the event density¹ of the two-dimensional $m_{\text{ES}}-m_{\pi^+\pi^-\pi^0}$ distributions for the signal, the summed MC backgrounds and data in this binning.

To perform the fit method described in 6.1 the bins of the two-dimensional histogram are mapped on a one-dimensional histogram that also consists of 77 bins. Although this is a mere technicality, this one-dimensional histogram will later be used to illustrate the fit performance.

The scale factors p_{signal} of the signal and $p_{b \rightarrow c\ell\nu}$ of the $b \rightarrow c\ell\nu$ background are the free parameters in the fit, the p_j of all other MC sources are fixed to their MC prediction with the nominal branching fractions of Tab. 4.2. Only the $q\bar{q}$ -continuum background is scaled by the factors estimated in chapter 4.3.1. After performing the fit, the fractions p_{signal} and $p_{b \rightarrow c\ell\nu}$ before and after the fit are compared and corresponding scale factors

$$f_{\text{signal}} = \frac{p_{\text{signal}}^{\text{after fit}}}{p_{\text{signal}}^{\text{before fit}}}$$

$$f_{b \rightarrow c\ell\nu} = \frac{p_{b \rightarrow c\ell\nu}^{\text{after fit}}}{p_{b \rightarrow c\ell\nu}^{\text{before fit}}}$$

are computed.

In principle, the measured branching fraction $\mathcal{B}(B^+ \rightarrow \eta \ell^+ \nu_\ell)_{\text{measured}}$ of the signal decay is just the product of the branching fraction $\mathcal{B}(B^+ \rightarrow \eta \ell^+ \nu_\ell)_{\text{MC}}$ used in the MC simulation and the obtained scale factor f_{signal} . But as the signal is reconstructed in the $\eta \rightarrow \pi^+\pi^-\pi^0$ channel, this is dependent of the branching fraction $\mathcal{B}(\eta \rightarrow \pi^+\pi^-\pi^0)_{\text{MC}} = 22.6\%$ in the MC simulation. As the actual value is $\mathcal{B}(\eta \rightarrow \pi^+\pi^-\pi^0)_{\text{PDG}} = (22.7 \pm 0.4)\%$ [4], this needs to be corrected for. In the

¹In order to make the regions of different bin sizes comparable the entries in each bin are normalized to the size of the bin.

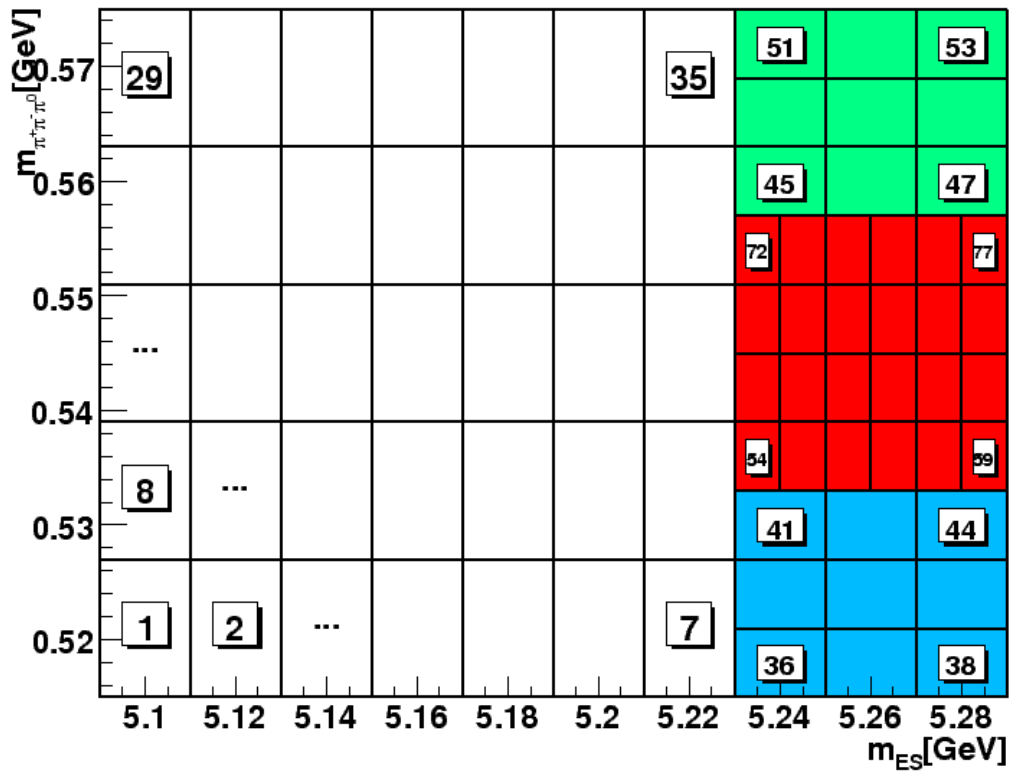


Figure 6.1: *Illustration of irregular binning used for the fit. Red indicates the signal region, green, blue and white indicate the sidebands. The numbers indicate on which bin of the one-dimensional histogram the bin is mapped.*

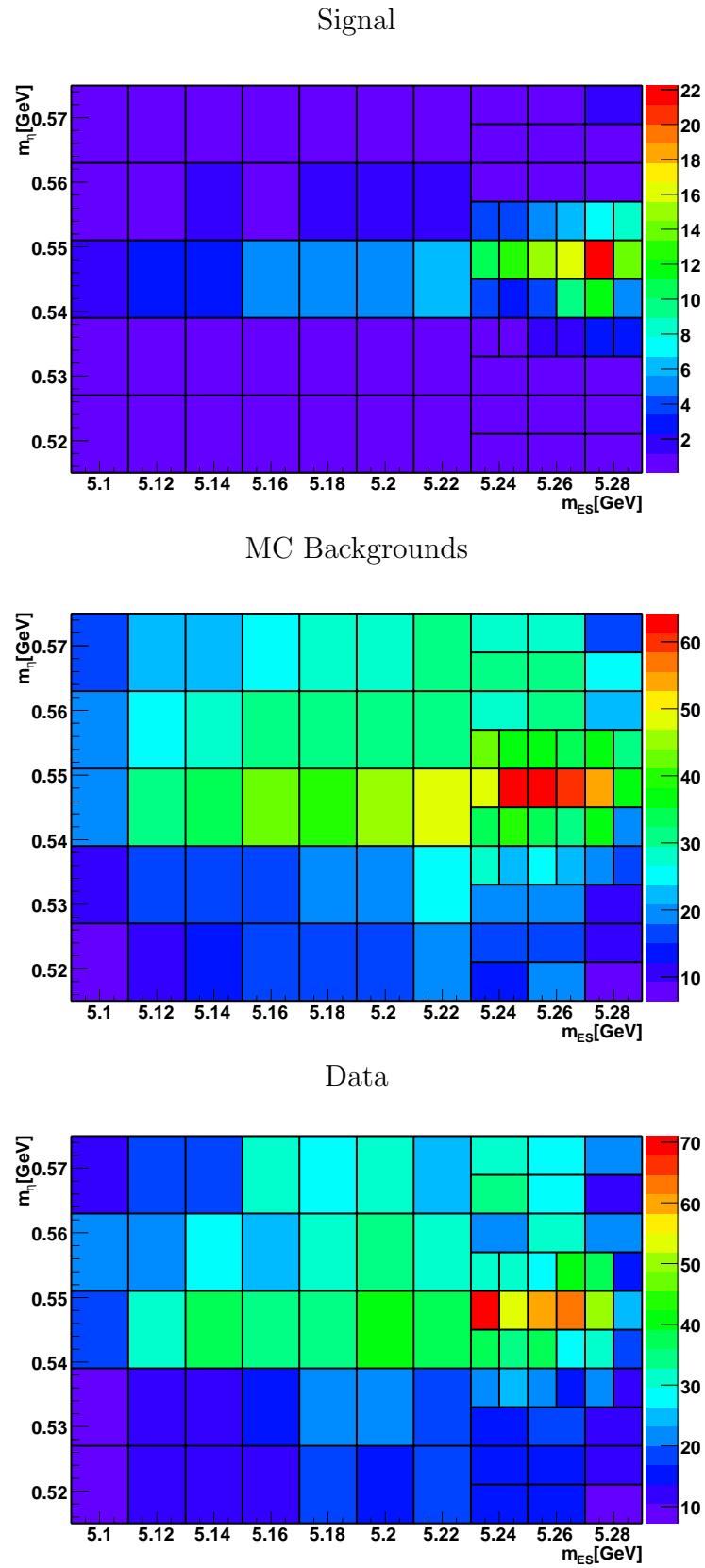


Figure 6.2: Two-dimensional distribution of m_{ES} vs. $m_{\pi^+\pi^-\pi^0}$ for the signal, the total MC sample and data. Note that event densities are shown, the unit of the color scale is event number per $10 \text{ MeV} \cdot 10 \text{ MeV}/c^2$.

MC simulation

$$\begin{aligned} \mathcal{B}(B^+ \rightarrow \eta (\rightarrow \pi^+ \pi^- \pi^0) \ell^+ \nu_\ell)_{\text{MC}} &= \mathcal{B}(B^+ \rightarrow \eta \ell^+ \nu_\ell)_{\text{MC}} \cdot \mathcal{B}(\eta \rightarrow \pi^+ \pi^- \pi^0)_{\text{MC}} \\ \rightarrow \mathcal{B}(B^+ \rightarrow \eta \ell^+ \nu_\ell)_{\text{MC}} &= \frac{\mathcal{B}(B^+ \rightarrow \eta (\rightarrow \pi^+ \pi^- \pi^0) \ell^+ \nu_\ell)_{\text{MC}}}{\mathcal{B}(\eta \rightarrow \pi^+ \pi^- \pi^0)_{\text{MC}}} \end{aligned}$$

is implemented. This has to be corrected by multiplying it with

$$\frac{\mathcal{B}(\eta \rightarrow \pi^+ \pi^- \pi^0)_{\text{MC}}}{\mathcal{B}(\eta \rightarrow \pi^+ \pi^- \pi^0)_{\text{PDG}}}.$$

Therefore the measured branching ratio is:

$$\begin{aligned} \mathcal{B}(B^+ \rightarrow \eta \ell^+ \nu) &= \mathcal{B}(B^+ \rightarrow \eta \ell^+ \nu)_{\text{MC}} \cdot f_{\text{signal}} \cdot \frac{\mathcal{B}(\eta \rightarrow \pi^+ \pi^- \pi^0)_{\text{MC}}}{\mathcal{B}(\eta \rightarrow \pi^+ \pi^- \pi^0)_{\text{PDG}}} \\ &= 8.4 \cdot 10^{-5} \cdot f_{\text{signal}} \cdot \frac{22.6}{22.7} \end{aligned}$$

6.3 Fit Validation

Before the fit is used on real data, its stability is tested by performing 10,000 “toy experiments”, where instead of the real data a fluctuated so-called “toy MC” sample is used.

For each toy experiment this toy MC sample is generated by adding the Poisson-fluctuated signal MC sample, the Poisson-fluctuated $b \rightarrow c\ell\nu$ and $q\bar{q}$ continuum MC samples and the Poisson-fluctuated sum of all the other background MC samples.

Then the MC sources, after being Poisson-fluctuated as well, are fitted to the toy MC. The whole process is then repeated 10,000 times.

In these toy-experiments the signal scale factor is expected to be one and that is indeed the case, as Fig. 6.3 shows. The so-called pull distribution is computed

$$\text{pull} = \frac{(\text{fitted value}) - (\text{true value})}{\text{error of the fitted value}}$$

and then fitted with a single Gaussian. Both are shown in Fig. 6.3. As expected for a stable and unbiased fit, the pull distribution has a mean of zero and a width of one.

6.4 Fit Result

After the stability of the fit has been validated, it is applied to real data. It yields the following scale factors for the signal and the $b \rightarrow c\ell\nu$ background:

$$\begin{aligned} f_{\text{signal}} &= (0.773 \pm 0.177) \\ f_{b \rightarrow c\ell\nu} &= (0.889 \pm 0.039) \end{aligned}$$

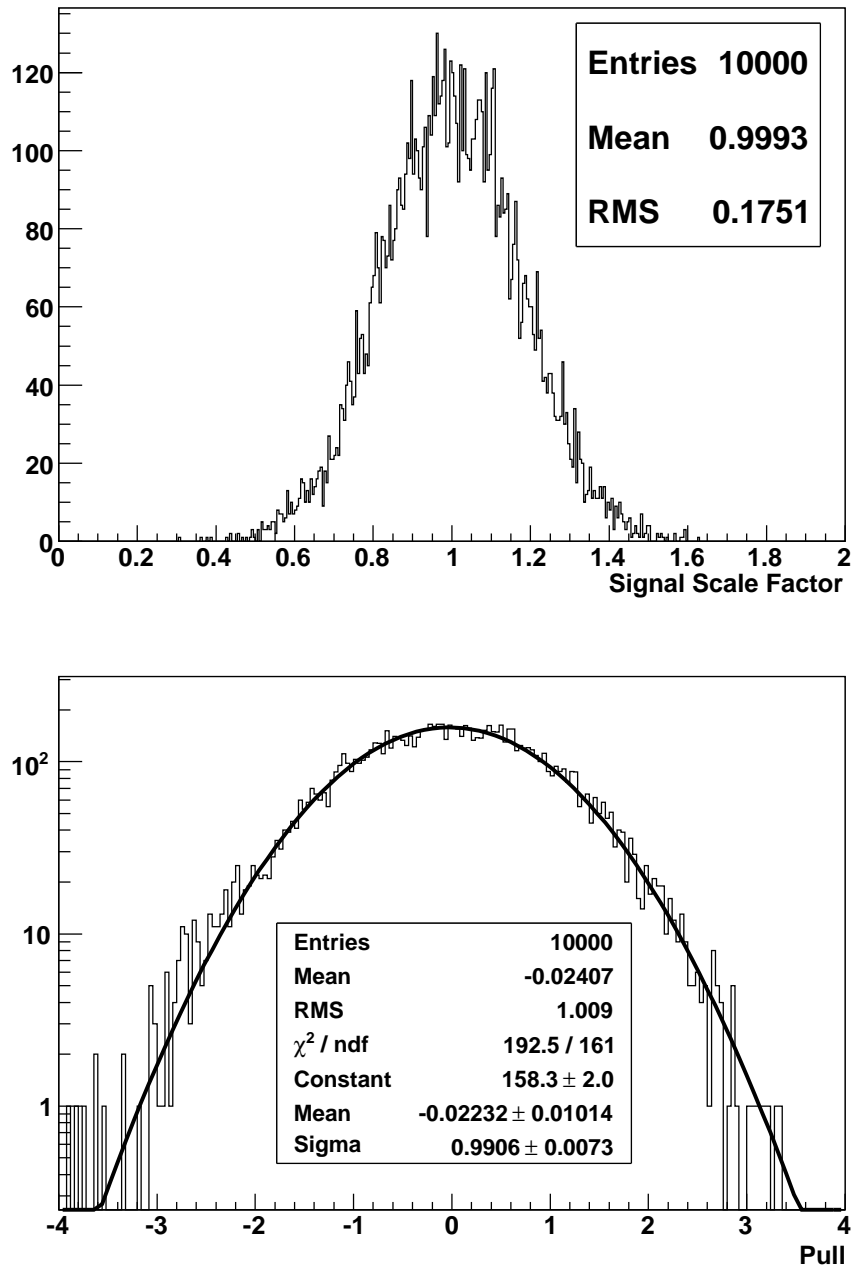


Figure 6.3: Distribution of the signal scale factor and the pull, obtained with 10,000 toy-experiment.

and has an acceptable $\chi^2/\text{d.o.f.}^2 = 109/77$.

The correlation matrix ρ of the fit-parameters f_{signal} and $f_{b \rightarrow c\ell\nu}$ is:

$$\rho = \begin{pmatrix} 1.00 & -0.57 \\ -0.57 & 1.00 \end{pmatrix}$$

Hence f_{signal} and $f_{b \rightarrow c\ell\nu}$ are correlated by about 57%. This correlation will be used in chapter 7 to take the systematic uncertainty in the $b \rightarrow c\ell\nu$ background into account.

Fig. 6.4 shows the fit result in the one-dimensional histogram and the reconstructed η mass $m_{\pi^+\pi^-\pi^0}$ before and after the fit, meaning with and without the f_{signal} and $f_{b \rightarrow c\ell\nu}$ scale factors applied.

The signal scale factor translates into a branching fraction of

$$\mathcal{B}(B^+ \rightarrow \eta\ell^+\nu_\ell) = (6.47 \pm 1.48) \cdot 10^{-5},$$

where the uncertainty is of pure statistic nature.

²degrees of freedom

Fit Result

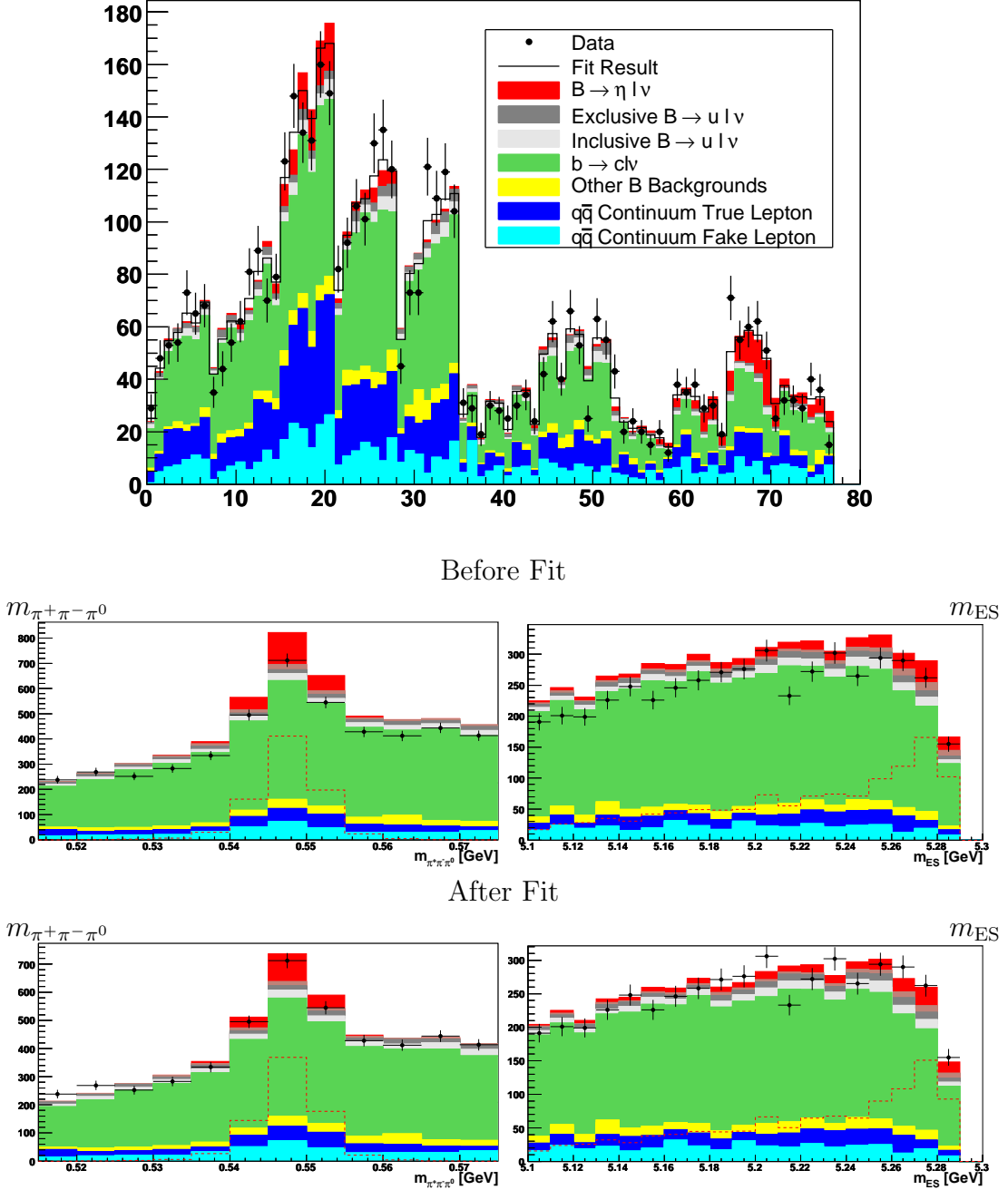


Figure 6.4: The fit result in the one-dimensional binning, the reconstructed η mass $m_{\pi^+\pi^-\pi^0}$ before fit (without the obtained scaling factors f_{signal} and $f_{b \rightarrow c l \nu}$ applied) and after the fit (with the obtained scaling factors $f_{\text{signal}} = 0.773$ and $f_{b \rightarrow c l \nu} = 0.889$ applied).

Chapter 7

Systematic Uncertainties

The uncertainties of the nominal branching ratio obtained in chapter 6 are of statistical nature only. However, there are other error sources that lead to systematic uncertainties. These are more complicated to evaluate than the statistical ones. The systematic uncertainties in this analysis are mainly due to detector effects, uncertainties in the physics modeling and the uncertainty in the NN configuration and training process.

To estimate the systematic uncertainty of the measured branching fraction, the nominal result is compared to the results obtained after systematic changes of the MC reconstruction that reflect the uncertainties in the simulation. For instance, the tracking efficiency is varied, then the MC reconstruction is repeated and the branching ratio is extracted again. The difference with respect to the nominal value is taken as the systematic uncertainty.

An overview of all systematic uncertainties considered is given in Tab. 7.1, here and in the following, all systematic uncertainties are given relative to the nominal branching fraction. To a good approximation the single errors are uncorrelated and therefore can be added in quadrature to estimate the total systematic error.

7.1 Detector Effects

Due to the neutrino reconstruction, the analysis does not only depend on the tracks and clusters used to reconstruct the η and the lepton, but also on all the remaining ones. Therefore, the uncertainties in the detection efficiencies of all particles contribute to the systematic uncertainty.

7.1.1 Track and Photon Reconstruction

All uncertainties in charged and neutral particle reconstruction efficiencies, in tracks and photons from beam background, fake tracks, failures in matching of neutral clusters to charged tracks etc. contribute to the quality of the neutrino reconstruction.

Uncertainty	Value [%]
Track efficiency	3.1
Cluster efficiency	6.8
K_L production and interactions	1.7
Lepton identification	2.9
π^0 identification	5.2
$B^+ \rightarrow \eta \ell^+ \nu_\ell$ Form-Factor	-
$q\bar{q}$ -Continuum Normalization	5.2
$b \rightarrow c\ell\nu$ Normalization	9.1
$\mathcal{B}(B \rightarrow u\ell\nu)$	0.9
$\mathcal{B}(\eta \rightarrow \pi^+ \pi^- \pi^0)$	1.8
NN configuration	13.1
NN training	10.8
$N_{B\bar{B}}$	0.7
Total	22.3

Table 7.1: Summary of systematic uncertainties given relative to the nominal branching fraction.

The uncertainty due to the tracking efficiency is evaluated on dedicated ntuples that are produced as recommended by the *BABAR* Tracking Efficiency Task Force [28]. The complete reconstruction is repeated but for this study tracks are eliminated at random with a certain probability given by the estimated uncertainty per track shown in Tab.7.2. The complete analysis is repeated on these modified ntuples and shows a deviation of 3.1% from the nominal branching fraction.

Run Period	Systematic uncertainty per track (%)
Run 1	0.51
Run 2	0.35
Run 3	0.26
Run 4	0.41
Run 5	0.45

Table 7.2: Systematic uncertainty on the track reconstruction efficiency per track for different run periods.

Similarly, the systematic uncertainty due to the photon efficiency uncertainty is considered by eliminating photons at random with an energy dependent probability, given in Tab. 7.3. The *BABAR* Neutral Particle group is using two different methods to estimate the single photon uncertainties. One using a $\tau \rightarrow \rho/\pi\nu$ sample for photon energies $E_\gamma < 2.5$ GeV [29], the other using a $e^+e^- \rightarrow \mu^+\mu^-\gamma$ sample for photon energies $1 \text{ GeV} < E_\gamma < 7 \text{ GeV}$ [30]. The analysis repeated on

these modified ntuples shows a deviation of 6.8% from the nominal branching fraction.

Energy	Systematic uncertainty per photons (%)
$E_\gamma < 1 \text{ GeV}$	1.8
$1 \text{ GeV} < E_\gamma < 7 \text{ GeV}$	0.7

Table 7.3: *Systematic uncertainty on the photon reconstruction efficiency per photon for different energy ranges.*

7.1.2 K_L^0 Production and Interactions

Decays with K_L^0 s involved have a substantial impact on the neutrino reconstruction quality, as K_L^0 s – due to their relatively long lifetime – deposit only a small fraction of their energy in the electromagnetic calorimeter and therefore are hard to identify and to reconstruct. Hence the proper simulation of their interactions in the detector and the knowledge of their production rate is important. Dedicated ntuples are produced with systematic changes in the reconstruction to account for these uncertainties [2]. The uncertainty resulting from the K_L^0 uncertainties is 1.7%.

7.1.3 Lepton Identification Efficiency

The uncertainty in the efficiencies of electron and muon identification have been estimated by other *BABAR* analyses and are 1.4% [31] and 3% [32]. To quantify the effect, the MC samples are scaled both up and down by those uncertainties and the analysis is then repeated. The larger discrepancy from the nominal branching ratio is taken as the systematic uncertainty. It is 2.8%.

7.1.4 Neutral Pion Efficiency

As recommended by the *BABAR* Neutral Particle Group [29] an uncertainty of 3% per π^0 is assigned for the π^0 reconstruction efficiency. Again, the MC samples are scaled both up and down by those uncertainties and the analysis is then repeated and the larger deviation from the nominal branching fraction is taken as the systematic uncertainty. It is 5.1%.

7.2 Physics Modeling

The uncertainties in the physics modeling and simulation of MC samples especially in the main backgrounds introduce further systematic uncertainties into the analysis. Within the scope of this work, it has not been possible to study the

uncertainties introduced by the theoretical $B^+ \rightarrow \eta \ell^+ \nu_\ell$ form-factor calculations. As far as it is known from other exclusive analyses the effect is expected to be small compared to the total systematic uncertainties.

7.2.1 $q\bar{q}$ -Continuum Normalization

The normalization of the $q\bar{q}$ -Continuum background is discussed in section 4.3.1. The normalization factors are estimated to be $f_{q\bar{q}}^e = (94.8 \pm 6.3)\%$ for electrons and $f_{q\bar{q}}^\mu = (78.9 \pm 4.4)\%$ for muons. To estimate the error due to the uncertainties in the normalization, the factors are scaled up and down according to their errors and the analysis is repeated. The largest deviation from nominal branching ratio – 5.2% – is taken as the systematic uncertainty.

7.2.2 $b \rightarrow c\ell\nu$ Normalization

As discussed in section 4.3.2, there is an excess of $b \rightarrow c\ell\nu$ events in the MC simulation. This is quantified in chapter 6, when the MC samples are fit to the real data and a normalization factor $f_{b \rightarrow c\ell\nu} = (88.9 \pm 3.9)\%$ for the $b \rightarrow c\ell\nu$ background sample is obtained. To check the stability of this factor it has been computed at different analysis steps and on a sideband sample. For this study the signal branching fraction is fixed to the measured value and only the $b \rightarrow c\ell\nu$ normalization is floating. The following $f_{b \rightarrow c\ell\nu}$ scale factors have been obtained at different stages of the analysis:

- Only the analysis selection applied: $f_{b \rightarrow c\ell\nu} = (84.1 \pm 1.5)\%$
Discrepancy to the MC simulation: $(1.000 - 0.841) = 15.9\%$
- No $c\ell\nu$ -net applied: $f_{b \rightarrow c\ell\nu} = (84.5 \pm 1.3)\%$
Discrepancy to the MC simulation: $(1.000 - 0.845) = 15.5\%$
- Final selection but outside the signal region ($m_{\text{ES}} > 5.23 \text{ GeV}$ and $533 \text{ MeV}/c^2 < m_{\pi^+\pi^-\pi^0} < 557 \text{ MeV}/c^2$): $f_{b \rightarrow c\ell\nu} = (88.0 \pm 3.4)\%$
Discrepancy to the MC simulation: $(1.000 - 0.880) = 12.0\%$

Within their uncertainties, the values are consistent with each other and the value obtained in the nominal fit ($f_{b \rightarrow c\ell\nu} = (88.9 \pm 3.9)\%$).

The error cannot be accounted for by varying the $b \rightarrow c\ell\nu$ normalization within its uncertainty, as it is done for the $q\bar{q}$ -continuum normalization, since the $b \rightarrow c\ell\nu$ fraction is floated in the fit. Therefore, this would yield the same result as the nominal fit.

Instead, the highest deviation of the scaling factors from one, 15.9%, is taken and folded with the correlation (chapter 6.4) between the signal and the $b \rightarrow c\ell\nu$ normalization factors to estimate the systematic uncertainty. The uncertainty is 9.1%.

7.2.3 $B \rightarrow ul\nu$ Branching Fraction

The current best value and its uncertainty of the inclusive branching fraction for $B \rightarrow ul\nu$ is $\mathcal{B}(B \rightarrow ul\nu) = (2.26 \pm 0.33) \cdot 10^{-3}$ [33]. The $B \rightarrow ul\nu$ branching fraction is varied within its errors and the $B^+ \rightarrow \eta\ell^+\nu_\ell$ branching fraction is extracted again. The discrepancy from the nominal value leads to an uncertainty in the measured branching fraction of 0.9%.

7.2.4 $\eta \rightarrow \pi^+\pi^-\pi^0$ Branching Fraction

As mentioned in section 6.2, the $\eta \rightarrow \pi^+\pi^-\pi^0$ branching fraction is known with limited precision : $\mathcal{B}(\eta \rightarrow \pi^+\pi^-\pi^0) = (22.7 \pm 0.4)\%$. It is therefore another source of systematic error for this analysis that yields an uncertainty of 1.8%.

7.3 Neural-Networks

7.3.1 Neural-Network Configuration

To study the uncertainty due to the choice of input variables for the NNs, the analysis is performed with NN configurations different from the nominal one, shown in Tab. 7.4.

Net	Input Variables $q\bar{q}$ -net	Input Variables $c\bar{l}\nu$ -net
Nominal	$\frac{m_{\text{miss}}^2}{2E_{\text{miss}}}, \Theta_{\text{miss}}, R_2, L_2, \cos(\Theta_{\text{BY}}), \cos(\Theta_{\text{thrust}}), \cos(\Theta_{\text{HL}}), p_{\text{lep}}^*, p_{\text{pi}^0}, \cos(\Theta_L), \Delta E, p_{\text{had}}^*$	Same as $q\bar{q}$ -net
A	$\frac{m_{\text{miss}}^2}{2E_{\text{miss}}}, \Theta_{\text{miss}}, R_2, L_2, \cos(\Theta_{\text{thrust}}), p_{\text{lep}}^*, p_{\text{pi}^0}, \Delta E, p_{\text{had}}^*$	Same as $q\bar{q}$ -net
B	$\frac{m_{\text{miss}}^2}{2E_{\text{miss}}}, \Theta_{\text{miss}}, R_2, L_2, \cos(\Theta_{\text{BY}}), \cos(\Theta_{\text{thrust}}), \cos(\Theta_L)$	Same as $q\bar{q}$ -net
C	$\frac{m_{\text{miss}}^2}{2E_{\text{miss}}}, \Theta_{\text{miss}}, R_2, L_2, \cos(\Theta_{\text{thrust}}), \cos(\Theta_{\text{HL}}), \cos(\Theta_L), \Delta E$	$\frac{m_{\text{miss}}^2}{2E_{\text{miss}}}, \Theta_{\text{miss}}, \cos(\Theta_{\text{HL}}), \cos(\Theta_L), p_{\text{had}}^*$
D	$\frac{m_{\text{miss}}^2}{2E_{\text{miss}}}, \Theta_{\text{miss}}, R_2, L_2, \cos(\Theta_{\text{thrust}}), \Delta E$	$\frac{m_{\text{miss}}^2}{2E_{\text{miss}}}, \Theta_{\text{miss}}, \Delta E$

Table 7.4: Neural-network configurations for the nominal and four different neural-networks.

With those configurations all the analysis steps are repeated and for each the branching fraction is extracted. The results are shown in Tab. 7.5. Within their uncertainties the branching fractions obtained with different NN configurations agree well. The nominal configuration is chosen because it yields the highest $S/\sqrt{S+B}$ ratio and therefore the smallest statistical uncertainty. The highest

Net	Branching Ratio [10^{-5}]	Error [10^{-5}]	Relative Error
Nominal NN	6.47	1.48	22.9 %
A	5.72	1.40	24.5 %
B	6.21	1.61	25.8 %
C	5.62	1.43	25.4 %
D	6.07	1.58	26.0 %

Table 7.5: Branching fractions with their statistic uncertainties for the different neural-network configurations.

deviation from the nominal branching fraction value is taken as the systematic uncertainty from this study. It is 13.1%.

7.3.2 Neural-Network Training

In order to estimate the uncertainty of the NN training process, both the $q\bar{q}$ -net and the $cl\nu$ -net are trained 100 times. After each new training the branching fraction is extracted.

Since this study is very time consuming, this procedure was repeated only 100 times. Fig. 7.1 shows the distribution of the branching fraction obtained from

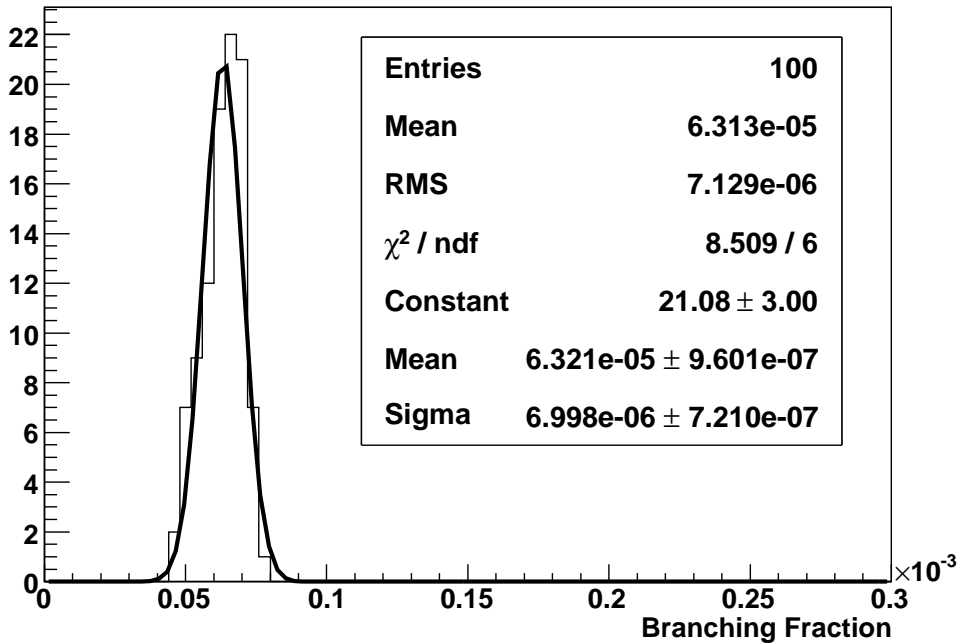


Figure 7.1: Distribution of the branching fraction for 100 different neural-networks trainings and a single Gaussian fit to it.

the 100 fits. A Gaussian is fit to the distribution and its full width of 10.8 % is taken as the NN training uncertainty.

7.4 $B\bar{B}$ Counting

The luminosity and number of $B\bar{B}$ estimation described in [21] has an uncertainty of 1.1%. This is taken into account by varying this number within its error and recalculating the branching fraction. The resulting uncertainty is 0.7%.

7.5 Summary of Systematic Uncertainties

A summary of all systematic uncertainties estimated is shown in Tab. 7.1. The main contributions are due to the uncertainties in the NNs and the uncertainty in the $b \rightarrow c\ell\nu$ background.

In case of the NNs, the two uncertainties might not be uncorrelated, as the uncertainty in the training process should also somehow be reflected in the uncertainties due to different NN input variable configurations. However, as the effect was not studied due to time constraints, the uncertainties are taken to be uncorrelated and therefore the uncertainty on the NNs might be overestimated. In addition, the uncertainty might also be reduced by applying a different multivariate analysis method, like boosted decision trees, fisher discriminants or likelihood estimators. This was not possible within the time frame of this work.

The uncertainty in the $b \rightarrow c\ell\nu$ background could be studied using a background enriched sample, e.g. the η mass sidebands. This was not possible with the ntuples used in this analysis, as the sidebands were quite limited.

The total systematic uncertainty, i.e. the single uncertainties added in quadrature, is 22.3%, which translates into a measured $B^+ \rightarrow \eta\ell^+\nu_\ell$ branching fraction:

$$\mathcal{B}(B^+ \rightarrow \eta\ell^+\nu_\ell) = (6.47 \pm 1.48_{stat.} \pm 1.44_{syst.})$$

Chapter 8

Conclusion and Outlook

In this thesis the measurement of the branching fraction of the charmless semileptonic B -decay $B^+ \rightarrow \eta \ell^+ \nu_\ell$ has been performed. Neural-network techniques are used to distinguish the $B^+ \rightarrow \eta \ell^+ \nu_\ell$ signal from the main backgrounds, the $q\bar{q}$ -continuum and $b \rightarrow c\ell\nu$ backgrounds. The analysis yields 285 ± 8 signal events over $4,682 \pm 48$ background events. The systematic uncertainties are dominated by the uncertainties resulting from the neural-networks and the lack of understanding of the $b \rightarrow c\ell\nu$ -background.

The result is

$$\mathcal{B}(B^+ \rightarrow \eta \ell^+ \nu_\ell) = (6.47 \pm 1.48_{\text{stat.}} \pm 1.44_{\text{syst.}}) \cdot 10^{-5} = (6.47 \pm 2.06) \cdot 10^{-5},$$

where the statistic, systematic and the total¹ uncertainties are given. The measurement agrees well with the current world-average of $(8 \pm 4) \cdot 10^{-5}$ [4], the CLEO measurement $(8.4 \pm 3.1_{\text{stat.}} \pm 1.8_{\text{syst.}}) \cdot 10^{-5}$ [5] and the preliminary result of the tagged *BABAR* analysis of $(8.4 \pm 2.7_{\text{stat.}} \pm 2.1_{\text{syst.}}) \cdot 10^{-5}$ [6] and has significantly smaller uncertainties.

The systematic uncertainties resulting from the neural-networks might be reducible by applying other multivariate analysis techniques such as boosted decision trees, fisher discriminants or likelihood estimators. This was not possible within the time frame of this work. To further improve the analysis, the uncertainty in the $b \rightarrow c\ell\nu$ -background must be studied in more detail. The impact of the uncertainties in the theoretical form-factor calculations on the signal acceptance has not been studied yet and has to be quantified to complete the analysis. Within the current accuracy of the analysis it is not expected to be a major contribution to the total systematic uncertainty [5].

In the future, the statistic uncertainties can be reduced by not only reconstructing the η in the charged $\eta \rightarrow \pi^+ \pi^- \pi^0$ (23%) final state but also in the neutral modes: $\eta \rightarrow \gamma\gamma$ (39%) and $\eta \rightarrow \pi^0 \pi^0 \pi^0$ (33%). In addition, *BABAR* plans to at least double the size of the data sample until the final shutdown, scheduled

¹The statistic and systematic uncertainties are added in quadrature.

for 2008. This would amount to roughly three times the sample size used for this analysis. Hence, by reconstructing more η final states and with the final *BABAR* data sample a signal yield of more than 1000 events can be achieved.

A future extraction of $|V_{ub}|$ depends on a more reliable theoretical form-factor prediction. An alternate approach is the measurement of the form-factor shape in an q^2 -dependent analysis of the $B^+ \rightarrow \eta \ell^+ \nu_\ell$ decay. However, an overall normalization to the theoretical prediction would be needed to extract $|V_{ub}|$.

Bibliography

- [1] M. Kobayashi, T. Maskawa, Prog. Theor. Phys. **49** 652 (1973).
- [2] J. Dingfelder, M. Kelsey, V. Lüth, P. Andreas Walker, H. Wells Wulsin, Study of Charmless Semileptonic Decays $B \rightarrow \pi\ell\nu$ and $B \rightarrow \rho\ell\nu$ with Neutrino Reconstruction, BAD # 1520.
- [3] J. Dingfelder, A. Weinstein, M. Kelsey, V. Lüth, Study of Untagged Exclusive Charmless Semileptonic Decays $B \rightarrow \pi\ell\nu$ and $B \rightarrow \rho\ell\nu$, BABAR Analysis Document (BAD) # 531.
- [4] W.-M. Yao et al., The Review of Particle Physics, Journal of Physics G 33, 1 (2006).
- [5] S.B. Athar, Study of the q^2 dependence of $B^0 \rightarrow \pi^-\ell^+\nu_\ell$ and of $B \rightarrow \rho(\omega)\ell\nu$ and extraction of $|V_{ub}|$, Phys. Rev. D 68, 072003 (2003).
- [6] Alessia D’Orazio, Measurement of Branching Fractions of Exclusive Charmless Semileptonic Decays using the Recoil of Fully Reconstructed B mesons, BAD 1537 (2006).
- [7] D. Scora and N. Isgur, Semileptonic meson decays in the quark model: An update, Phys. Rev. D52, 2783-2812 (1995).
- [8] P. Ball and R. Zwicky, New results on $B \rightarrow \pi, K, \eta$ decay formfactors from light-cone sum rules, Phys. Rev. D71: 014015 (2005).
- [9] J. Shigemitsu *et al.*, Semileptonic B decays with $N(f) = 2 + 1$ dynamical quarks, e-Print Archive: hep-lat/0408019.
- [10] M. Okamoto *et al.*, Semileptonic $D \rightarrow \pi/K$ and $B \rightarrow \pi/D$ decays in 2+1 flavour lattice QCD, e-Print Archive: hep-lat/0409116.
- [11] B. Aubert *et al.* [BABAR Collaboration], Nucl. Instrum. Meth. A **479**, 1 (2002).
- [12] <http://bbr-onlwww.slac.stanford.edu:8080/babarrc/perfdata.html>, Public BABAR website.

- [13] Brandt, Thorsten, Likelihood-based electron identification, BAD # 396.
- [14] Mohapatra, Ajit, Studies of A Neural Net Based Muon Selector for the BaBar Experiment, BAD # 474.
- [15] Stephanie Majewski, PID Likelihood Selectors, http://www.slac.stanford.edu/BFROOT/www/Physics/Tools/Pid/Hadrons/pid_summarytable.html, Internal *BABAR* webpage.
- [16] <http://www.slac.stanford.edu/BFROOT/www/Physics/Tools/Pid/pid.html>, 2007, internal *BABAR* website.
- [17] S. Giani *et al.*, Geant – Detector Description and Simulation Tool, CERN Program Library Long Writeup W5013 (1994).
- [18] P. Ball and R. Zwicky, Phys. Rev. D71, 014015 (2005), arXiv:hep-ph/0412079v1.
- [19] P. Ball, private communication, January 2007.
- [20] D. Fortin, <http://www.slac.stanford.edu/bfroot/www/physics/analysis/awg/inclusivesl/common/dominiquehybrid.html/hybrid.html>, 2004, Internal *BABAR* webpage.
- [21] C. Hearty, “Hadronic Event Selection and B-Counting for Inclusive Charmonium Measurements”, BAD # 30 (2000).
- [22] Sylvie Brunet, David Cote, Martin Simard, Benoit F. Viaud, *BABAR* Analysis Document 740 (2005).
- [23] M. Mazur, Measurement of the exclusive branching fractions $B \rightarrow D^* \tau \nu$, BAD # 1111.
- [24] R. Brun, F. Rademakers, ROOT - An Object Oriented Data Analysis Framework, Proceedings AIHENP’96 Workshop, Lausanne, Sep. 1996, Nucl. Inst. & Meth. in Phys. Res. A 389 (1997) 81-86. See also <http://root.cern.ch/>.
- [25] A. Hocker, J. Stelzer, F. Tegenfeldt, H. Voss, K. Voss, A. Christov, S. Henrot-Versille, M. Jachowski, A. Krasznahorkay Jr., Y. Mahalalel, X. Prudent, P. Speckmayer, “TMVA - Toolkit for Multivariate Data Analysis” arXiv::physics/0703039.
- [26] R. J. Barlow and C. Beeston, Fitting using Finite Monte Carlo Samples, Comput. Phys. Commun. 77, 219-228 (1993).
- [27] F. James, MINUIT – Function Minimization and Error Analysis, CERN Program Library Long Writeup D506 (1994).

- [28] <http://www.slac.stanford.edu/BFROOT/www/Physics/TrackEfficTaskForce/TrackingTaskForce-2006.html>.
- [29] M. T. Allen, a Study of π^0 Efficiency, BAD # 870.
- [30] D. Payne, High Energy Single Photon Efficiency Using $e^+e^- \rightarrow \mu^+\mu^-\gamma$ events, BAD # 1110.
- [31] B. Aubert et al. (*BABAR* Collaboration), Measurement of the ratio $\mathcal{B}(B^+ \rightarrow X e \nu) / \mathcal{B}(B^0 \rightarrow X e \nu)$ hep-ex/0607111.
- [32] B. Aubert et al. (*BABAR* Collaboration), Phys. Rev. Lett. 97,221801 (2006).
- [33] Heavy Flavor Averaging Group, <http://www.slac.stanford.edu/xorg/hfag/>, Semileptonic Averages, ICHEP 2006.

Appendix A

Kaon Veto Study

The performance of the kaon veto on the η 's charged pion daughters was studied on MC samples before the veto was applied. Only events in the signal region as defined at this time ($m_{\text{ES}} > 5.23 \text{ GeV}/c^2$, $-0.3 \text{ GeV} < \Delta E < 0.5 \text{ GeV}$ and $0.528 \text{ GeV}/c^2 < m_{\pi^+\pi^-\pi^0} < 0.568 \text{ GeV}/c^2$) were used.

Using the generator level information in the MC samples, a “true η -meson” reconstructed from true charged pions can be distinguished from a “fake η -meson” wrongly reconstructed from at least one true charged kaon.

In the $B^+ \rightarrow \eta \ell^+ \nu_\ell$ signal sample only 9% of the reconstructed η -mesons are “fake η -mesons”, while in the $b \rightarrow c \ell \nu$ -background sample 31% and in the combined other background samples 17% of the η -mesons are “fake η -mesons”.

The kaon selector, discussed in chapter 3.2.6, vetoes 88% of the “fake η -mesons” in the $b \rightarrow c \ell \nu$ -background sample and 98% of the “fake η -mesons” in the signal sample, while 88% of the true η -mesons in the signal sample pass the veto. In the other MC samples 33% of the events are vetoed.

In conclusion, the kaon veto significantly reduces the main background and almost all signal events are kept.

Appendix B

Neural-Network Input Distributions

The input variables of the NN are shown in the following, each with different selection criteria applied, namely with the analysis selection, the additional $q\bar{q}$ -net and the additional $cl\nu$ -net. The signal and the $b \rightarrow cl\nu$ -background MC are scaled by the factors obtained in chapter 6, $f_{\text{signal}} = 0.773$ and $f_{b \rightarrow cl\nu} = 0.889$. The more restrictive the selection criteria are, i.e. the less background dominated, the better the simulation agrees with the data. The legend for all distributions is shown in Fig. B.1.

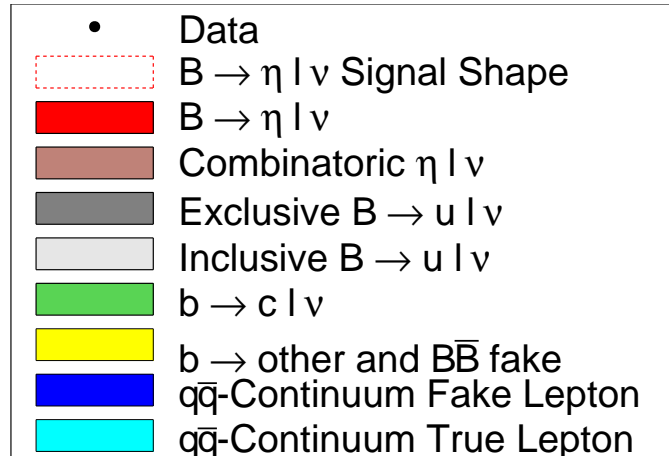


Figure B.1: Legend for the distributions shown here.

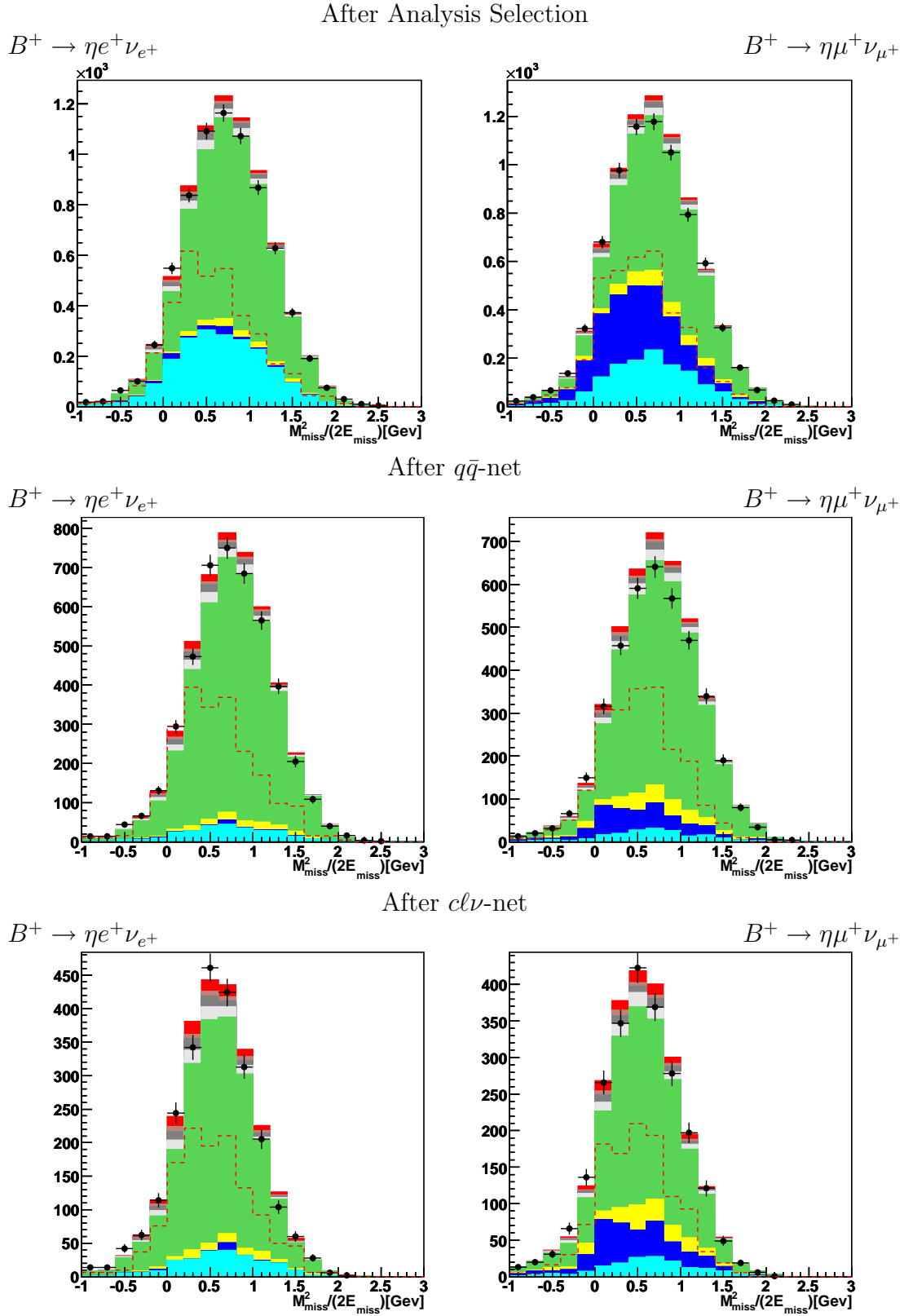


Figure B.2: Distribution of the energy over the mass $m_{\text{miss}}^2/(2E_{\text{miss}})$ of the neutrino candidate after the analysis section applied (top), after the $q\bar{q}$ -net applied (middle) and after $cl\nu$ -net applied (bottom).

After Analysis Selection

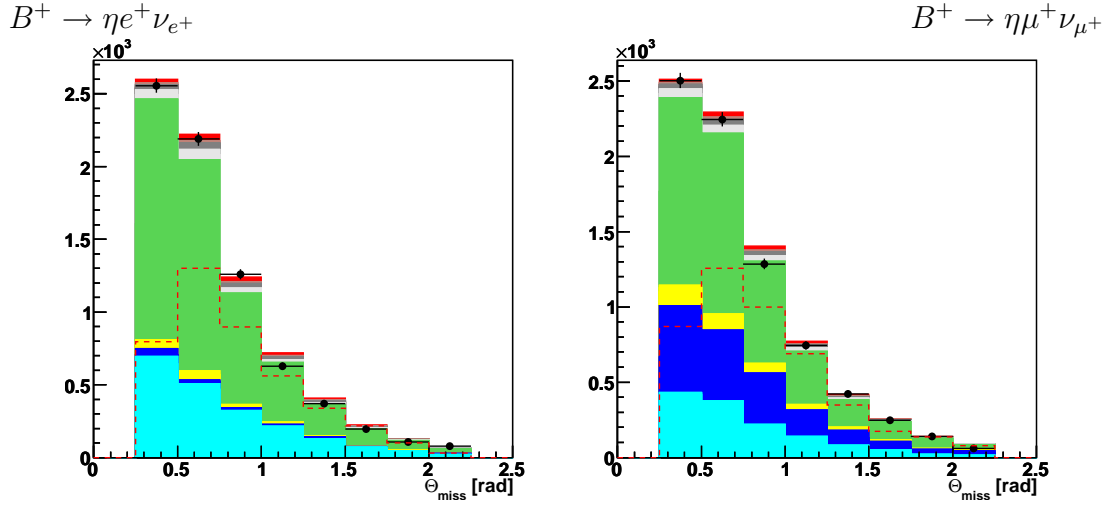
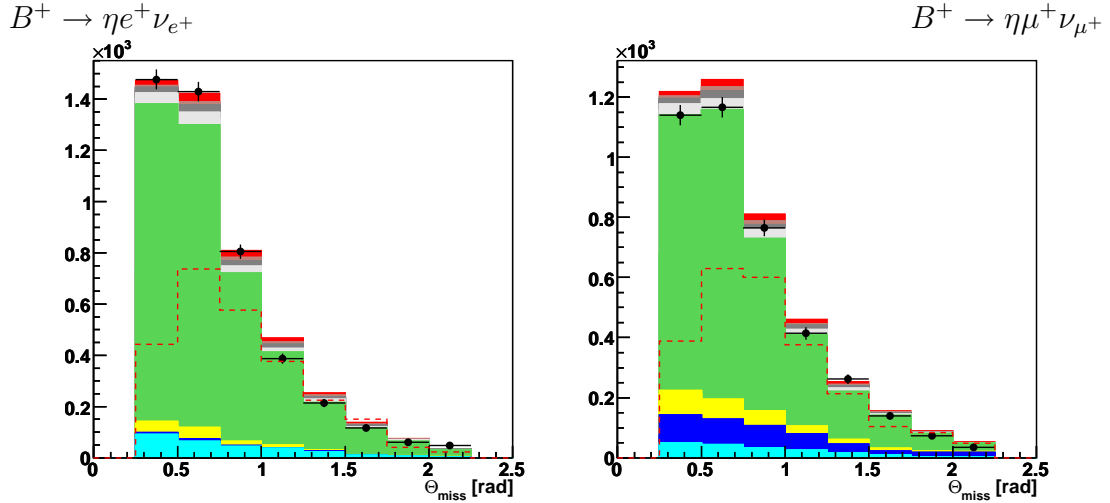
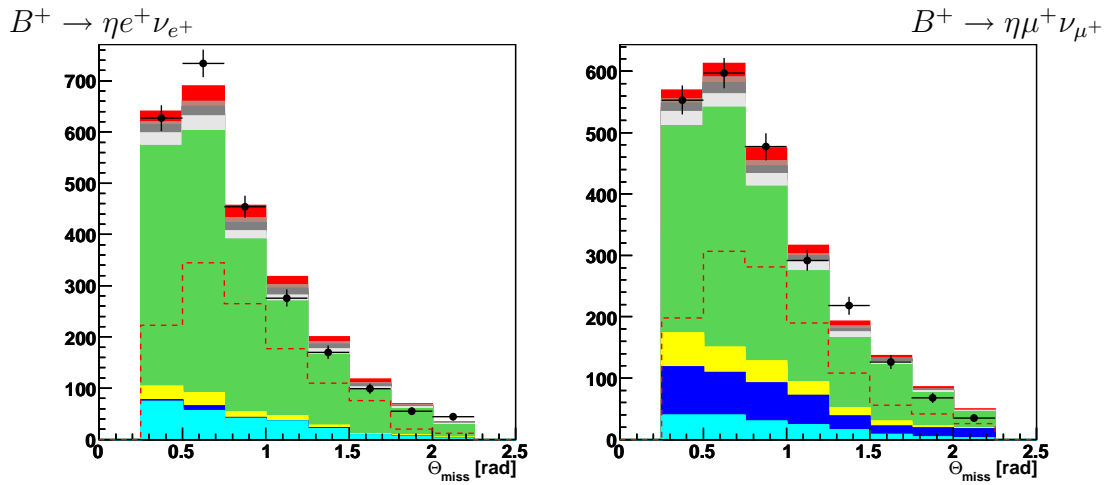
After $q\bar{q}$ -netAfter $cl\nu$ -net

Figure B.3: Distribution of $\Theta_{p_{\text{miss}}}$ the angle between the neutrino momentum and the beam axis after the analysis section applied (top), after the $q\bar{q}$ -net applied (middle) and after $cl\nu$ -net applied (bottom).

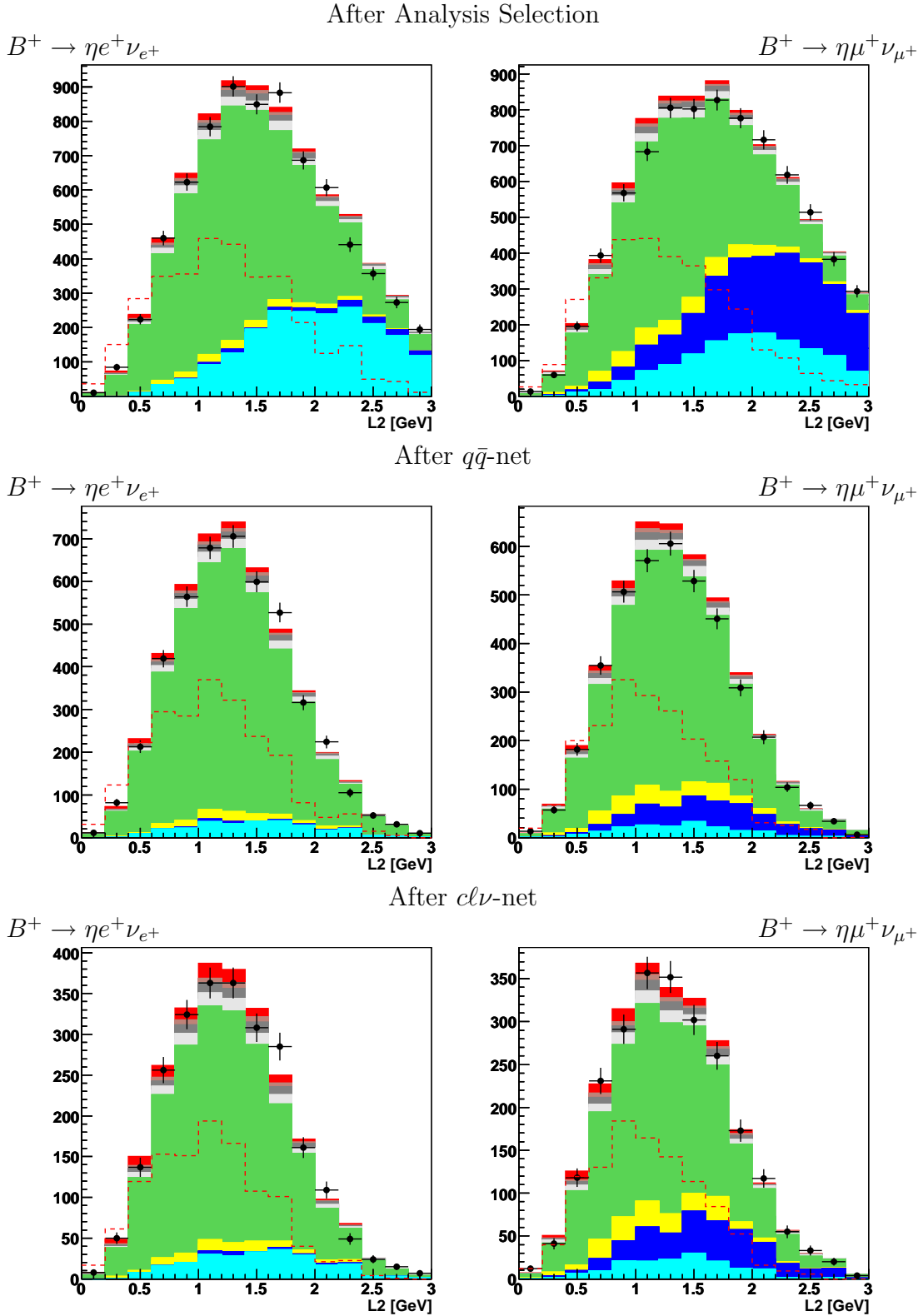


Figure B.4: Distribution of L_2 , the second Legendre moment after the analysis section applied (top), after the $q\bar{q}$ -net applied (middle) and after $cl\nu$ -net applied (bottom).

After Analysis Selection

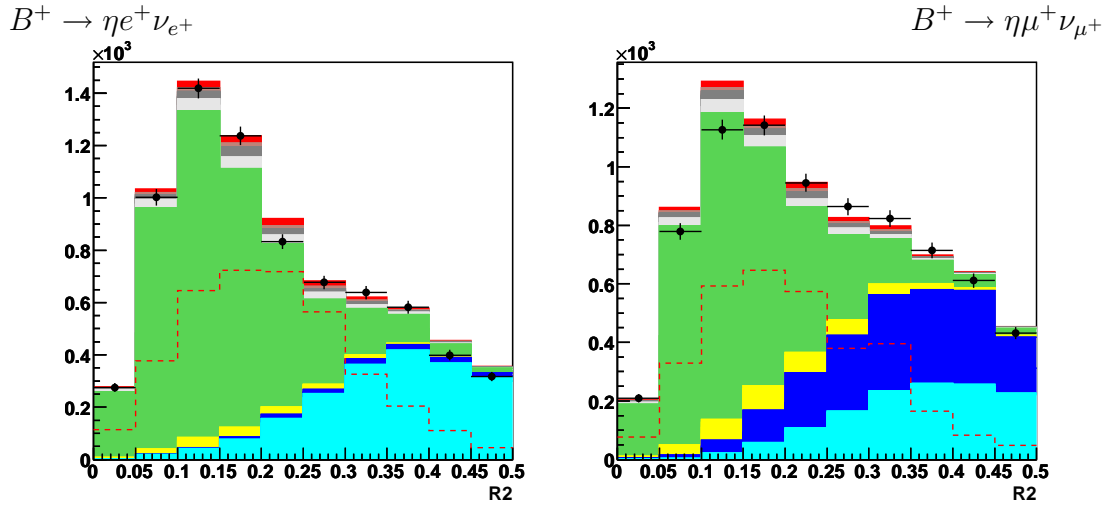
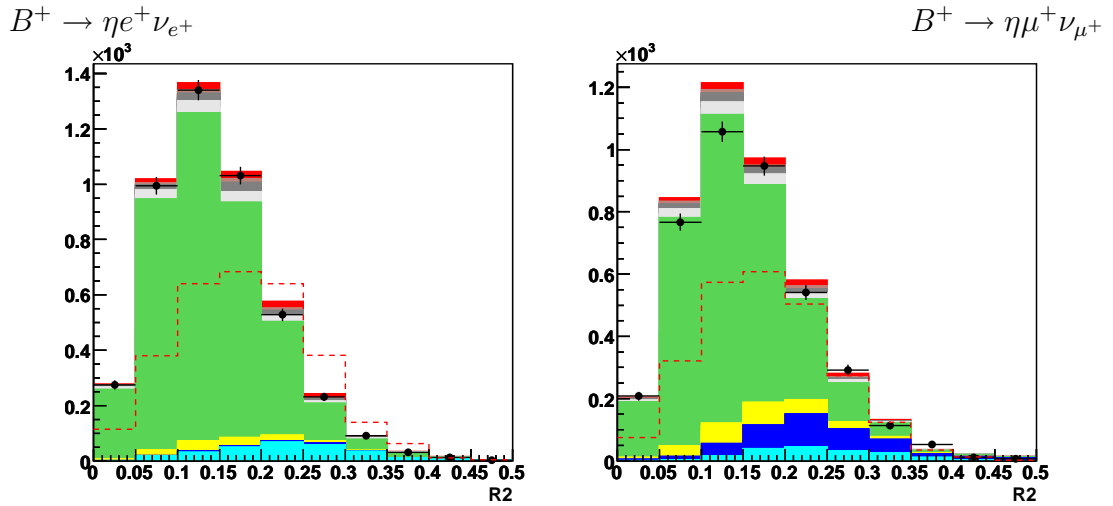
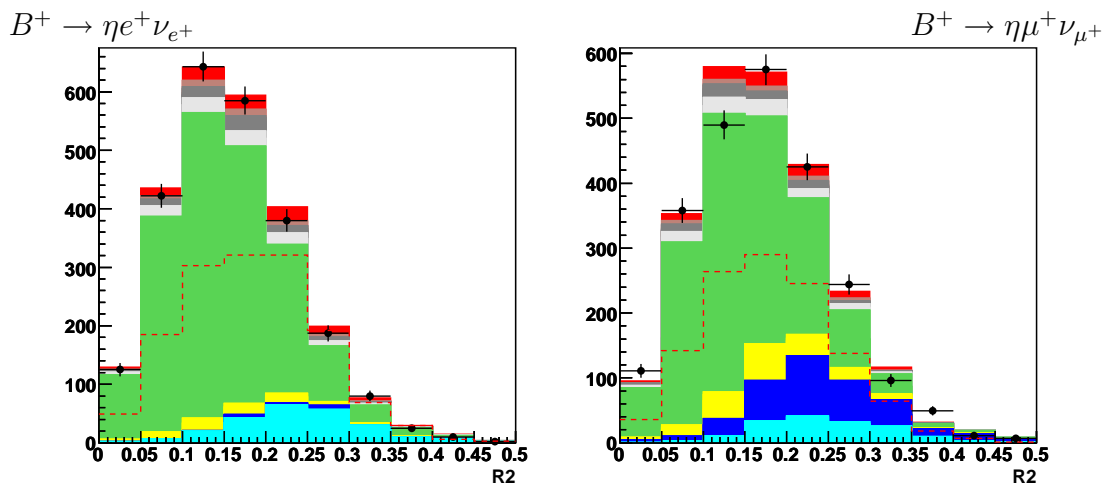
After $q\bar{q}$ -netAfter $cl\nu$ -net

Figure B.5: Distribution of the second Fox-Wolfram moment R_2 after the analysis selection applied (top), after the $q\bar{q}$ -net applied (middle) and after $cl\nu$ -net applied (bottom).

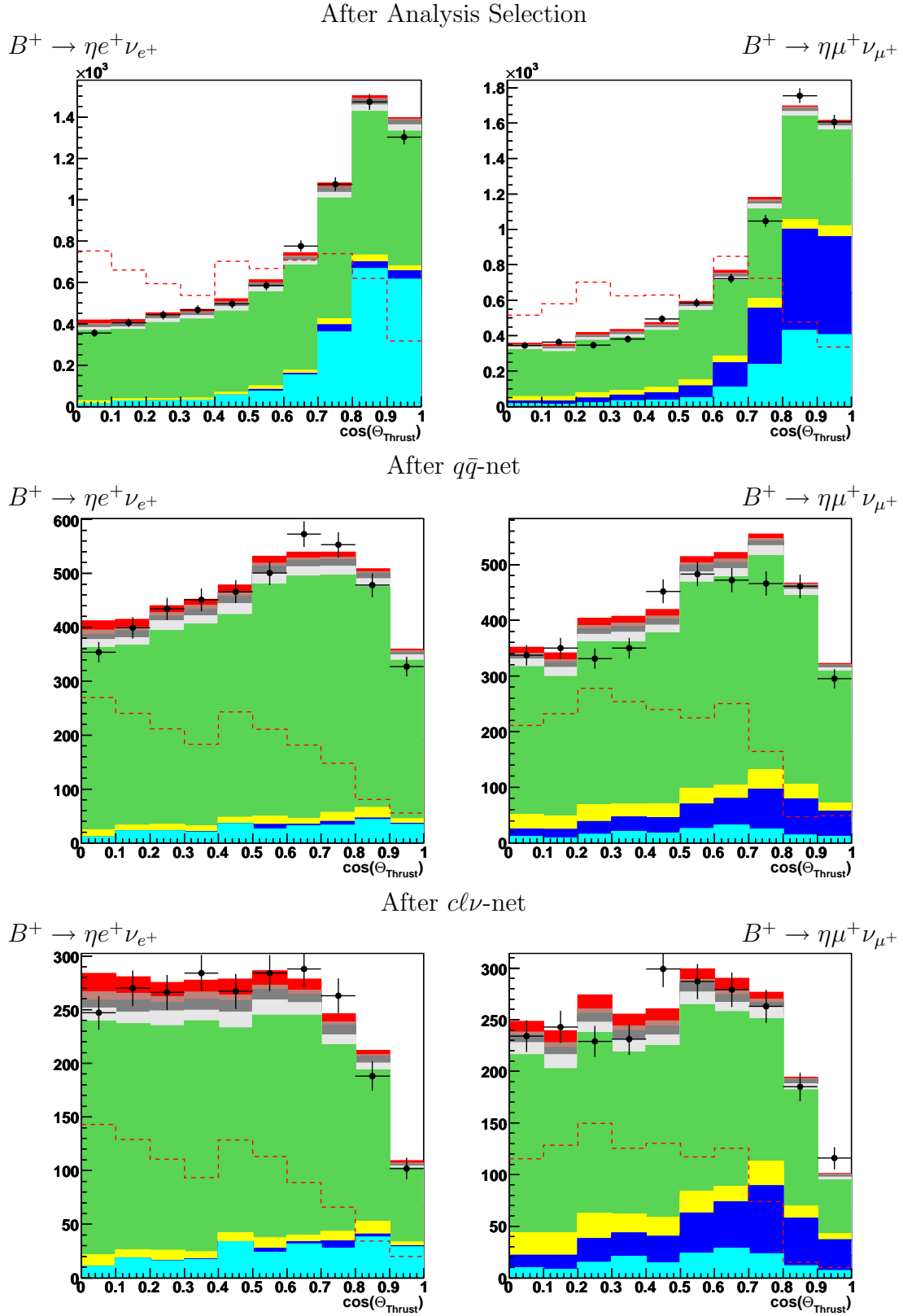


Figure B.6: Distribution of the cosine of the angle between the thrust axes of the Y -system and of the whole event $\cos(\Theta_{Thrust})$ after the analysis section applied (top), after the $q\bar{q}$ -net applied (middle) and after $cl\nu$ -net applied (bottom).

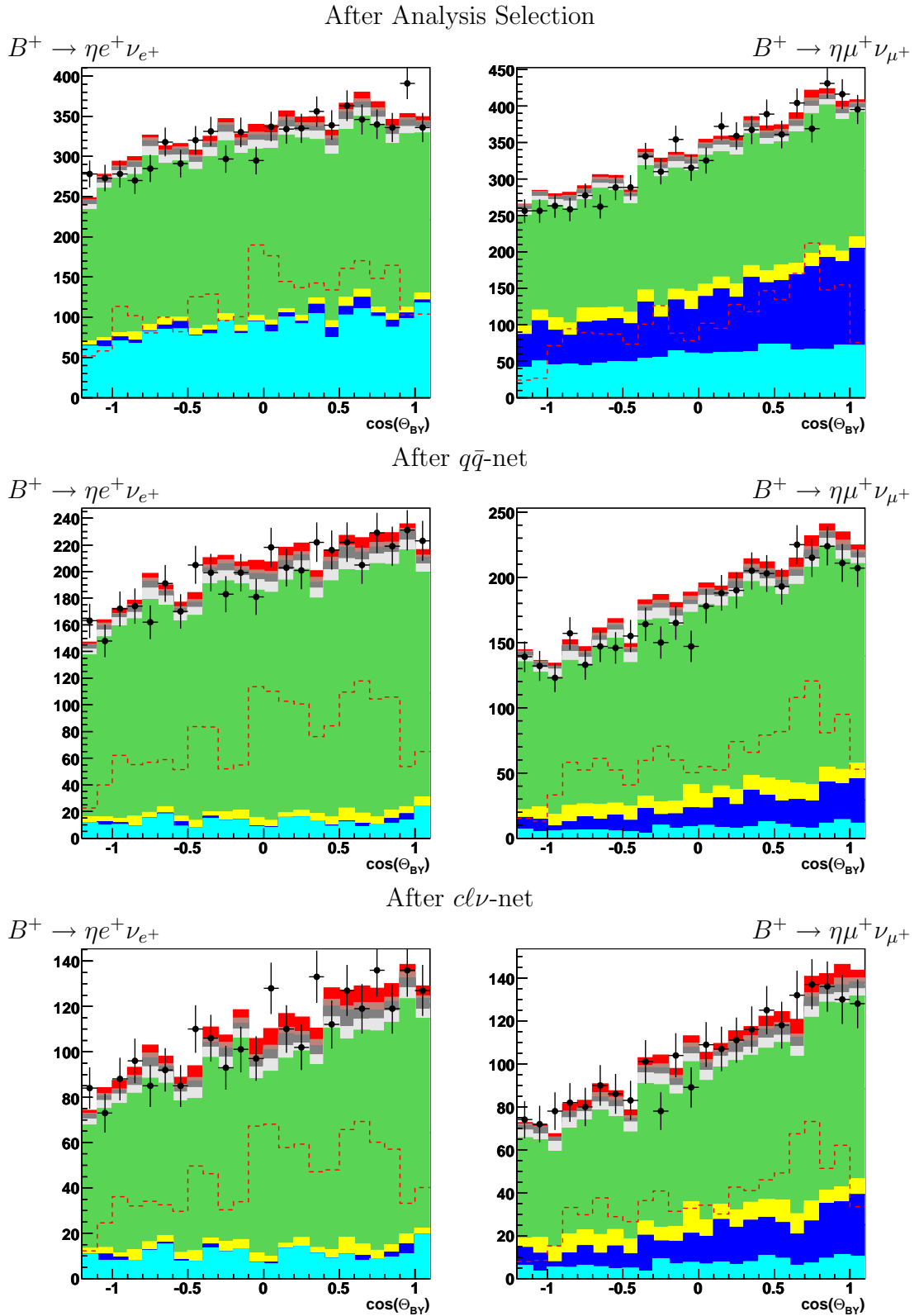


Figure B.7: Distribution of $\cos(\Theta_{BY})$, the cosine of the angle between the Y -candidate and the B -meson after the analysis section applied (top), after the $q\bar{q}$ -net applied (middle) and after $cl\nu$ -net applied (bottom).

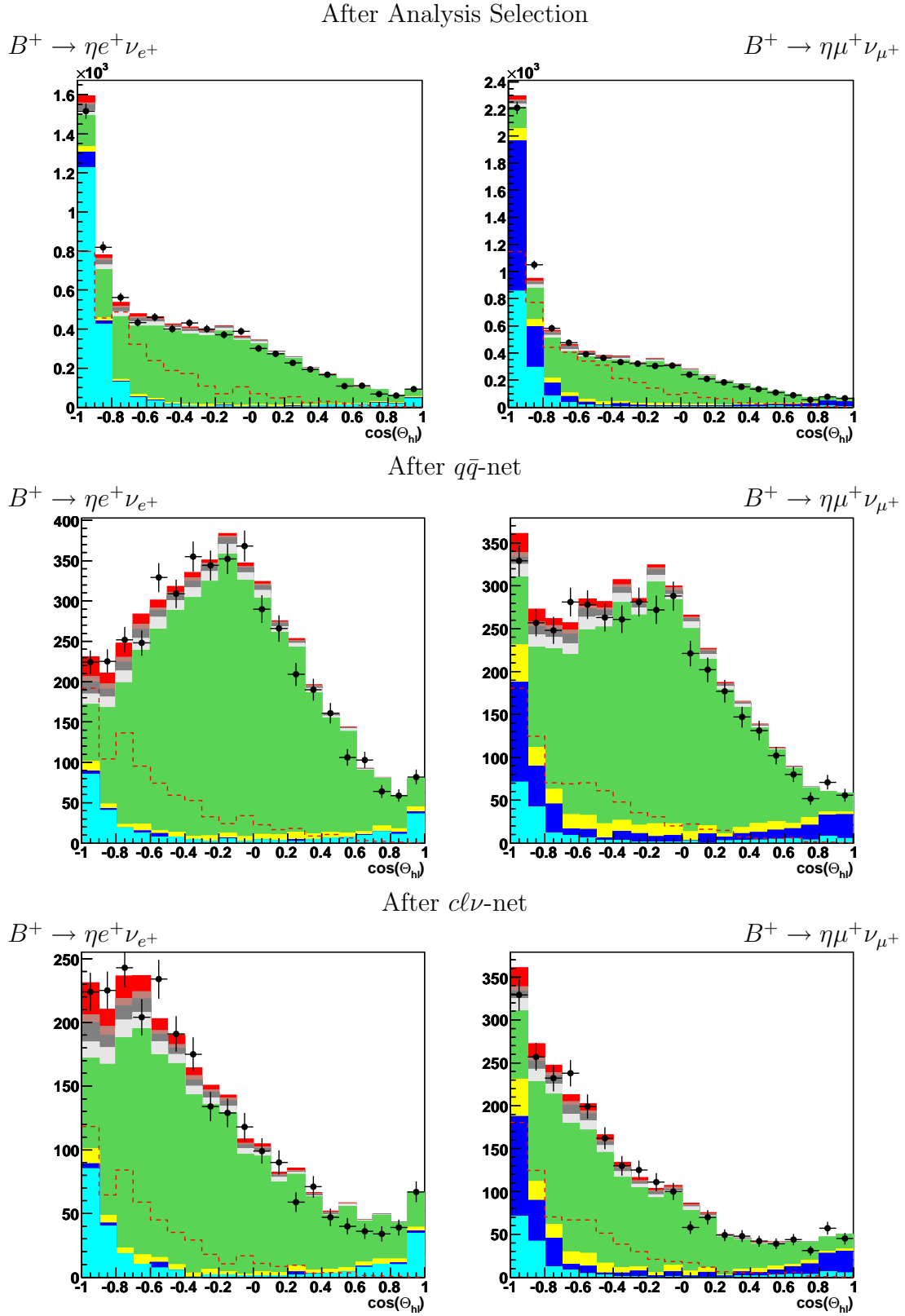


Figure B.8: Distribution of $\cos(\Theta_{hl})$, the cosine of the angle between the η and the lepton taken in the laboratory system after the analysis section applied (top), after the $q\bar{q}$ -net applied (middle) and after $cl\nu$ -net applied (bottom).

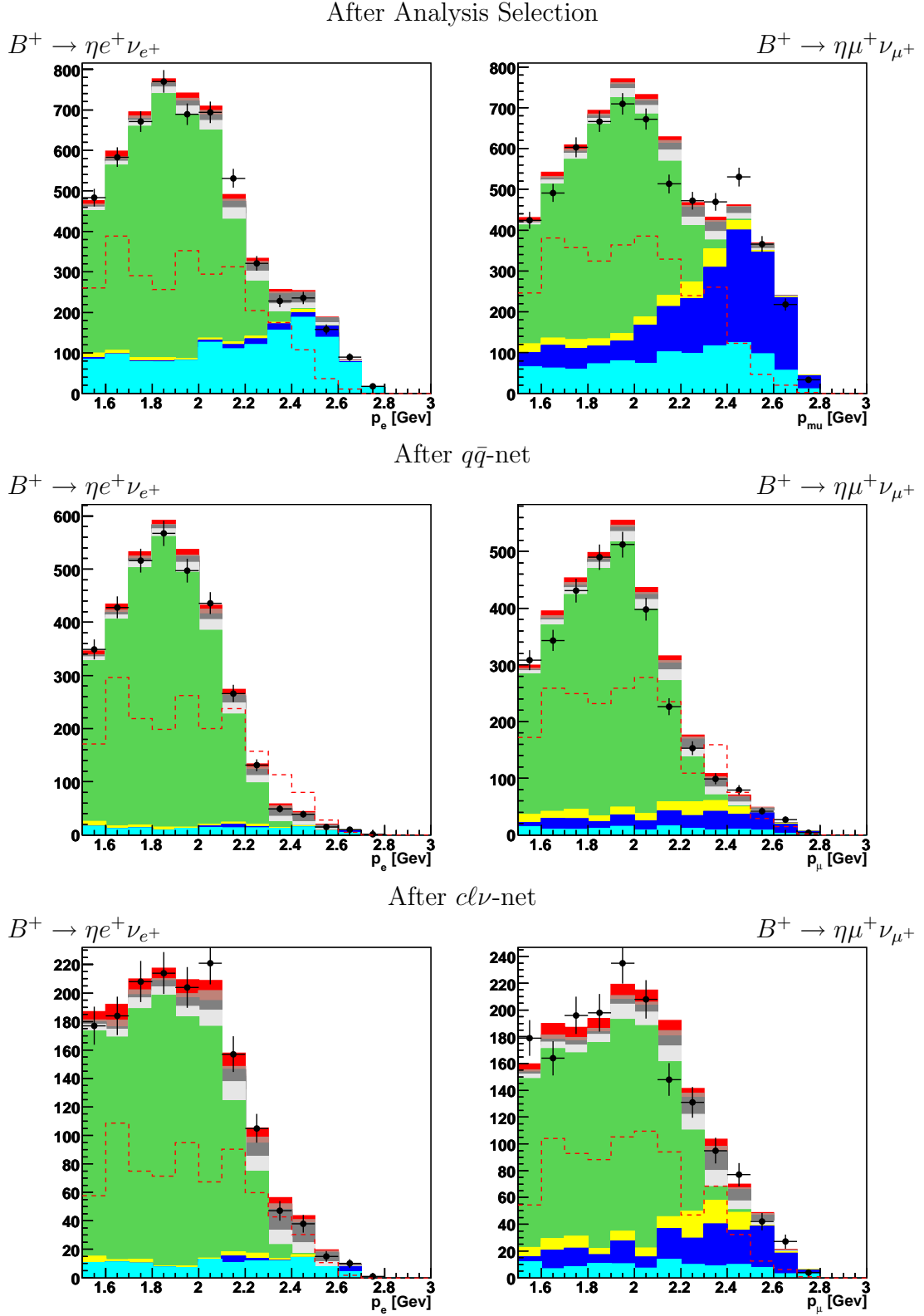


Figure B.9: Distribution of the lepton momentum p_i^* in the $\Upsilon(4S)$ system after the analysis section applied (top), after the $q\bar{q}$ -net applied (middle) and after $cl\nu$ -net applied (bottom).

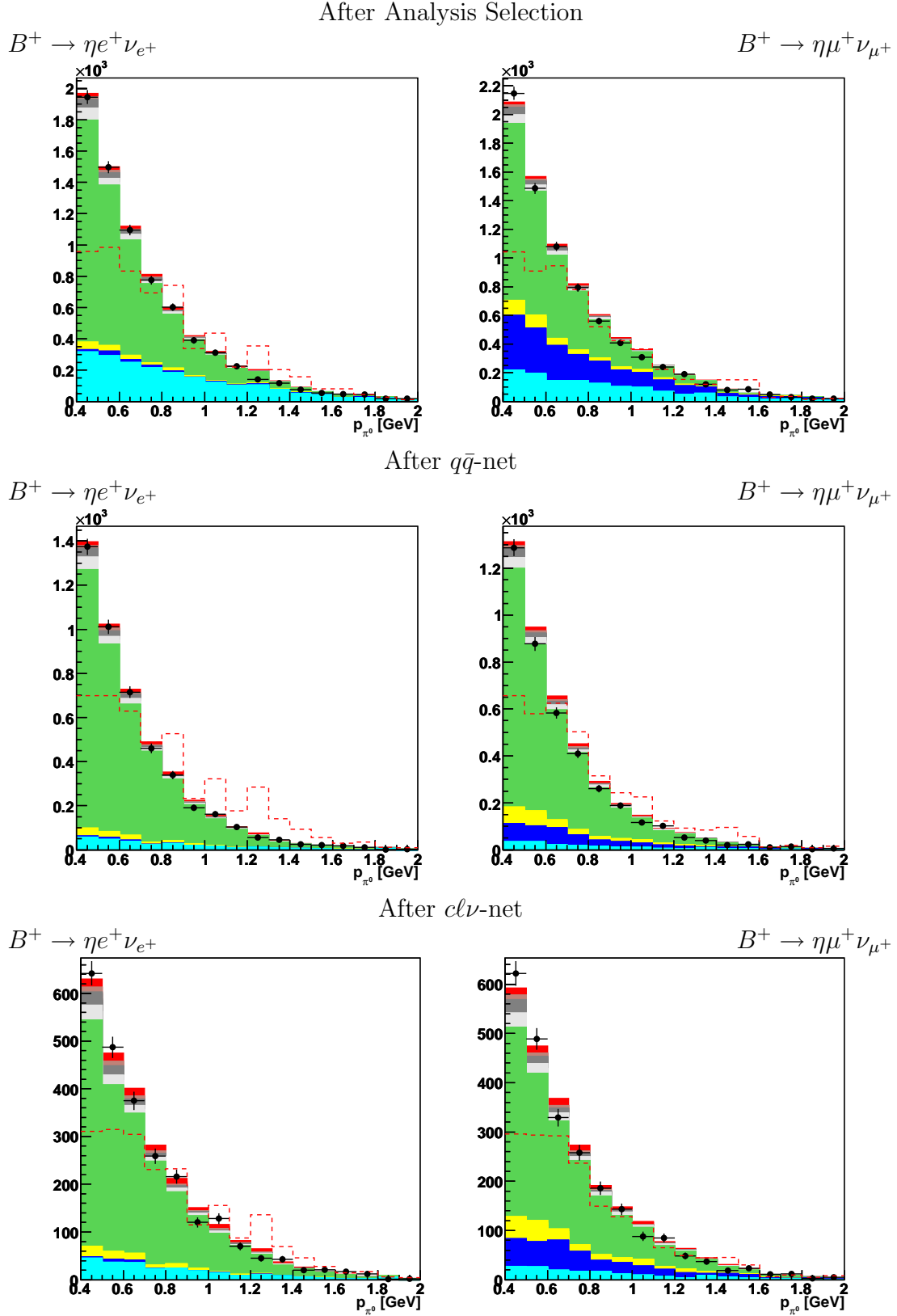


Figure B.10: Distribution of the momentum $p_{\pi^0}^*$ of the π^0 coming from the η decay measured in the $\Upsilon(4S)$ system after the analysis section applied (top), after the $q\bar{q}$ -net applied (middle) and after $cl\nu$ -net applied (bottom).

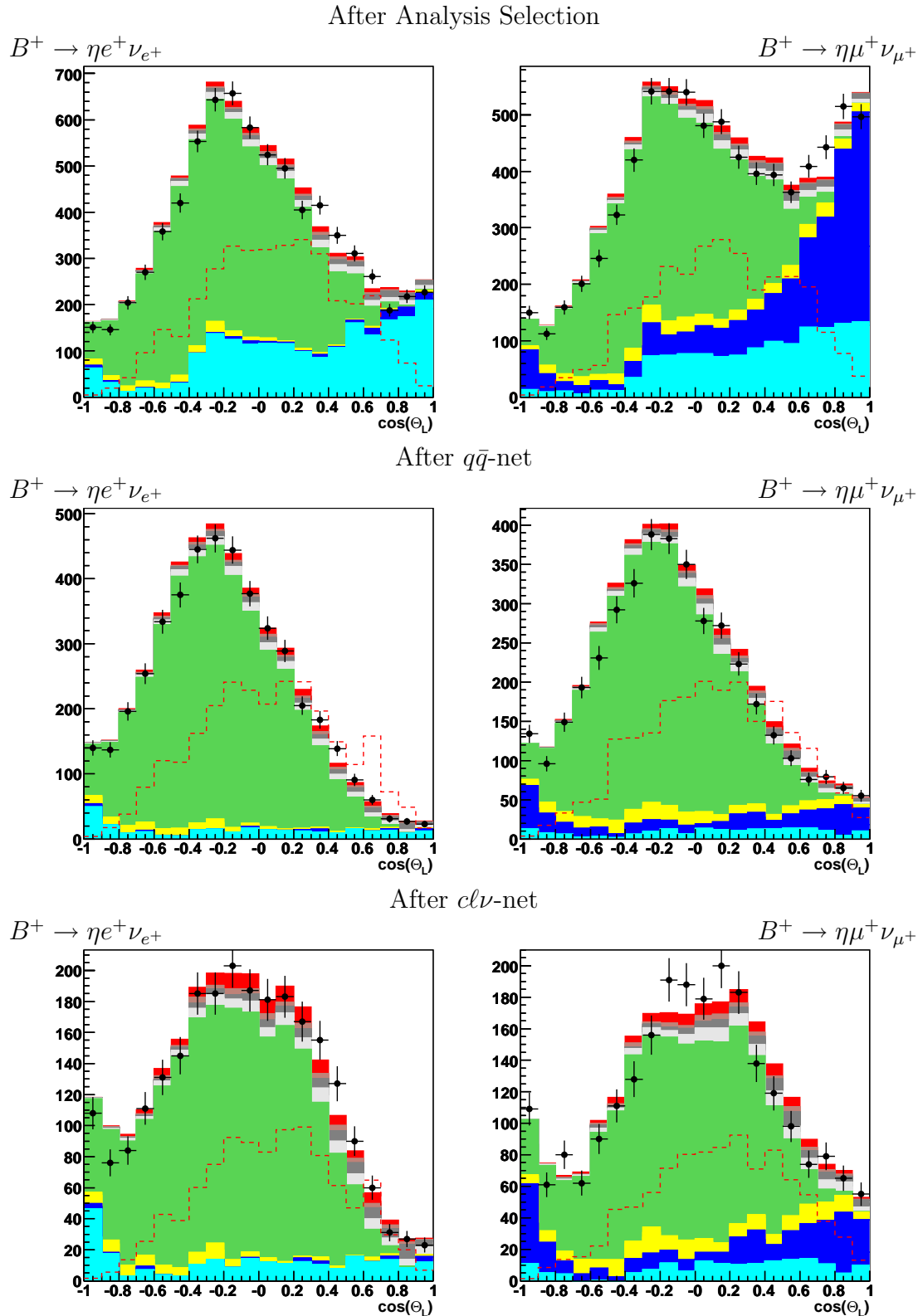


Figure B.11: Distribution of $\cos(\Theta_L)$, the cosine of the angle between the lepton and the W -boson in $\Upsilon(4S)$ system after the analysis section applied (top), after the $q\bar{q}$ -net applied (middle) and after $c\bar{l}\nu$ -net applied (bottom).

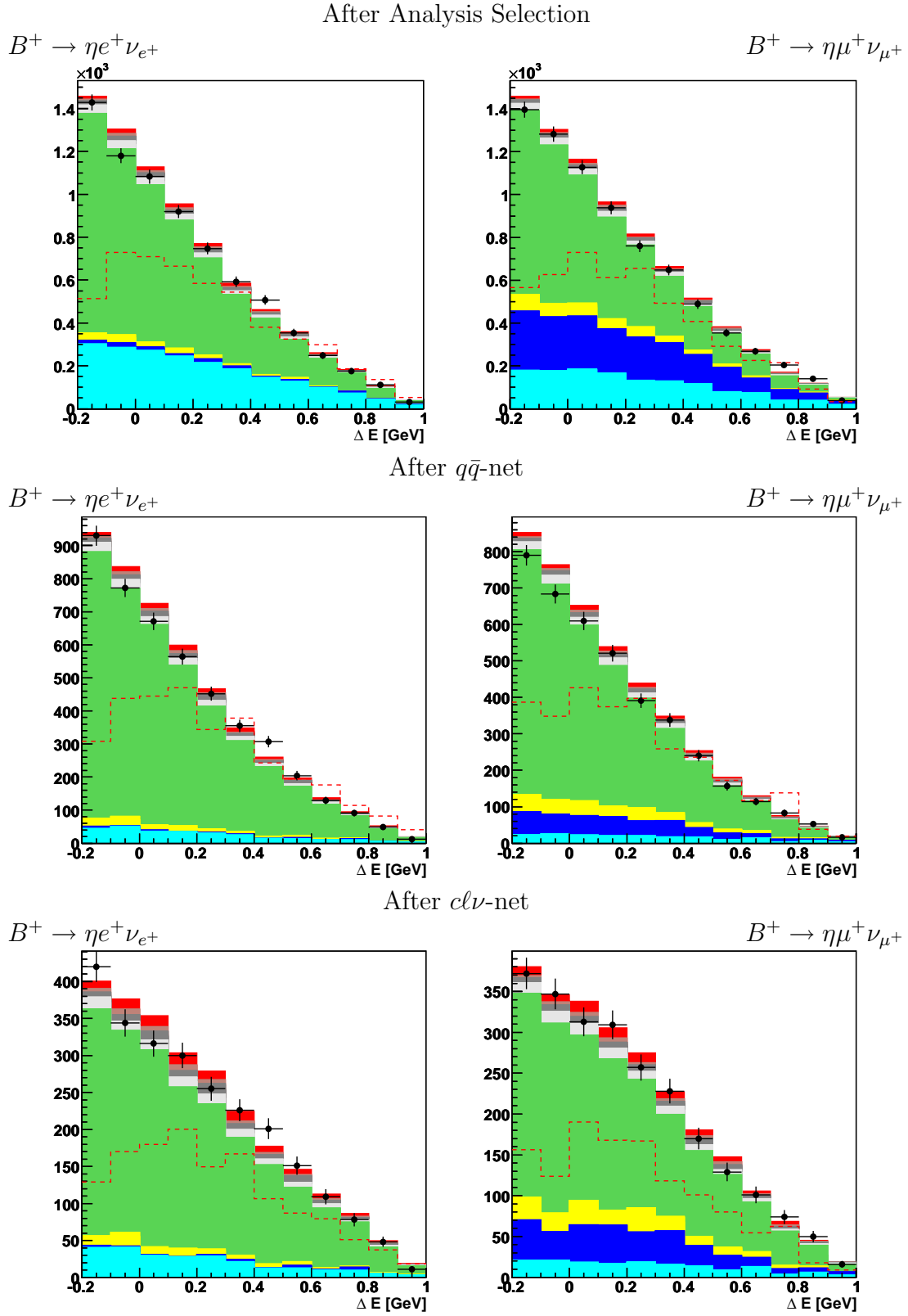


Figure B.12: Distribution of energy difference of the B -meson ΔE after the analysis section applied (top), after the $q\bar{q}$ -net applied (middle) and after $cl\nu$ -net applied (bottom).

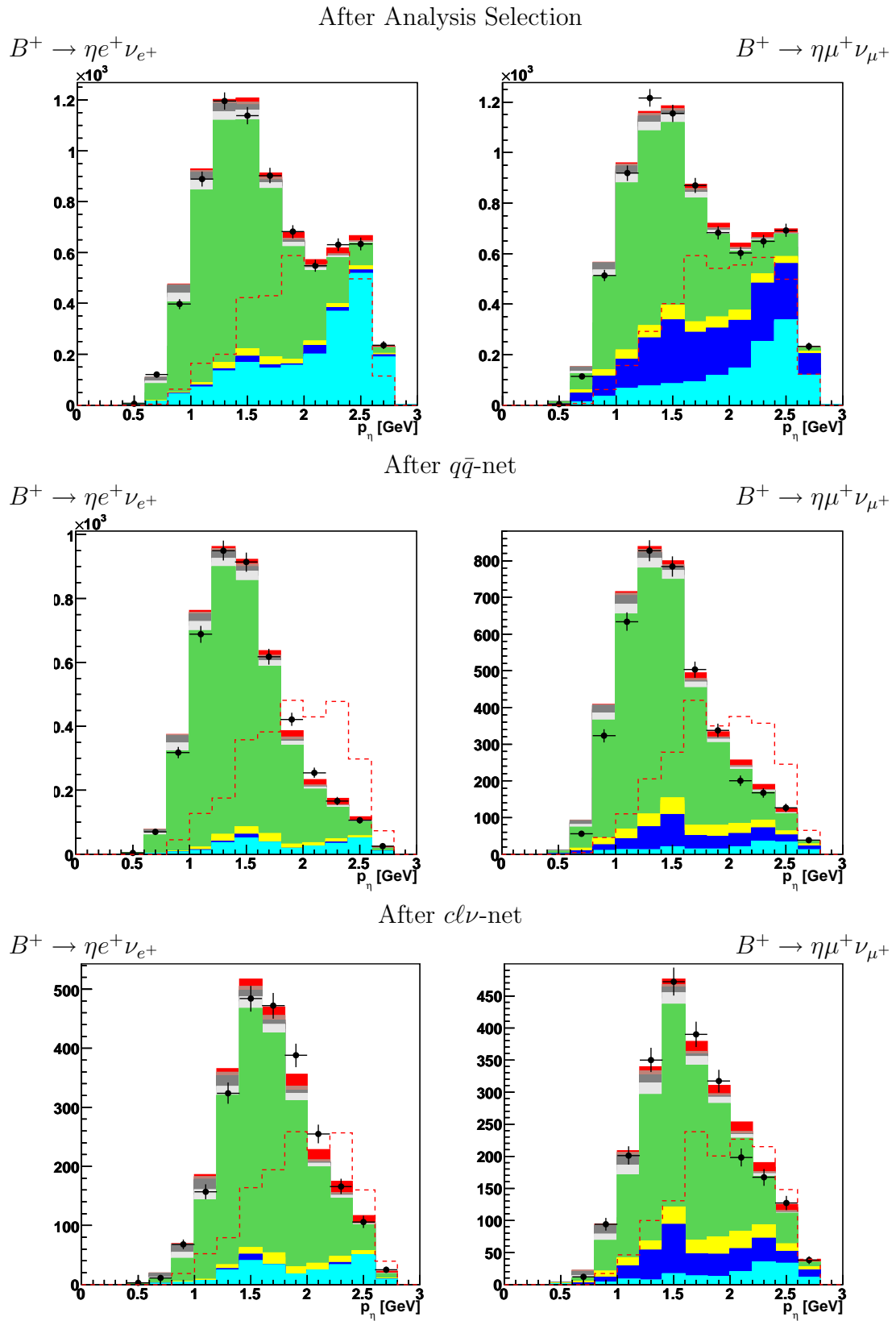


Figure B.13: Distribution of the momentum p_η^* of the η in the $\Upsilon(4S)$ system after the analysis section applied (top), after the $q\bar{q}$ -net applied (middle) and after $cl\nu$ -net applied (bottom).

Erklärung

Ich versichere, dass ich diese Arbeit selbständig verfaßt und keine anderen als die angegebenen Quellen und Hilfsmittel benutzt habe.

Heidelberg, den 15. Juni 2007
